GEOLOGICAL INFLUENCES ON THE STRENGTH OF ROCKS AND IMPLICATIONS ON BRITTLE ROCK MASS BEHAVIOR

JEFFREY ANANGKAARA GANYE

A THESIS SUBMITTED TO THE FACULTY OF GRADUATE STUDIES IN PARTIAL FULFILLMENT OF THE REQUIREMENTS OF THE DEGREE OF MASTER OF APPLIED SCIENCE

GRADUATE PROGRAM IN CIVIL ENGINEERING

YORK UNIVERSITY

TORONTO, ONTARIO

December 2020

ABSTRACT

Selection of the Hoek-Brown material constant, m_i for use in design is often not based on thorough laboratory test results but rather on an estimate solely based on rock type from published tabulations. Rock strength properties are well known to have a high coefficient of variation and therefore a more rigorous approach to determining m_i needs to be considered when laboratory testing data is not available. This research examines a suggested approach that considers the interlocking nature of grains, modal grain size, anisotropy, porosity, and the degree of mixing of the grains to make estimates of the material constant. The procedure is applied to a number of rock sample photos, which were taken as part of a data set of compressive and tensile strength testing on a variety of rock types. The individual influences are examined and the resulting effects on the value of m_i are discussed. In addition, the way in which such an approach can be useful in conventional numerical modelling techniques are explored. This approach, based on visual inspection of rock type characteristics, was found to have an overall accuracy of up to 81% when compared to m_i values calculated from laboratory test data. The approach worked best with granitic rocks showing an accuracy of 96%, however, it was less effective with finer grained rocks such as limestone with an accuracy of 59%. The visual based *mi* technique was applied to the Bedretto adit in a back-analysis study to determine how closely the modelling would predict the true overbreak depth. The visually determined m_i resulted in a conservative overestimate of the depth of damage, ranging from 4% up to 35% over a limited laboratory test derived m_i value. The conservative overestimate means the approach is suitable for preliminary feasibility studies and design and as the visual approach gives a more reliable estimate of the m_i parameter than simply selecting a value from published tables based on the rock type.

ACKNOWLEDGMENTS

I would like to express my gratitude to my supervisor, Dr. Matthew Perras and committee member, Dr. Rashid Bashir for all their support and encouragement. Through their expertise and guidance, they imparted knowledge that was invaluable to the completion of this research project.

Special thanks to Dr. Trevor Carter, who developed and provided me with the theoretical foundations upon which this research project was undertaken. Many thanks to SKB and Diego Mars Ivars for discussion on the laboratory findings and putting us into contact with the Swedish National Testing and Research Institute who provided me with the laboratory datasets which were paramount to the completion of the project. To Apostolos Vasileiou, your expertise in the use of the primary software for image analysis was invaluable and greatly appreciated. To Rodrigo Alcaíno Olivares, and the Engineering Geology group at ETH Zurich, many thanks for providing me with data from your previous works, which was built upon in this project. Thanks are also due to Drs Florian Amann and Pooya Hamdi of the Department of Engineering Geology and Hydrogeology at RWTH Aachen University for discussions on the Bedretto Adit and the Rotondo granite.

Gratitude to all my friends who shared with me the culture and experience and contributed to my personal growth. Thank you, Pushpendra, Rodrigo and Josephine, you guys were my family during these amazing times. Thanks to all the lecturers in the Civil department who imparted me with life-long knowledge and experience, and special thanks to all the technical and administrative staff in the department for being a reliable source of accurate information and problem solver.

Finally, I am grateful to my family for their guidance and also supporting the decisions I have made in my life, and their continuous words of encouragement through these unusual times even while they are thousands of kilometers away.

TABLE OF CONTENTS

LIST OF TABLES

LIST OF FIGURES

LIST OF SYMBOLS

CD	crack damage stress (MPa)
CI	crack initiation stress (MPa)
d	rock grain diameter (mm)
Is	point load index strength (MPa)
$K_{G\phi}$	kurtosis modifier term
m_b	rockmass Hoek-brown parameter
m_i	intact Hoek-Brown parameter
n	porosity (%)
R	Sheorey quotient
T	tensile strength (MPa)
U	tunnel damage extent (m)
UCS	uniaxial compressive strength (MPa)
β	spall notch deviation from horizontal (°)
Θ	vertical tilt of tectonic stress from horizontal plane (°)
λ	mean fracture frequency (m^{-1})
ξ	grain interlock parameter (%)
σ_1	major principal stress (MPa)
σ_2	minor principal stress (MPa)
σ_t	tensile strength (MPa)
σ_{tect}	tectonic strength magnitude (MPa)
σ_y	yield strength (MPa)
φ	angular deviation of tectonic stress from tunnel axis (°)
ψ	rock fabric anisotropy

CHAPTER 1. INTRODUCTION

1.1 Problem Statement

Laboratory test results are necessary as inputs for rock engineering design, whether for input into analytical, empirical, or numerical solutions. However, due to financial constraints, the complexity of testing procedures, and inconsistent results, the required testing results are not always available. Rock strength properties are well known to have a high coefficient of variation (Diederichs, 2007; Langford, 2013) and therefore a more rigorous approach to determining such properties needs to be considered when laboratory testing data is not available (Cowie & Walton, 2018).

The Hoek-Brown failure criterion (Hoek & Brown, 1980) is one of the most widely used empirical criteria for defining the confinement-strength relationship for rocks. For an intact rock, only two parameters, the intact material constant (m_i) and the uniaxial compressive strength (σ_c) need to be determined to fully define the Hoek-Brown envelope. Between the two, m_i is the more challenging to determine due to the fact that it utilizes tensile, unconfined, and confined compression test results when being determined.

This research aims to develop an alternative procedure to estimate the Hoek-Brown mi parameter, based on image analysis of rock samples. This allows a first pass estimate of the parameter to be made even in the absence of extensive laboratory data. Such an approach is an improvement upon simply selecting a value from already published tabulations based solely on the named rock type in question, which is common practice in industry. The visual estimates are compared against laboratory-determined values to assess its reliability and limitations, and its impact of the performance of a finite element model of a tunnel in brittle rock is evaluated. In the research, the influence of certain individual geological parameters such as grain size and porosity on the strength of rocks will be addressed and their impact on numerical models will also be evaluated. It is anticipated that after a rigorous assessment of the feasibility of this visual approach, it can be implemented as a routine procedure for determining the mi parameter.

1.2 Thesis Objectives

The specific objective of this thesis was to develop a cost-effective method for making a first pass estimate of the Hoek-Brown failure parameters during the early stages of a project. This method can be used on sample photos taken during core logging and can be used as a potential solution to the challenge of how best to determine rock strength parameters in the absence of laboratory test data. To address these challenges, the following objectives were set;

1. Assessing the influences of various geological parameters including grain size and distribution, porosity and anisotropies such as foliation on the behavior of rocks under tensile and compressive loads.
2. Using existing methods on a laboratory test dataset to calculate Hoek-Brown m_i values for various granitic and limestone rock types.
3. Developing a procedure for visually estimating the Hoek-Brown m_i value of a rock material based on quantified geological parameters of the above-mentioned rocks using photos of the samples taken before laboratory tests. Comparisons of the laboratory-determined and visually derived m_i values are made to assess the accuracy of the new procedure.
4. Conducting a numerical back analysis exercise to estimate the stress regime around an adit based on observed damage inside the tunnel. This is followed using the visual m_i values as inputs to the numerical models and making comparisons of the extents of

damage in these models with the original models that have laboratory-estimated m_i values as inputs.

1.3 Thesis Outline

The thesis is structured in a traditional thesis format with the chapters contributing together to produce a complete account of the research.

Chapter two presents a review of current theoretical knowledge on brittle failure of rocks. In this chapter, the International Society for Rock Mechanics (ISRM) suggested laboratory testing methods for determining the intact geomechanical properties of rocks and their applications in characterizing insitu rockmass behavior, as well for numerical modeling purposes are explored (ISRM, 1978; ISRM, 1985; Bieniawski & Bernede, 1979)

Chapter three presents an assessment of the influences of various geological parameters including grain size and distribution, porosity, and anisotropies such as foliation, on the behavior of rocks under tensile and compressive loads. A database of tensile and compressive test results consisting of a variety rock types compiled by Perras and Diederichs (2014) is analyzed by sorting based on individual geological parameters, establishing trends and evaluating their interrelationships with each other.

In chapter four, a database of laboratory tests with sample photos is compiled. Hoek-Brown m_i for each rock type is determined by curve fitting the datasets using various curve fitting algorithms. The previously discussed geological parameters are quantified for each rock type and by following Carter's (2019) guidelines, visual estimates of m_i for each rock type are made. The visual estimates are compared with laboratory-determined values to evaluate its performance and identify its limitations.

Chapter five focuses on numerical modeling. A numerical back analysis exercise is conducted to estimate the stress regime around a tunnel based on observed damage inside the tunnel. The performance of the models is assessed against the variability of the estimated mi of the rock material and the laboratory-based value.

The last chapter constitutes the final assessment of the research, in which the research findings are discussed, and conclusions are drawn. Theoretical knowledge is applied to explain the interrelationships between the geological parameters. The limitations of this study are identified, and future research is suggested.

CHAPTER 2. THEORETICAL BACKGROUND

2.1 Brittle Failure in Hard Rocks

Brittle failure of rock has been the subject of ongoing research for the past few decades due to its relevance in a wide range of rock engineering problems including slope stability and surface and underground excavations. In most cases, it is an unwelcome phenomenon, and the possibility of brittle failures should always be taken into consideration in rock engineering projects.

2.1.1 The Hoek-Brown Failure Criterion

The Hoek-Brown failure criterion (Hoek and Brown, 1980) was introduced to provide input data for the numerical analysis of underground excavations. The model describes the behavior of intact rocks under compressive and tensile stresses, while also providing a strength-reduction mechanism for jointed rock masses. It is assumed in the criterion that rocks respond to the presence of several small fractures in an isotropic manner. The generalized Hoek-Brown strength envelope (Hoek et al., 2002) of a rock is defined by the equation;

$$\sigma'_1 = \sigma'_3 + \sigma_c \left(m \frac{\sigma'_3}{\sigma_c} + s \right)^a \tag{1}$$

Where m is a rock material constant, which may be denoted as m_i for intact rock and m_b for rock mass.

s is a rock material constant, where $s = 1$ for intact rock.
a is a rock material constant.
σ_c is the uniaxial compressive strength of intact rock

In the original Hoek-Brown formulation (Hoek and Brown 1980), the parameter a was a fixed value of 0.5. This was subsequently changed to a variable in the generalized form (Hoek et al.

2002), ranging from 0.5 for good quality rock and approaches 0.6 for disturbed rock masses. This was necessary after it was recognized that the Rock Mass Rating (RMR) system of Bieniawski (1976) was not adequate for relating the failure criterion to geological and structural weaknesses in rocks, paving way for the geological strength index system (GSI) that is currently in use. The generalized Hoek-Brown formulation is currently available in commercial engineering software, such as Rocscience. The rock mass and rock material constants are defined as functions of GSI and rock disturbance factor (D) according to the following equations.

$$s = \exp\left(\frac{GSI - 100}{9 - 3D}\right) \tag{2}$$

$$m_b = m_i exp\left(\frac{GSI - 100}{28 - 14D}\right) \tag{3}$$

$$a = \frac{1}{2} + \frac{1}{6}\left(e^{\frac{-GSI}{15}} - e^{\frac{-20}{3}}\right) \tag{4}$$

The GSI classification system uses two factors – the overall blockiness and the condition of joints to obtain a numerical value of the quality of the rock, ranging from 0 to 100 as shown in Figure 2.1. The disturbance factor is associated with the stress removal and the rock dilation due to removal of rock masses by sudden and destructive methods such as blasting. It ranges from 0, which represents a careful design of blast hole pattern, explosive charges and blasting sequence to achieve a smooth blast, to 1 a very poorly designed blasting system.

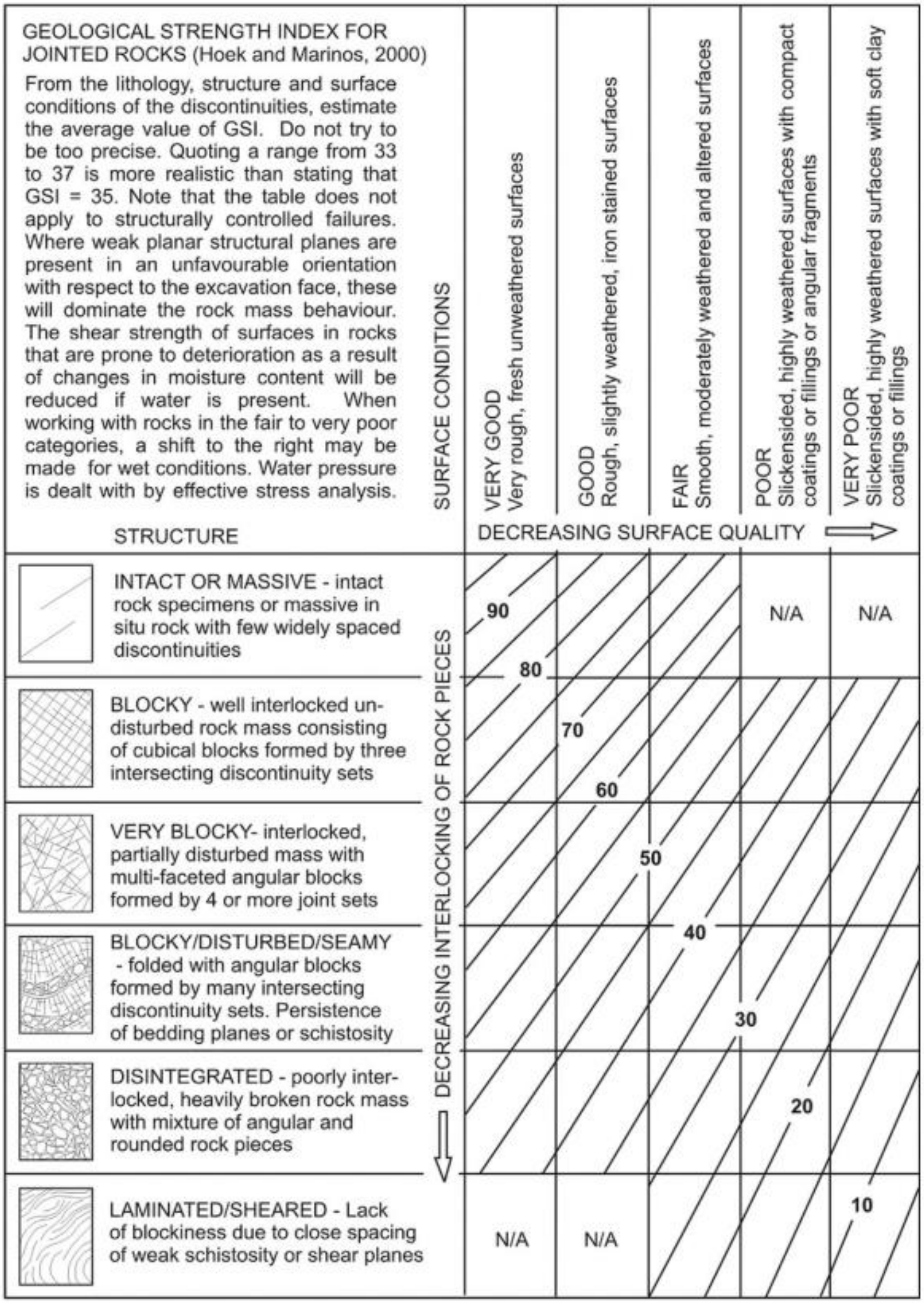

GEOLOGICAL STRENGTH INDEX FOR JOINTED ROCKS (Hoek and Marinos, 2000)

From the lithology, structure and surface conditions of the discontinuities, estimate the average value of GSI. Do not try to be too precise. Quoting a range from 33 to 37 is more realistic than stating that GSI = 35. Note that the table does not apply to structurally controlled failures. Where weak planar structural planes are present in an unfavourable orientation with respect to the excavation face, these will dominate the rock mass behaviour. The shear strength of surfaces in rocks that are prone to deterioration as a result of changes in moisture content will be reduced if water is present. When working with rocks in the fair to very poor categories, a shift to the right may be made for wet conditions. Water pressure is dealt with by effective stress analysis.

Figure 2.1. GSI classification chart used either as a standalone system for determining rock quality or as inputs to develop the Hoek-Brown strength envelope of a rock (Hoek and Marinos, 2000)

2.1.2 Stress-Induced Brittle Failures in Deep-Seated Tunnels

One of the areas in which studies into the development of brittle failures continue to be prominent is the construction of deep-seated tunnels (Martin et al., 1999; Hajiabdolmajid and Kaiser, 2003; Diederichs, 2007; Perras and Diederichs, 2016; Renani and Martin, 2018). In these tunnels failure usually occurs due to high stress concentrations at the excavation surface which exceed the crack initiation threshold (Diederichs, 2007). When the excavation is created, the in-situ stresses increase in the tunnel walls which are parallel to the maximum principal stress and this can instigate stress-induced fractures parallel to the tunnel wall (Martin et al., 1999). As described by Diederichs (2007), rocks under stress may undergo brittle failure in the form of spalling or strain bursting depending on the stress to strength ratio. Spalling may not necessarily be violent and may occur over a long period of time. Case history analysis of rock bursts by Lee et al. (2004) showed that there is a high potential for rock bursts in tunnels at depths greater than 400m, especially if the tunnel was excavated by a tunnel boring machine.

The tunnel excavation process itself also induces damage around the tunnel. The degree of damage usually attenuates radially away from the tunnel. At great depths below the ground surface, the brittle failure region around the tunnel is generally symmetrical and for in-situ stress regimes in which the major and minor principal stress vary significantly, a notch-shaped failure geometry typically develops (Martin et al., 1999; Hajiabdolmajid et al., 2002 Diederichs, 2007).

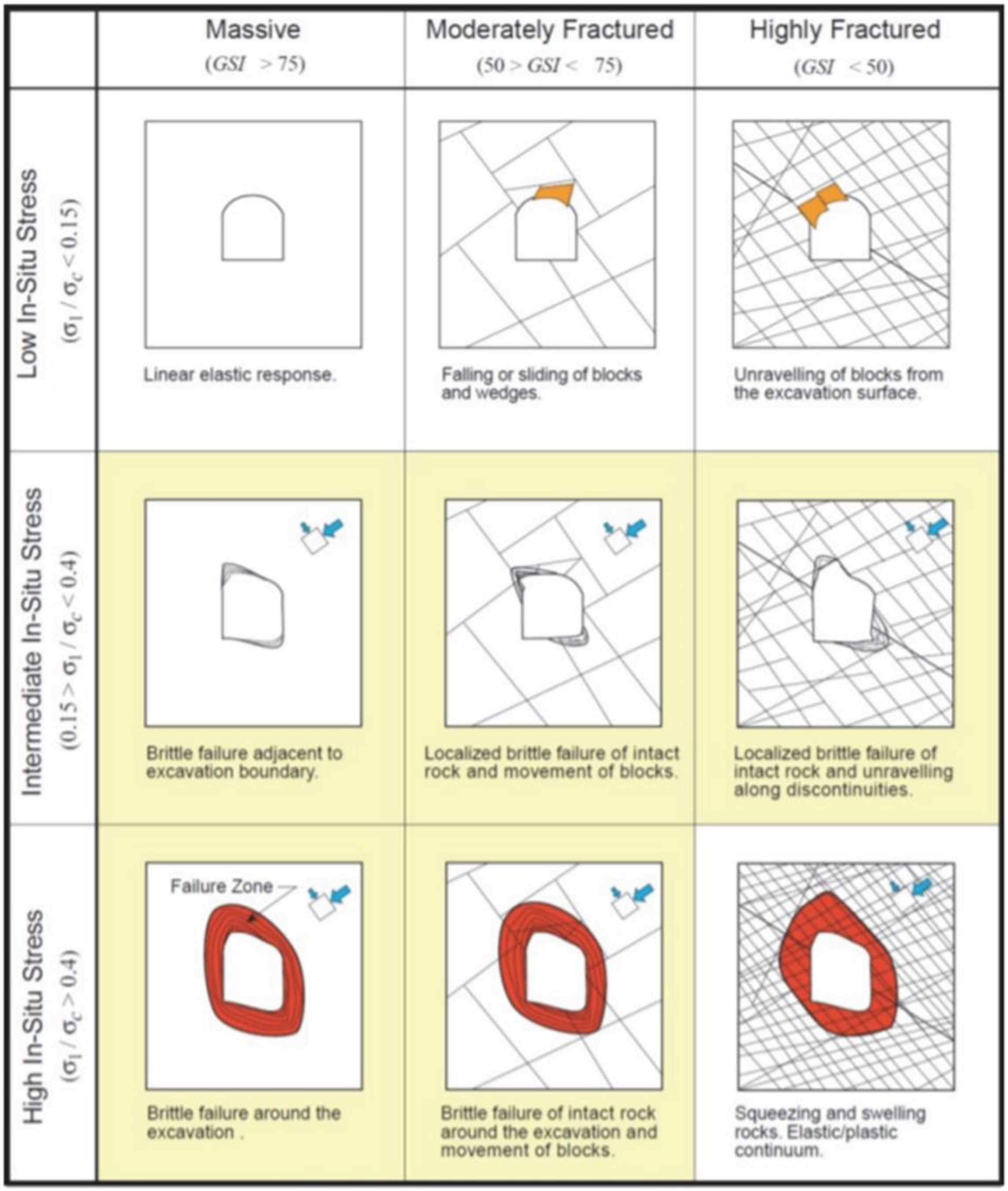

Figure 2.2. Illustration of tunnel brittle failure as a function of degree of fracturing and in-situ stress (modified from Hoek et.al, 1995)

The spalling processes is recognized to be associated with tensile crack growth (Diederichs, 2007). It has also been observed in vertical laboratory scale boreholes (Lee and Haimson, 1993; Haimson and Song, 1993) and in-situ boreholes and wells (Bell and Gough, 1979; Moos and Zoback, 1990; Zoback, 1985). In most cases, the notches were observed to form in the direction of the minimum horizontal stress and it was suggested that the shape and orientation of the borehole notches may be used to determine the orientation of in-situ far-field stress. The general alignment of spall notches with far-field stress orientation is illustrated in Figure 2.3.

An example of such a tunnel in Canada in which spalling damage has occurred is the underground research laboratory (URL) located approximately 120 km NE of Winnipeg, Manitoba (Figure 2.4). The URL lies within the Lac du Bonnet granite and consists of four experimental levels at depths ranging from 130 m to 420 m. At the 420 level, a major excavation response experiment was conducted to study the process involved in the progressive development of spalling using monitoring instrumentation including extensometers, acoustic emission sensors and triaxial strain cells (Read, 2004).

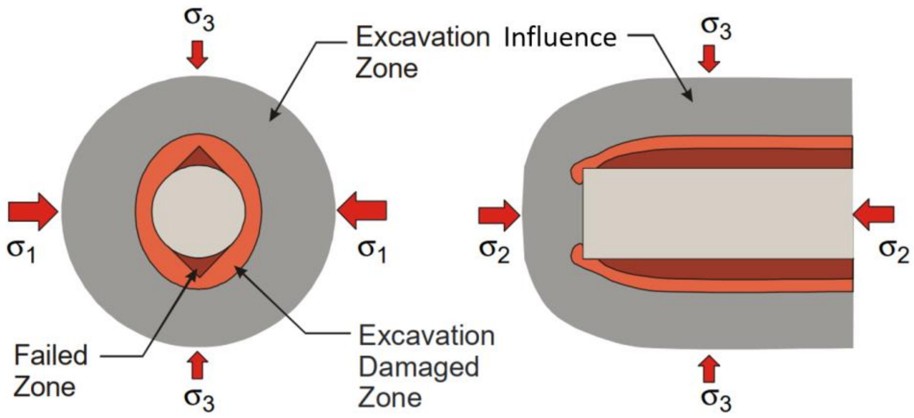

Figure 2.3. Schematic illustration of excavation damage zones around a circular tunnel (Read, 2004)

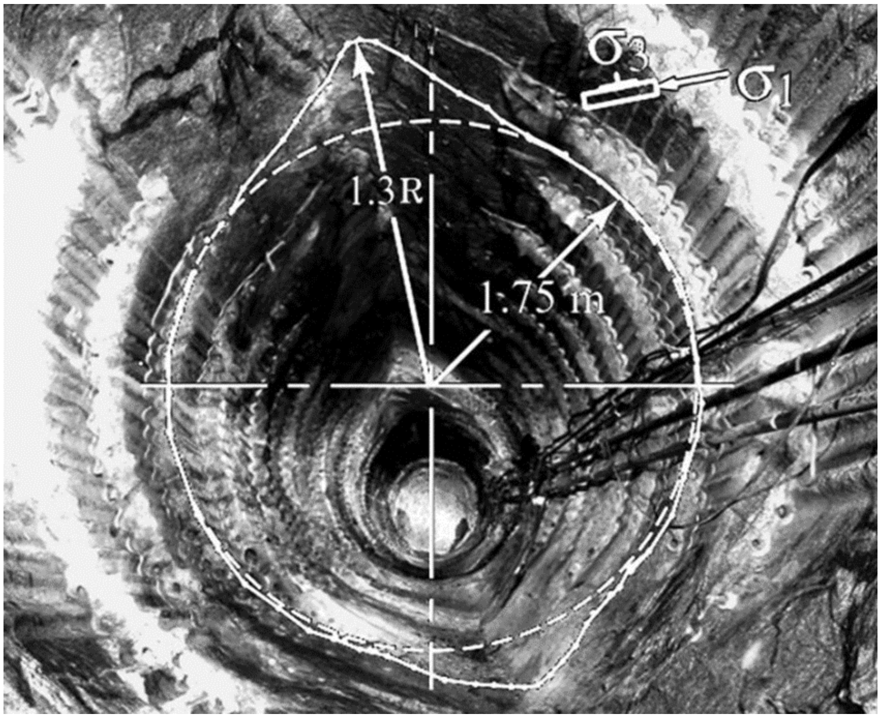

Figure 2.4. Photograph of mine-by-test tunnel at URL (Diederichs, 2007). The photograph shows the distinctive notch and the orientation of the stress field

Empirical studies from boreholes and tunnels suggest that the far-field stresses that have the greatest influence on the orientation and extent of spalling are oriented approximately perpendicular to the long axis of the tunnel. Diederichs, (2007) indicated that because spalling forms parallel slabs by extension cracking, both the Mohr-Coulomb and Hoek-Brown (Hoek and Brown, 1988) failure criteria, which are based on “yield via ubiquitous continuum shearing”, are incompatible with the mechanics of spalling. To model the spalling phenomena, Diederichs (2007) suggested a composite model that consists of a peak (damage initiation) and residual (spalling limit) envelope.

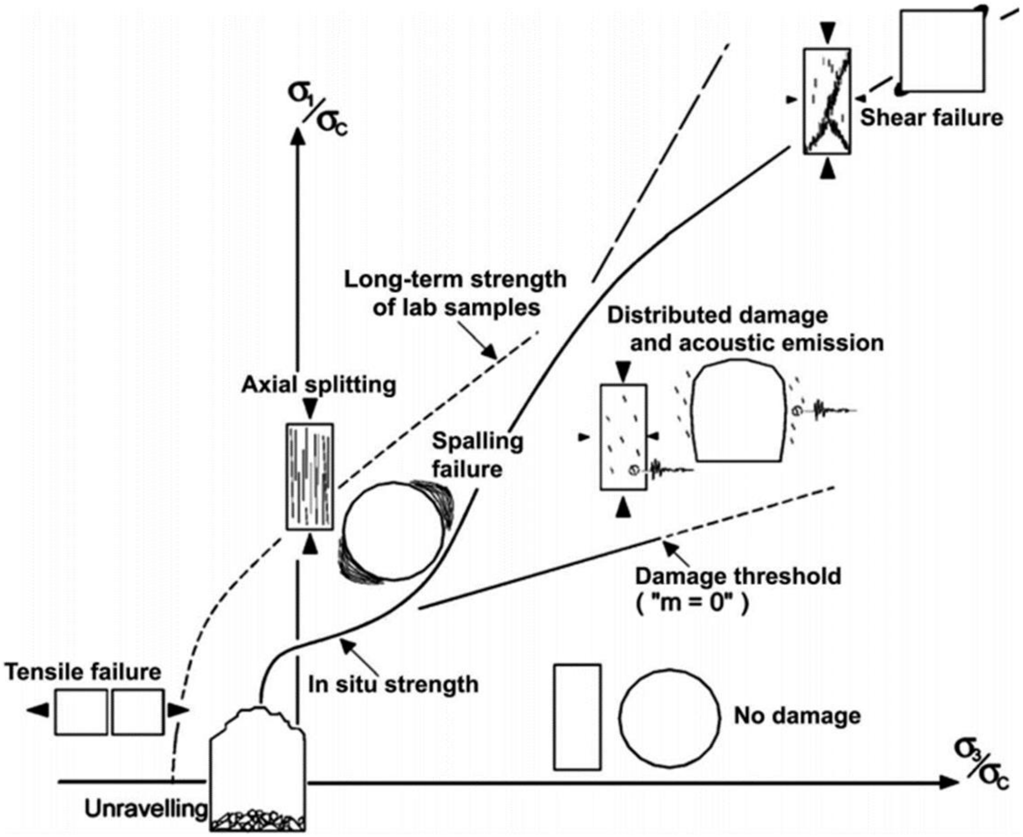

Figure 2.5. Composite strength envelope highlighting the different zones of rock behavior (Deiderichs, 2007)

The two envelopes are developed by setting specific rock parameters in the generalized Hoek-Brown criterion (Hoek et al., 2002) to better represent the role of friction in the post yield failure process. The failure mechanism for rocks changes under different conditions of pure tension, uniaxial compression or triaxial tension. Figure 2.5 shows a composite strength envelope that illustrates the conditions under which the common rock failure modes occur.

2.2 ISRM Suggested Methods for Geomechanical Testing of Rocks

Measuring the strength of rock both in the field and the laboratory is governed by ISRM standards with specify the apparatus, sample preparation and load application for each testing type to ensure consistency and reproducibility of testing results. This section presents and overview of the various testing methods for determining the tensile, uniaxial and triaxial strengths of rocks in the laboratory.

2.2.1 Point Load Test

The point load test is a relatively quick and easy method used to determine the strength a rock in the laboratory or on the field. As an index test, it does not directly measure a specific strength property of a rock, but the results can be used to predict other strength properties with which it is correlated, such as the tensile or uniaxial compressive strength. It involves the application of two point loads on opposite sides of a rock specimen continuously until failure is achieved. As specified by ISRM (1985), the load application system should consist of spherically truncated, conical platens with a cone angle of 600, meeting tangentially with a tip in the shape of an arc with radius 5mm (Figure 2.6). Although the test can be performed on a rock of any shape (cylindrical, block or even irregular lumps), it is usually preferable to perform the test on rocks samples with standard geometries such as a cylinder. In the case of a cylinder, the load may be applied either axially or diametrically.

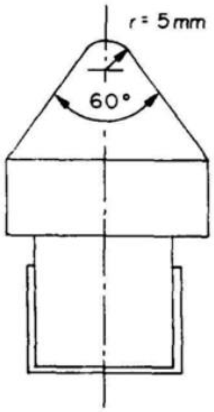

Figure 2.6. Point load test platen shape and tip radius (ISRM, 1985)

Figure 2.7 shows the recommended dimension ratios to be used in a cylindrical sample and some possible failure modes. Due to the nature of the experiment, relatively smaller loads (up to about 50 KN) are usually sufficient, which allows for the use of a portable apparatus. When the test is performed, the uncorrected point load strength, *Is* index can be calculated as P/D^2, where P is the applied load a failure and D is the diameter of the specimen.

A coherent set of units must be used in evaluating *Is*. In order to produce a result with units of MPa, units of N and mm are required for P and D respectively. Point load test results are subject to a size effect and so it is usually recommended to stick to a single specimen shape and size when performing a group of tests. The standard test is conducted on 50 mm diameter core. A correction procedure is available to convert the measured index to a size-corrected value (termed Is_{50}) if a different sized core or irregular lump is used.

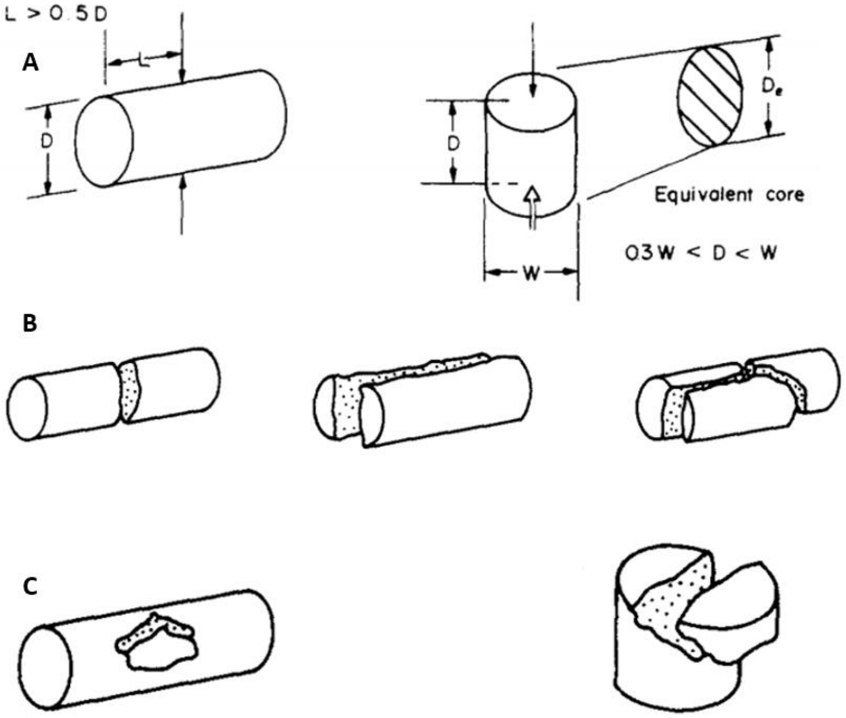

Figure 2.7. (a) Recommended sample geometry and load application points; (b) Ideal failure mode for a valid test, (c) Invalid test failure modes (ISRM, 1985)

The size correction for irregular lump cores can be achieved using the following expression:

$$I_{s50} = I_s \left(\frac{D}{50}\right)^{0.45} \tag{5}$$

Correlations of the index strength with tensile and compressive strengths have been made in the past by various authors. For example, Studies by Bieniawski (1975) of over 1,000 lab tests suggested that for most rock types, UCS can be approximated to be equal to 24 times Is(50). Studies by other authors, as summarized by Basu and Aydin (2006) suggests that the UCS to Is(50) ratio ranges between 15 and 24. In a review of the tensile properties of rocks, Perras and Diederichs (2014) found that the tensile strength of a rock may be estimated to be 1.5 times Is(50).

2.2.2 Brazilian Tensile Test

The Brazilian tensile test (BTS) is an indirect measurement of the tensile strength of a rock typically performed on cylindrical rock samples with a height to diameter ratio preferably ranging from 2.5:3 (ISRM, 1978). This testing method is typically preferred over the direct testing methods, despite them being considered less valid the direct methods. This is mainly due to difficulties associated with preparing samples with the desired shapes, difficulties in firmly griping samples and the frequency of invalid failure modes.

The ISRM testing standard for BTS is based on the theory that the stress at failure is a function of the applied load, sample diameter and sample thickness. Loading is applied axially on the rock sample until it fails by splitting along the center. ISRM (1978) suggests that the loading platen system comprise of a curved set of jaws with radius 1.5 times the radius of the specimen. However other loading platens exist, as shown in Figure 2.8.

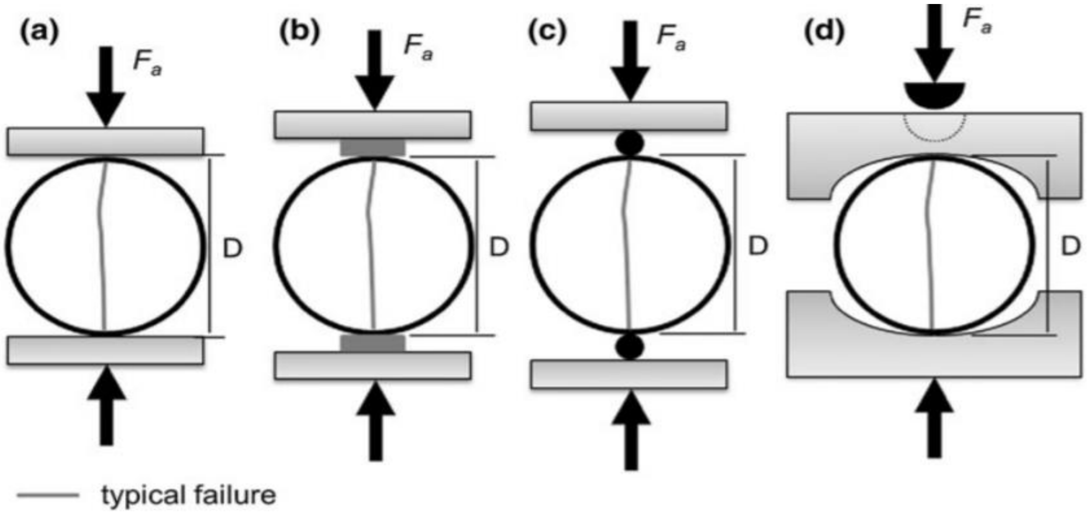

Figure 2.8. Brazilian test platen shapes (from Perras & Diederichs, 2014)

Once the sample has failed, the tensile strength, σ_T, is calculated using the expression determined from 2-D elastic solution by Mellor and Hawkes (1971):

$$\sigma_T = \frac{2P}{\pi DT} \tag{6}$$

Where: P = load at primary failure (N)
D = sample diameter (mm)
T = sample thickness or length (mm)

While a Brazilian test sample is under load, the sample is subjected to tensile stresses along the loading axis, except at the very edges, close to the point of contact of the loading platens where the rock particles are under compressive loads (see Figure 2.9).

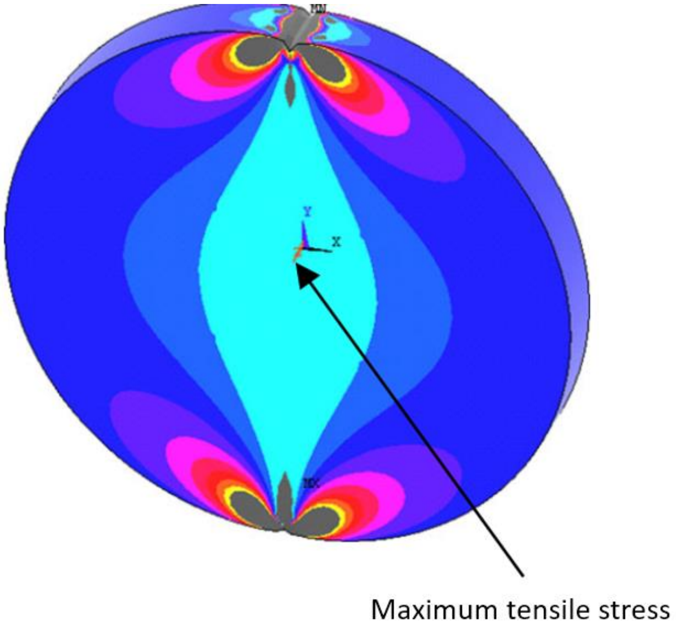

Maximum tensile stress

Figure 2.9. Tensile stress contours for 3D models of a Brazilian disk (from Aliha, 2014)

For a Brazilian test to be valid, the fracture on the specimen should be an approximate straight line that passes through the center of the specimen and touches the points of contact of the platen with the specimen, as shown in Figure 2.8. Perras and Diederichs (2014) noted that invalid tests can easily occur in sedimentary or metamorphic rocks in which existing bedding planes or foliations act as planes of weakness along which the sample splits, rather than vertically through the center.

2.2.3 Uniaxial Compressive Strength Test

The Uniaxial compressive strength (UCS) test is a laboratory testing method for intact rock classification. It is performed on cylindrical samples with height 3 times the diameter (ISRM, 1979). The load application system consists of steel platens in the form of discs with diameter slightly larger than that of the specimen. While the load is being applied, axial and radial strains on the rock sample is continuously measured by the use of electrical resistance strain gauges or linear variable differential transformers (LVDT). It is recommended that the load be applied such that failure occurs within 5-10 min from the start of the experiment. Aside the peak UCS, stress-strain curves can be used to determine other rock parameters including Young's Modulus and Poisson's ratio.

2.2.3.1 Stages of Crack Growth Under Compressive Loading

During compressive testing of brittle rocks, at least four stages of brittle failure can be identified from the stress-strain response during loading. These stages are;

1. Closure of existing cracks
2. Linear elastic behavior
3. Stable crack growth
4. Unstable crack growth

The loading thresholds for the third and fourth stages are commonly referred to by authors as crack initiation (CI) stress and crack damage (CD) stress respectively. (Martin, 1997; Diederichs and Martin, 2010; Paraskevopoulou et al., 2017). The stages of brittle damages and their thresholds are illustrated in Figure 2.10. The figure shows axial stress-radial strain and axial stress-axial strain curves that are typical of rocks during UCS tests.

Many authors have determined the CI and CD thresholds for rocks either thought the stress-strain curves or through the detection of acoustic emission activity of the rocks under compression. (Martin and Chandler, 1994; Eberhardt et al., 1998; Lajtai, 1998; Diederichs et al., 2004). The crack initiation threshold is considered to be the lower bound for in situ strength. It marks the onset of new inter- and intra-granular cracks, dependent on the nature of internal flaws in a rock (Diederichs 2007). Studies show that the threshold usually varies between 30% and 60% of the UCS of a rock (Diederichs, 2007; Nicksiar and Martin, 2013; Ghazvinian

2015). The crack damage threshold, on the other hand, signifies the onset of significant interaction in previously existing cracks, at which point the rock is approaching its yielding limit (Ghazvinian, 2015). In Figure 2.10, axial and lateral strains are measured by strain gauges, from which the volumetric strain and crack volumetric strain are calculated. The thresholds for CI and CD can be determined as the points of reversal of the crack volumetric strain and volumetric strain respectively. Alternatively, CI and CD thresholds can be determined from acoustic emission monitoring as described by Eberhardt et al. (1998) and Diederichs et al. (2004).

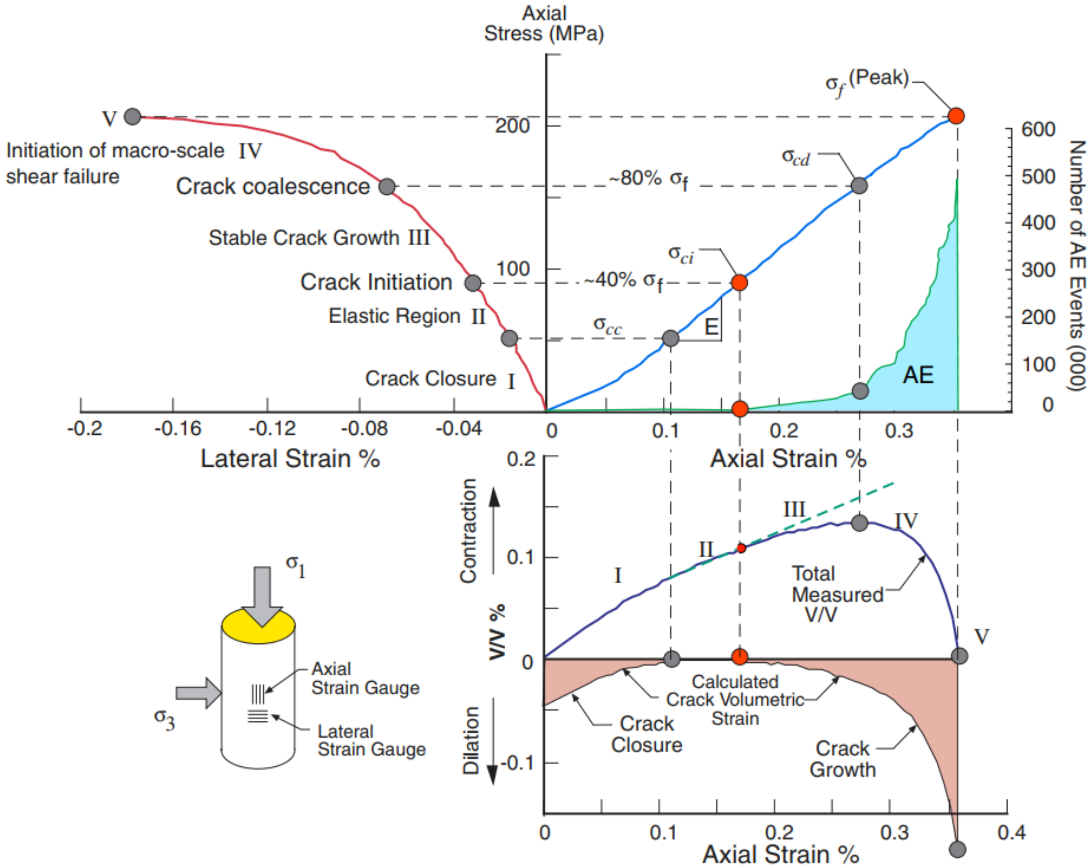

Figure 2.10. Typical stress-strain curves for a rock samples under uniaxial compressive testing showing the four phases of brittle behavior and their associated stress thresholds

CHAPTER 3. GEOLOGICAL AND ENVIRONMENTAL INFLUENCES ON GEOMECHANICAL ROCK BEHAVIOUR

The geological characteristics of a specific rock type and its influence on intact rock strength and stiffness have been studied by many authors (e.g. Nalsund, 2013; Cowie and Walton, 2018, and citations therein). It is a challenging topic to comprehensively explore, given the heterogenous nature of rock, even for the same rock type on one project site. It is generally agreed in the rock engineering community that all aspects of rock texture exhibit some degree of influence of the mechanical behavior of rocks. Spry (1969) defines rock texture to constitute:

1. Mineral grain size (mean, median or mode).
2. Mineral grain distribution (measures of central tendencies which describe the grade of the rock minerals.
3. Geometry of minerals.
4. Spatial orientation of mineral grains (e.g., Foliation).

In addition to the above, Nalsund (2013) notes that other petrological parameters such as grain boundary relations and degree of alteration of minerals equally influences rock behavior under stress. Laboratory measurement of intact rock strength properties are also subject to a degree of uncertainty due to the inherent heterogeneity in the mineralogical structure of rocks, to Samples taken from the same site will still usually possess diverse micro defects and minor differences in petrographic characteristics that will inevitably affect the results of experiments, sometimes to significant extents. For example, in the case of UCS testing, at least five different failure modes have been identified (see Figure 3.1), each of which can occur in any given sample.

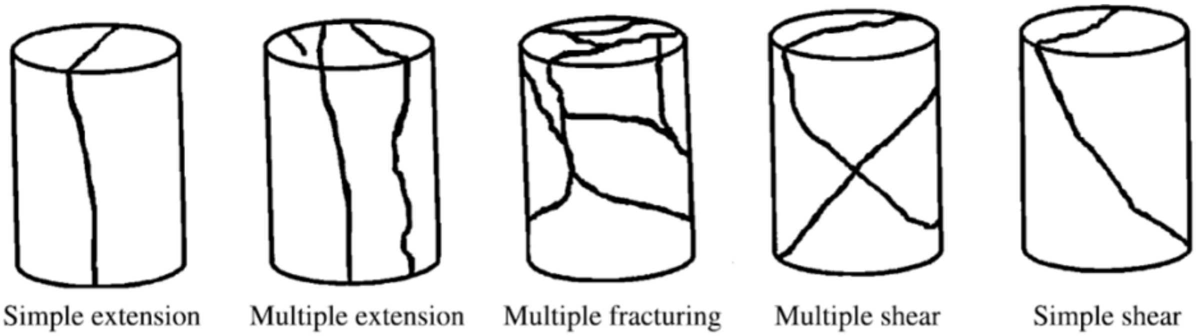

Figure 3.1. Possible failure modes for a UCS test (Szwedzicki, 2007)

Since the International Society for Rock Mechanics (ISRM) has established a standardized procedure for most conventional rock tests, the degree of uncertainty attributed to human and equipment related errors is expected to be low, as long as testing equipment of suitable quality is used and the standard methods are followed meticulously. It can be reasonably assumed that under near ideal lab testing conditions, natural heterogeneity of rocks should account for most of the variability observed in testing results. When one compiles a database of rock testing data, there is typically a wide range of values, reflecting the natural heterogeneity. For this reason, it is always recommended that engineers, within their capacity, always make measurements on multiple samples to understand the range of uncertainty and minimize sample selection, preparation and testing biases. A minimum of 10 samples per rock domain and test type is recommended by the ISRM.

Take for example the relationship between the tensile strength (both direct and indirect tests) and UCS, as shown in Figure 3.2 from the database of Perras and Diederichs (2014). The slope of a linear trend line on this graph reflects the original quotient definition of mi = UCSi / |σT|, however, one can see that even within the same testing program (single author), not all test results from the same rock type align parallel to an ideal linear trend line. Some, like the Schist from Mishra and Basu (2012), or the limestone of Bell (1981), do in fact align well with a linear trend line. Others such as the granite from Betournay (1983) do not. The question is why not? Many authors (e.g. Cai, 2010; Richards and Read, 2011 and 2013; or Read and Richards, 2012 and 2015) would consider this a reflection of challenges related to testing protocols which have improved over the years. However, as shown by Richards and Read (2011), rock materials have an inherent variability and so even in the most ideal lab testing conditions, test results are not expected to all behave in the exact same manner, as man-made materials might. One can point to the continued debate in the rock engineering community on how best to handle the tensile portion of the failure envelope, with errors in the indirect tensile testing approach and challenges in conducting direct tensile tests having been noted by many authors (e.g. Perras and Diederichs, 2014; Read and Richards, 2015; and Carter and Carvalho, 2020). However, this does not necessarily account for all the scatter in Figure 3.2. One must consider that many of the rock types shown in Figure 3.2 are from the same test program, and would be considered homogeneous from an engineering perspective, yet scatter still exists. For some classic rock types like Indiana Limestone (Churcher et al., 1991) or Barre Granite (Sano et al., 1992) that are considered standards due to their low standard deviation in an individual strength value do not necessarily show consistent correlations when examining multiple strength or property values at the same time. Further compounding the problem are heterogenous rocks, like the schist tested by Mishra and Basu (2012) that does show a consistent trend in Figure 3.2 just below the R = 5 line. The heterogenous nature of rocks is thought by many authors to be due to variation in mineralogical parameters including grain size, porosity, and existing planes of weaknesses. The individual effects of these parameters on the strength of rock are explored in the subsequent sessions.

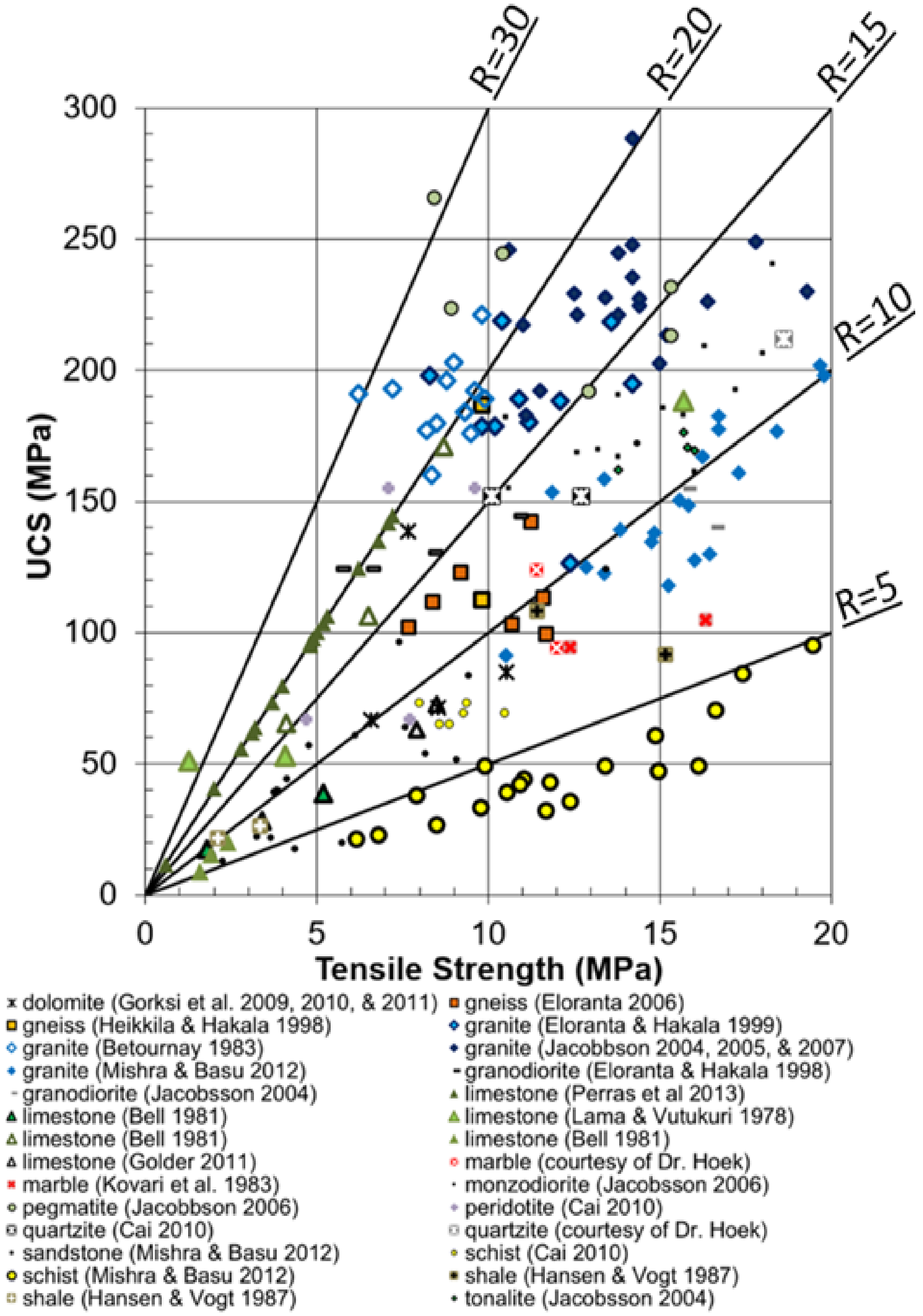

Figure 3.2. Tensile strength versus unconfined compressive strength (UCS) for a variety of rock types (modified from Perras and Diederichs, 2014, see paper for complete references). R is the Sheorey quotient, defined as the ratio of UCS to tensile strength

3.1 Grain Size

The inverse square root of grain size has long been recognized in the materials industry as a benchmark for defining variability in tensile strength (the Hall-Petch relationship, Morris, 2001) with the classic Hall-Petch maxim suggesting that the finer the grain size the higher the tensile strength, (Morris, 2001). For many materials, several mechanical properties including tensile strength, hardness and the ductile-brittle transition temperature has been found vary with the inverse square root of grain size. The classic Hall-Petch equation that relates the yield strength of a material to grain size is defined as;

$$\sigma_y = \sigma_0 + K_y d^{-1/2} \tag{7}$$

Where σ_0 is a friction stress constant. This is the threshold stress for dislocation movement within the material, allowing particles to slide over each other. K_y is the Hall-Petch slope and d is grain size. The strength-grain size relationships serve ss important constitutive relationships in the materials industry.

For rock, where compressive strength is usually considered of more importance than tensile strength, researchers have mainly concentrated on studying grain size influence on UCS tests, with the ISRM suggested methods for compressive testing requiring that test specimen diameters be a minimum of 10 times greater than the largest identifiable grains (Bieniawski and Bernede, 1979). The influence of grain size is however complex but appears to be most dominated by the most commonly present grain size. Grain size is a visually perceptible parameter and rocks with sufficiently different grain size can easily be distinguished from each other, as shown in Figure 3.3. The convention in materials science that finer grain size correlates to higher tensile strength appears to also be applicable in the rock mechanics. Eberhardt (1999) reasoned that longer grain boundaries, as a direct result of larger grain sizes provides longer paths of weaknesses for crack growth. This is theoretically supported by the Griffith theorem for an elliptical crack (Griffith, 1924) which is defined by the expression:

$$\sigma_c \geq 8 * \sqrt{\frac{2E\alpha}{\pi c}} \tag{8}$$

Where: σ_c = Minimum compressive stress to initiate fracture

E = Elastic modulus

α = Surface energy per unit area of crack surface

c = Crack half-length

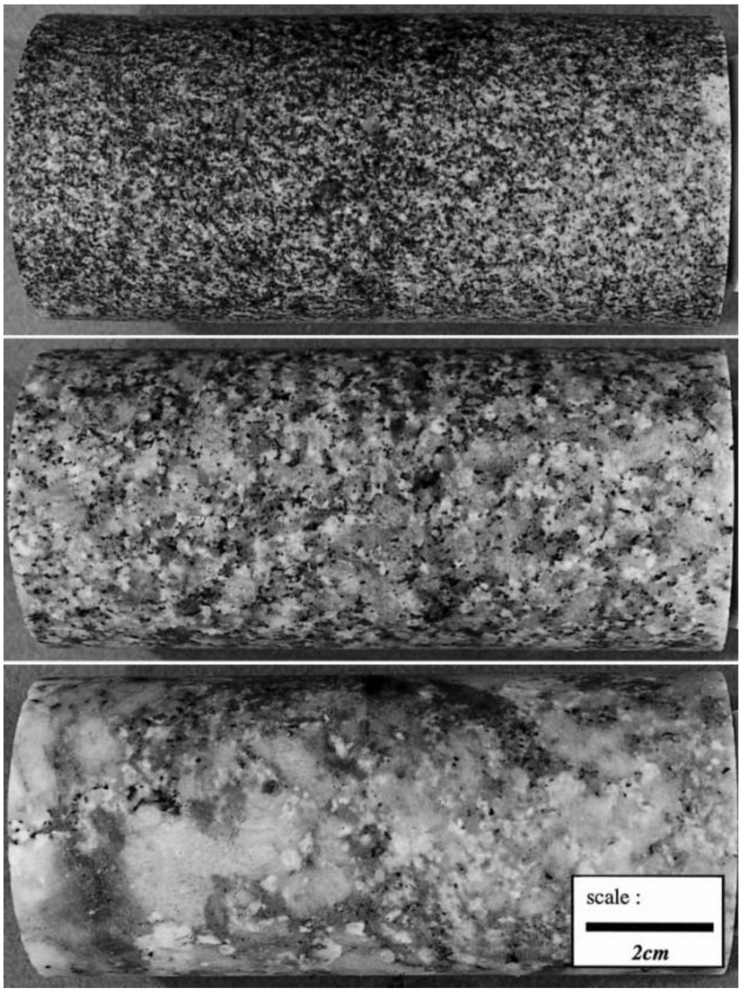

Figure 3.3. Visual comparison rocks with similar mineralogical composition, but different grain sizes: a) Granodiorite - Average grain size = 1 mm; (b) Granite - Average grain size = 3 mm: (c) Pegmatite - Average grain size = 20 mm. (Eberhardt, 1999)

If one considers the crack length to be roughly proportional to grain size, then the equation denotes that the fracture initiation threshold of a rock has an inverse square root relationship with grain size. Hatzor and Palchik (1997), in a study involving dolomite rocks from Israel, demonstrated empirically that both grain size and porosity has an inverse relationship with fracture initiation stress. In low porosity rocks, changes in grain size has a stronger influence on their strength. It can be reasonably assumed that lower porosity rocks have higher overall grain contact and hence there is a stronger grain boundary relationship with strength.

In laboratory tests performed on Lac du Bonnet granite found in Canada's Underground Research Laboratory (URL), Eberhardt (1999) found that the degree of intercrystalline deformation in the rocks had a positive correlation with grain size. Similarly, the number of acoustic emission (AE) events at early stages of loading correlated positively with grain size. In contrast grain size had an inverse relationship with crack damage (CD) thresholds, in agreement with the Griffith theorem. Recent studies by Cowie and Walton (2018) indicate that multivariate analysis, complex as it may be, may provide better insights into the geological influences on the strength of rocks. For example, while the author's studies also supported the convention that grain size varies inversely with tensile strength, the results show that this relationship is strongly influenced by the relative abundance of mica minerals in the rock (Figure 3.4). Mica is a sheet silicate mineral that forms distinct layers that are notably recognized as excellent planes of weaknesses.

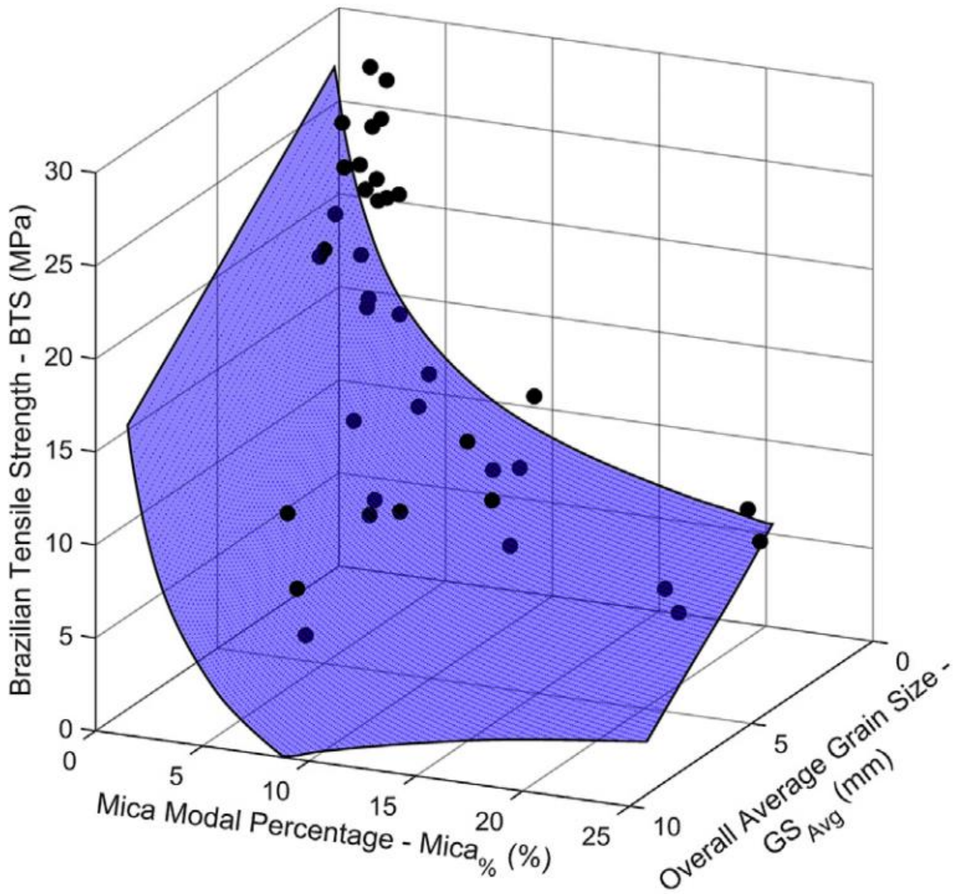

Figure 3.4. Brazilian tensile strength and its bi-variate relationship with mean grain size and mica modal percentage (modified from Cowie and Walton, 2018)

Going back to Figure 3.2 to examine the grain size – strength relationship, a relative size distribution (loosely based on the standard Wentworth (1992) scale) was adopted based on visual inspection of available photographs of the specimens. The results are presented in Figure 3.5, which indicates again a weak alignment parallel to linear trend lines. There are only a few very coarse-grained specimens, and these are mixed within the same ranges as the coarse-grained specimens. There is a clear distinction between the coarse-, medium- and fine-grained specimens. The plot suggests that the finest-grained specimens have the highest m_i's – ie., high compressive strength, yet low tensile strength.

Most of these specimens are limestone and the monomineralic nature of these limestones could place them into a different behavioral mode than the more heterogeneous rock types making up the coarse and medium grained specimens (igneous and metamorphic rocks). Contrary to the high m_i of these limestones in the plot, other sources, such as those in Shen and Karakus (2014) and Jackson (1995), indicate lower m_i values. This is enigmatic with limestone due to induration effects. Young limestones (e.g. Eocene and Tertiary Caribbean cliff materials studied by Carter et al., 2009) show very low m_i values, with tensile strengths almost equal to compressive strengths (each around 10 MPa). This is in contrast to the much older Quintner limestone in the database, which was deposited during the upper Jurassic age (Perras et al., 2012).

The Quintner limestone shows high mi values due to the fact that compressive strengths are in excess of 100 MPa while tensile strengths still remain below 7 MPa. However, it should be noted that the Quintner Formation is highly tectonized resulting in micro-cracks that potentially preferentially affect the tensile strength more than the compressive strength. The Ordovician Ontario limestones also show similarly high m_i values with UCS values reaching as high as 220 MPa and tensile strengths up to 25 MPa. These Ontario limestones are often microcrystalline, recemented, fully indurated and very fine grained and in contrast to with the Quintner little to no influence from tectonic deformations that affected the east coast of North America at the time of deposition.

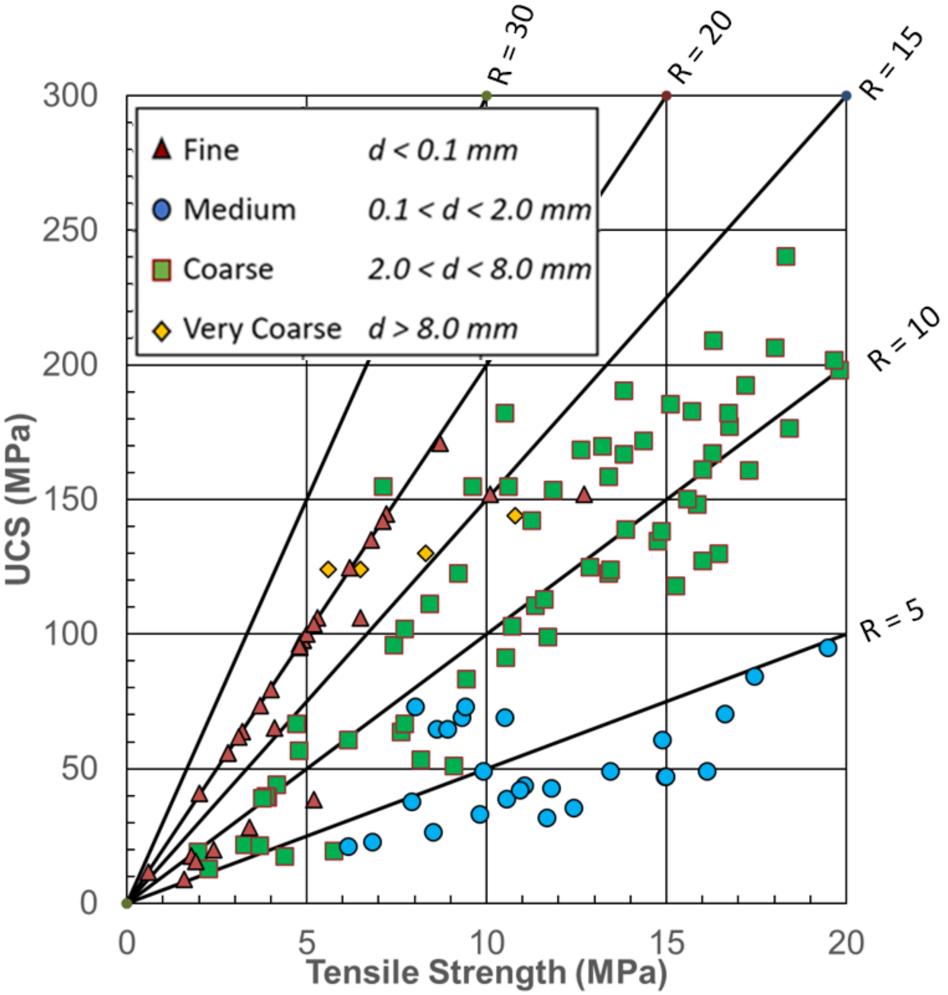

Figure 3.5. Tensile strength versus unconfined compressive strength (UCS) classified by broad grain size categories, where d is the modal grain size (subset from Perras and Diederichs, 2014)

3.2 Anisotropy

Anisotropy in rocks often occurs in the form of bedding, foliation, layering, fissures and preferential orientation of minerals. Their existence in rocks is well-known and their effect on the strength properties of rocks have been studied by many authors (Shea and Kronenberg, 1993; Hakala et.al., 2005; Ghazvinian, 2013). In some cases, different but closely related properties of rocks can respond very differently to the presence of anisotropies. This phenomenon has been observed by Ghazvinian et al. (2013) in experiments involving Cobourg limestone, in which the rocks behaved in a close to isotropic manner under CI and CD levels and remained anisotropic at peak strength. Knowledge of the presence of an anisotropy on its own cannot be used to fully be used to describe rock behavior since studies show that orientation of the anisotropic planes relative loading axes is equally as important (Hakala et al., 2005; Ghazvinian et al., 2013). This angle between the loading axis and plane of anisotropy is often denoted by β. Several models of anisotropies exist, from ones that consider the anisotropy a unique plane of weakness to models that emulate continuously variable rock behavior with respect to loading orientation. Figure 3.6 illustrates the two most common models for describing oriental strength dependence of anisotropic rocks.

In general, the UCS of a rock reaches its peak when compressively loaded perpendicular to its anisotropic plane ($\beta = 90°$) and approaches its minimum as β approaches 45°. This was demonstrated in experiments performed by Ghazvinian et al. (2013) on Cobourg limestones from the Michigan sedimentary basin. Similar responses in rock behavior were observed for UCS, CI and CD tests. Based on the results, The Hoek-Brown strength criterion would predict the limestone rocks to be twice as strong under uniaxial compressive conditions and up to 1.5 times strong-er under tensile conditions, when the anisotropy angle 90°.

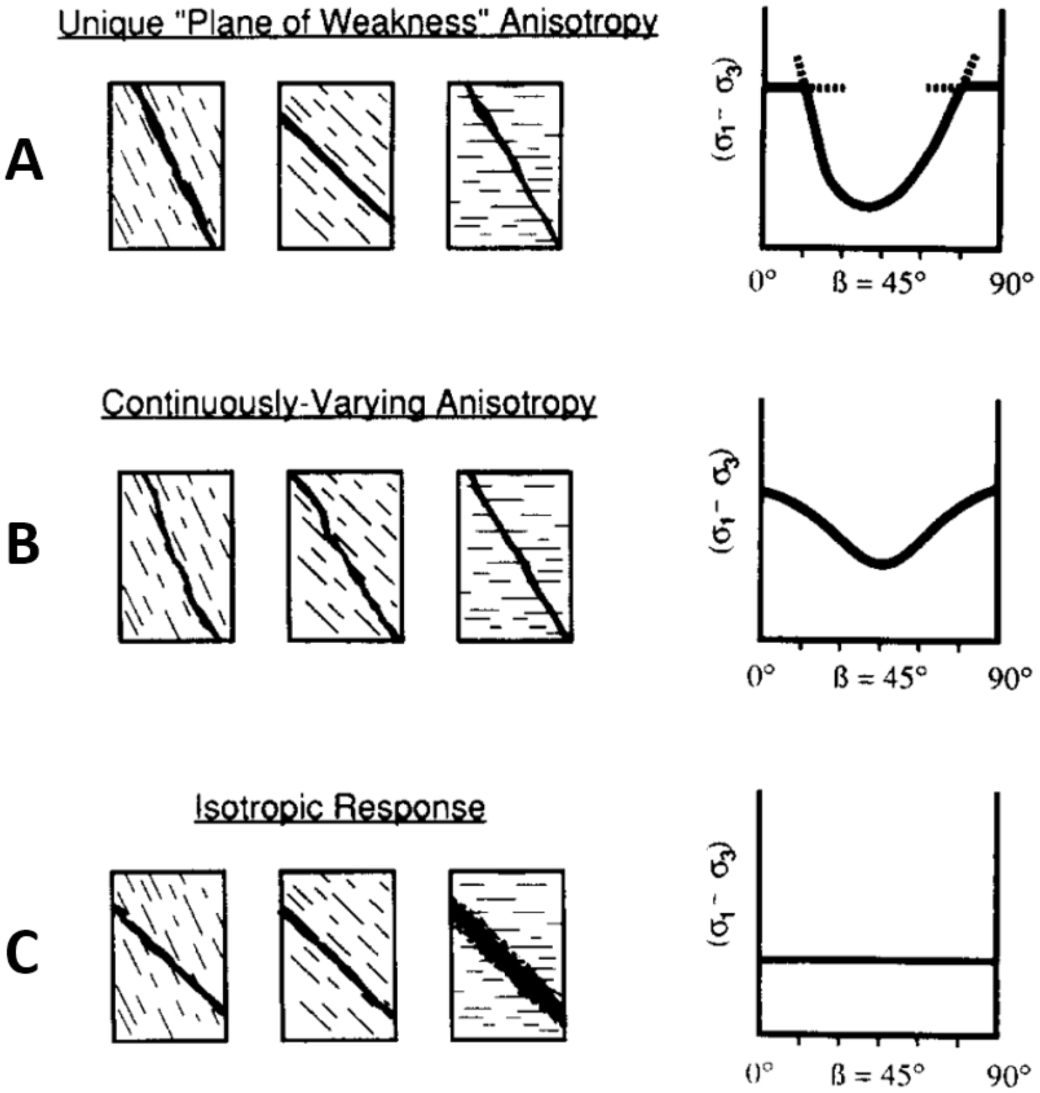

Figure 3.6. Models of ultimate strength as a function of anisotropy angle. A) This model considers the anisotropy to be a singular plane of weakness in an otherwise isotropic rock. B) A continuous model in which strength varies smoothly and continuously with anisotropy angle. C) Depending on the rock and the type of anisotropy, some rocks show no obvious response to the presence of an anisotropy (from Shea and Kronenberg, 1993; Ghazvinian et al., 2013)

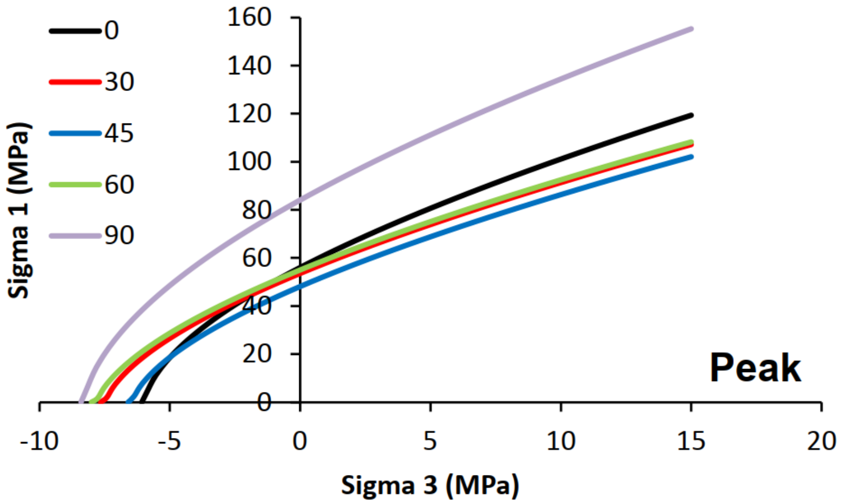

Figure 3.7. Hoek-Brown envelopes at different anisotropy angles for Cobourg limestone – Bowmanville quarry (Ghazvinian et al., 2013)

The anisotropy models suggest that anisotropy angles, 90° and 45° represent the upper and lower bounds for rock strength and the ratio between the two is often termed as the coefficient of anisotropy or anisotropy factor (Shea and Kronenberg, 1993). Other authors define anisotropy factors based on other rock properties such as point load index (Tsidzki, 1990) and transversely isotropic elastic constants (Kwasniewski, 1984).

Despite the extensive ongoing studies on the behavior of anisotropic rocks, it is noted that most geotechnical design methods are largely developed for isotropic conditions, often with minor adjustments to cater for the inherent heterogeneity and imperfections such as fractures and foliations. Research by many authors (e.g. Shea and Kronenberg, 1993; Vakili et al., 2014) suggest that highly anisotropic rocks can have an anisotropic factor greater than six. It is clear that the potential for anisotropic behavior cannot be overlooked in laboratory testing or geotechnical design. Table 3.1 is a generalized guideline of degrees of anisotropy for common rocks based on data compiled from various authors (see Vakili et al., 2014 for full list of authors).

Table 3.1. Classification of degree of anisotropy for various rock types. (Vakili et al., 2014)

Degree of Anisotropy	Example Rock Types	Anisotropy Factor
Isotropic	Quartzite, hornfels, granulite	1-1.1
Low anisotropy	Quartzofeldspathic gneiss, mylonite, migmatite, shale	1.1-2.0
Medium anisotropy	Schistose gneiss, quartz schist	2.0-4.0
High anisotropy	Mica schist, hornblend schist	4.0-6.0
Very high anisotropy	Slate, phyllite	>6.0

A first examination of the test results from Figure 3.2, organized based on a degree of foliation or bedding developed within the specimens shows a wider scatter compared to an organization based on either grain size or angularity. The influence of anisotropy on both compressive and tensile strength has been studied by several authors (e.g. Dan et al., 2013 for tensile strength of sedimentary rocks). An experimental study by Donath (1961) on Martinsburg slate in Pennsylvania indicated that under confining stresses ranging from 3 to 35 MPa, the compressive strength of slate increased by a factor of 3 depending on the inclination of foliation to the axis of loading. In all tests, the rock exhibited the highest strength at a foliation angle of 90° and lowest at an angle of 30°. It is therefore imperative to always consider the angle of foliation or bedding when interpreting test data of anisotropic rocks, (as suggested in the figures and procedures outlined by Hoek and Brown, 1980).

Defining the degree of foliation on its own does not adequately delineate a relationship, which in part could be related to the angle with respect to the loading direction that further complicates the relationship between tensile strength and UCS. Hoek and Brown (1980) suggested that for foliated rocks, mi cannot be a constant, but rather a function of the angle of foliation. Intact UCS and mi should thus be determined in the laboratory by strictly performing tests at right-angles to the foliation.

The analysis of the individual geological characteristics considered in this study does not yield clear trends with respect to the tensile strength or UCS relationship. It is however apparent that each individual parameter has some degree of correlation with other geological characteristics – hence the lack of clear trends when considered on their own merits. In order to examine these characteristics further, a subset of the data base, from Sweden, has been used and is discussed in the following section.

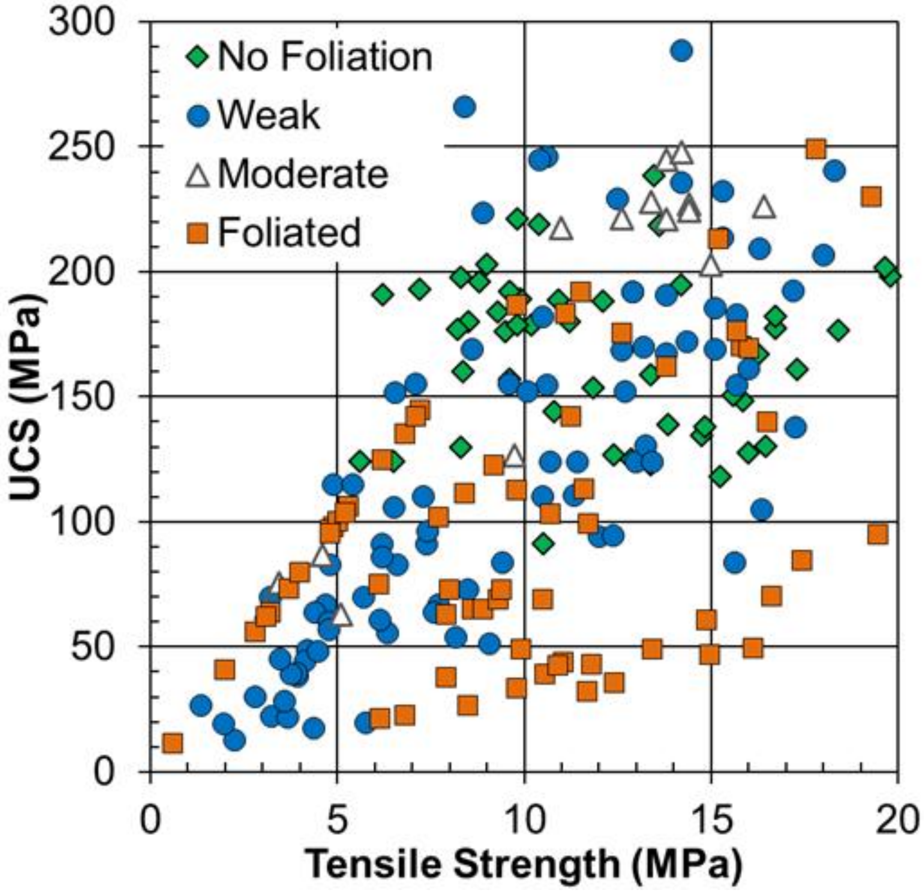

Figure 3.8. Tensile strength versus unconfined compressive strength (UCS) classified by degree of foliation or bedding developed within the specimen (modified from Perras and Diederichs, 2014)

3.3 Porosity

The porosity of a rock is a function of both the pores present in the rock and preexisting microcracks. Many authors have applied the Griffith fracture theory to define the relationship between rock strength and grain size. Hatzor and Palchik (1997) showed that the initial crack half-length in the Griffith equation (Eqn 8) depends not only on the grain size, but also on the porosity of the rock. The author's experiments suggest that direct correlations of grain size and UCS or tensile strength are only valid for homogenous samples in which grain size is the only significantly variable parameter. In heterogeneous rocks, pores may act as stress concentrators and so their presence cannot be ignored (Hatzor & Palchik, 1997).

The influence of porosity on strength has been studied in many other engineering materials including concrete (Nguyen, 1972), metals (Simone and Gibson, 1996), ceramics (Hattiangadi and Bandyopadhyay, 2000) and soils (Del Olmo et al., 1996). In all cases, higher porosity tends to weaken the material. Several models have been proposed for correlating a specific strength property to the porosity of the materials. One of the earliest expressions proposed is a power law function that relates tensile strength with porosity in metals Bal'shin (1949), defined by the expression;

$$\sigma_t = \sigma_{t0}(1-n)^{\lambda} \tag{9}$$

Where; n is the porosity of the material

λ is a material constant

σ_{t0} is the tensile strength of a non-porous variant of the material

The parameter λ is considered to vary for different materials as well. Figure 3.9(a) shows a graphical representation of the Eqn 9 for different values of *m*. Modification of the expression has been proposed by some authors to correlate porosity with other parameters such as the uniaxial compressive strength. Other existing generalized porosity-strength relationships exist in the form of power law or exponential functions (Hattiangadi and Bandyopadhyay, 2000; Tvergaard, 1981; Ryshkewitch, 1953). Three of these expressions are illustrated in Figure 3.9. Li and Aubertin, (2003) provides an extensive review of existing models that describe the relationship between porosity and material strength.

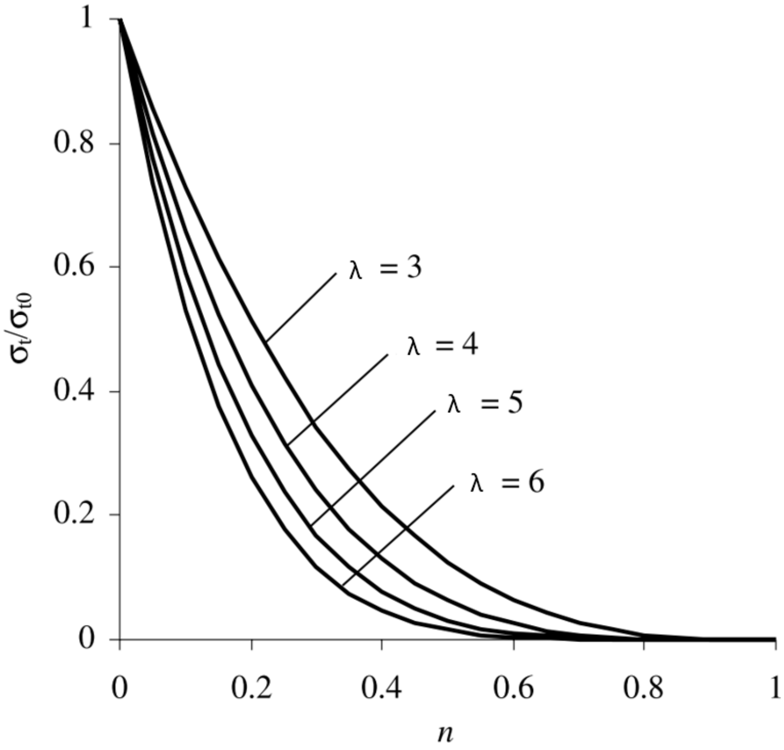

Figure 3.9. Tensile strength-porosity relationships according Bal'shin (1949) relationship (Eqn 9)

3.4 Grain Interlock

Grain interlock is intended to capture the influence of grain shape and grain interaction in controlling rock material breakage under shear or in tension. Depending on the character and strength of the matrix in a rock and the strength of the major mineral grains and their interlock with each other, grain boundary cracking may dominate over internal grain fracturing. Although defined as an individual parameter, interlock is in a complex way also inter-related with strength, porosity, and the clast to matrix ratio, such that it is proposed that it can be visually estimated depending on the rock type. Carter (2019) suggested that with a high interlock value, exceeding 10, cracking occurs through grains, whereas with a low interlock value, cracking occurs as a separation between individual grains.

Using the angularity or grain shape scale, the database of Perras and Diederichs (2014) was re-classified by visual inspection of the available results, as shown in Figure 3.10 and Figure 3.11 The two figures consist of a sample dataset of 10 rock types which forms a subset of the database in Figure 3.2. The subset was compiled based on the availability of sample pictures for visual inspection. The database contains rocks dominated by angular, sub-angular, and sub-rounded grains for the most part. Grouping the test results in terms of angularity suggests that while there may be a transition to lower strengths for more rounded grains, no clear distinction is evident in the data moving from sub-angular to angular.

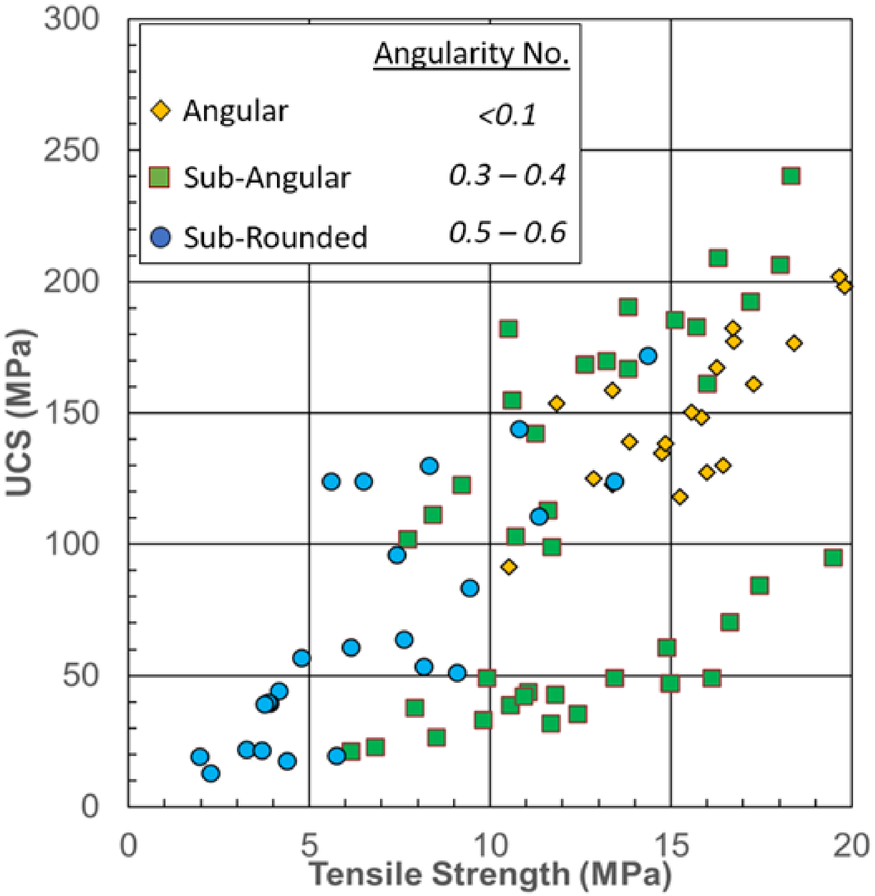

Figure 3.10. Tensile strength versus unconfined compressive strength (UCS) classified based on grain angularity (subset from Perras and Diederichs, 2014)

Grain interlock, which encompasses multiple grain properties, however, shows better segregation of data (Figure 3.11) than the angularity-based plot in Figure 3.10. This presents a good argument that individual sub-parameters such as angularity, matrix/clast ratio, etc., on their own do not fully govern the intergranular shear or tensile behavior of rocks. As the interlock % decreases from ±40% to less than 10%, the trend tends to steepen. A close examination of the data reveals that this segregation may be loosely tied to the origin of the rock, based on the author and rock type.

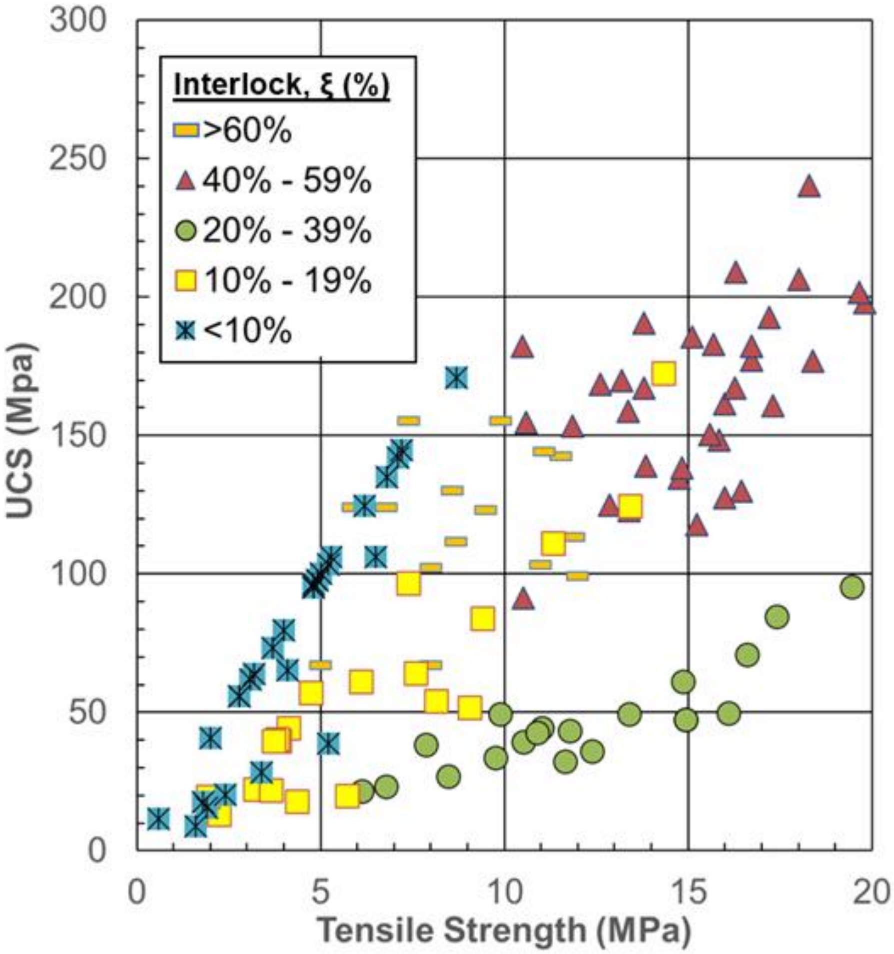

Figure 3.11. Tensile strength versus unconfined compressive strength (UCS) classified based on percentage interlock, ξ, (subset from Perras and Diederichs, 2014)

The sediment-derived rocks, including limestone and schist have a different trend than the crystalline rocks. The granitic rocks cluster together with the gneisses, which in the database used were derived from granites to form augen gneisses (Eloranta, 2006). Examining the clusters at higher interlock percentages suggests that some of the trends maybe more related to data availability, rather than interlock alone. However, this needs further study.

3.5 Water and Humidity

3.5.1 Stress Corrosion Cracking and Subcritical Crack Growth

Metals are known for their high ductility and strength, making them the largest group of construction materials across many industries. Their high tensile strengths and fracture toughness allow them to withstand high stresses throughout their operational life. Under certain conditions however, cracks may develop and grow slowly in some metals despite being subjected to stresses below their specified strength magnitude - a process known as subcritical crack growth (Maugis, 1985). A special case of subcritical crack growth in metals is a phenomenon known as Stress Corrosion Cracking (SCC). SCC is the sub-critical growth of cracks in a metal in a corrosive environment which results in failure under mechanical loading conditions in which fracture mechanics otherwise predicts that the metal is safe. According to Speidel (1975) the phenomenon was first reported in 1919. It is believed that under the right conditions, SCC may also occur in rocks as well (Brantut et al., 2013). The intrinsic heterogeneity of rocks makes it relatively difficult to study the process.

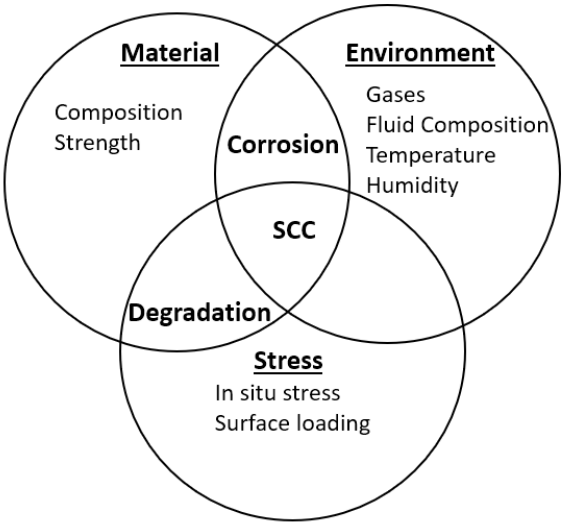

Figure 3.12. Simultaneous presence of tensile stress, susceptible material condition and critical corrosive solution required for stress corrosion (modified from Speidel, 1984)

For SCC to occur, three conditions must be met (Winzer et al., 2005): (1) Mechanical loading to induce stress, (2) a corrosive environment, (3) a susceptible material. All three conditions have to be simultaneously present in order for SCC to be possible. Experiments by several authors on different metals (Winzer et al., 2005; Singer et al., 2011; Rebak, 2011; Cheng, 2013; Ramamurthy and Atrens, 2013) indicate that the environment does not necessarily have to be highly corrosive to the metal for SCC to occur. Consequently, a metal may undergo SCC in a mildly corrosive environment while still looking new and shiny, which makes it very difficult to detect. This is especially problematic in large machines such as airplanes, where tiny cracks may easily go unnoticed. Due to differences in material chemistry and microstructure, different metals and alloys respond differently to different corrosive environment as applied to SCC.

As is illustrated in Figure 3.12, other forms of material defects can occur when only two of the above-mentioned conditions are present. Corrosion is a mostly chemical damage process, rusting being a very common example. Corrosion usually leaves a strong visual impression including colour changes, deformity of the affected area and an accompanying strength loss and is easier to detect than SCC. Degradation is the mechanical loss of strength or integrity of a material due to the application of stress. Different forms of degradation can occur depending on the magnitude of applied stress and its mode of application. Examples loading conditions that lead to degradation include: (1) Fatigue - the progressive growth of microcracks that results from cyclic loading of a material, and (2) Creep - the slow deformation that is caused by the application of a persistent mechanical load (Tomor and Verstrynge, 2013).

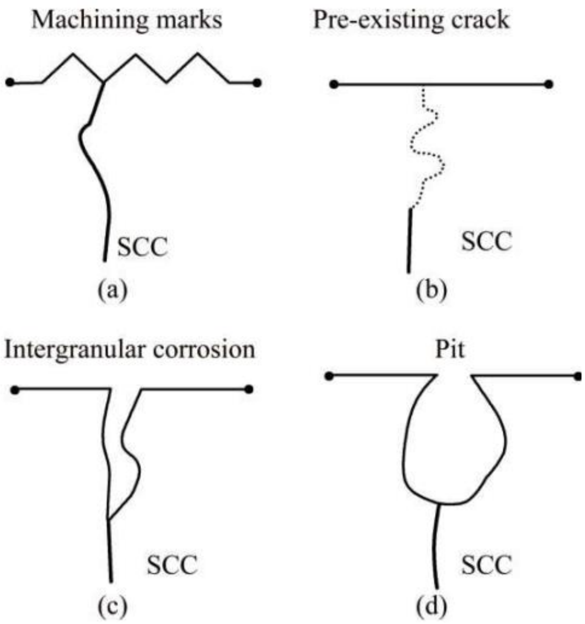

Figure 3.13. Types of SCC initiation sites: (a) machining marks; (b) pre-existing cracks; (c) intergranular corrosion (d) corrosion pit

Oftentimes, SCC will initiate from already existing structural imperfections such as a pre-existing crack or from certain geometrical features such as sharp corners. The various identified SCC initiation sites are illustrated in Figure 3.13. The figure shows that damage previously caused by only two prerequisites of SCC (i.e, corrosion and degradation as previously described) can be a precursor to SCC.

In rocks, SCC has been recognized as one of the driving forces of time dependent rock failure (Brantut et al. 2013). This can affect the long-term integrity of underground mines and excavations. Fluids are also known to be transported to preexisting cracks in rocks and time dependent changes in crack size and density can significantly affect fluid transport properties.

Although not always explicitly described as SCC, accelerated crack growth have been observed in certain environments. Studies on these environments have however mostly been limited to water and humid air.

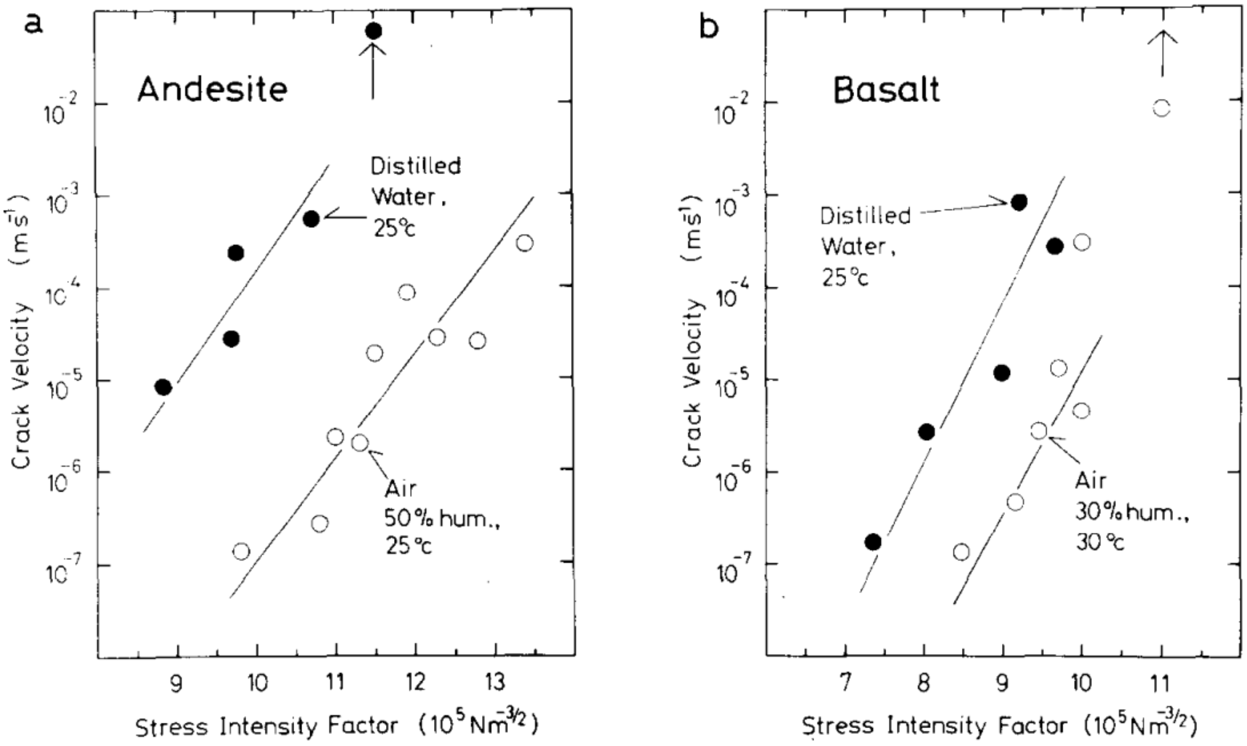

Figure 3.14. Crack velocity as a function of stress intensity factor for (a) andesite and (b) basalt in both saturated and ambient conditions (Waza, Kurita, & Mizutani, 1980)

The effect of water on subcritical crack growth was investigated by Waza et al. (1980) on andesite and basalt rock samples. The rate of crack propagation was measured separately on water saturated and air-dry samples using the double torsion method. The results (Figure 3.14) show that crack velocity in either samples increased by 1 to 3 orders of magnitude when submerged in distilled water and it was concluded that SCC occurs due to weakening of the siloxane bond at the crack tips in silicate rocks.

CHAPTER 4. DETERMINATION OF HOEK-BROWN m_i

4.1 Laboratory Determination of m_i

With the knowledge of the various factors that influence rock strength, a feasible method of obtaining rock strength information that accounts for this grain influences is desired. It is generally considered that the Hoek-Brown material constant, m_i is the parameter that reflects the individual material variation between different rocks. This section examines a potentially cost-effective procedure that can be used to make estimates of the m_i parameter using only sample photos and a few compressive and tensile strength tests, so that they can be used as a first pass in the early stages of a project more sophisticated test results (such as a the triaxial test) is not yet available. A database consisting of rocks whose laboratory test data, as well as sample photos are available, is gathered with the aim of making comparisons between the visual parameter estimates and calculated values from their corresponding laboratory test results.

4.1.1 Sources of Laboratory Test Samples

The rocks from which laboratory test data were obtained originate from two locations: Forsmark, Sweden and Ontario, Canada. Laboratory work performed on rocks from Forsmark were performed by the Swedish Nuclear Fuel and Waste Management company (SKB). SKB manages and safely disposes off wasted from nuclear power plant in Sweden. SKB operates in three places in Sweden (see Figure 4.1), including Forsmark, where a repository for short-lived radioactive waste is located.

Figure 4.1. Map of Sweden showing the three SKB operation locations

The samples labelled Cobourg are limestones from the Appalachian and Michigan sedimentary basins, which are separated by the Algonquin arch as shown in Figure 4.2 (Mazurek, 2004). The limestone is the proposed host rock for a low and intermediate level Waste Deep Geologic Repository (DGR) at the Bruce nuclear site near Triverton, Ontario.

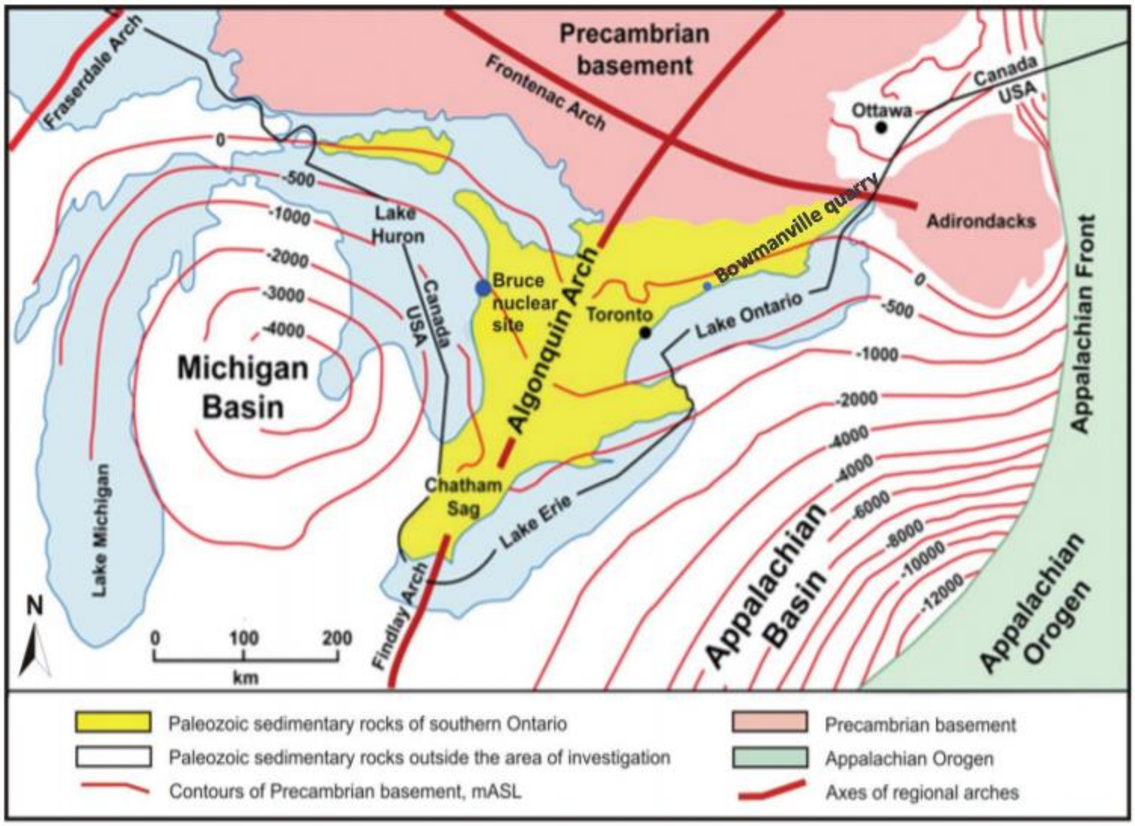

Figure 4.2. Large scale tectonic elements in Southern Ontario and the sedimentary rock depth contours of the Michigan and Appalachian Basins in which the Cobourg is a Formation (Mazurek, 2004) and the locations from which the two sets of Cobourg samples came from, the Bruce nuclear site and the Bowmanville quarry

4.1.1.1 Geology of the Forsmark Site

Data on the geology of the Forsmark site has been accumulated over several years through surface and bedrock mapping, and drilling activities. The field data continues to be used in mineralogical, geochemical and petrophysical work in order to identify a suitable bedrock for construction of the repository at an elevation of approximately 500 m (Stephens, 2010 – R-10-04). The Forsmark region is characterized by a gentle relief landscape with the ground surface covered by unconsolidated Quaternary and post-glacial deposits. The major rock units in the Forsmark region can be divided into four major groups (groups A to D) based on their relative age relationships, as shown in Figure 4.3 and summarized in Table 4.1.

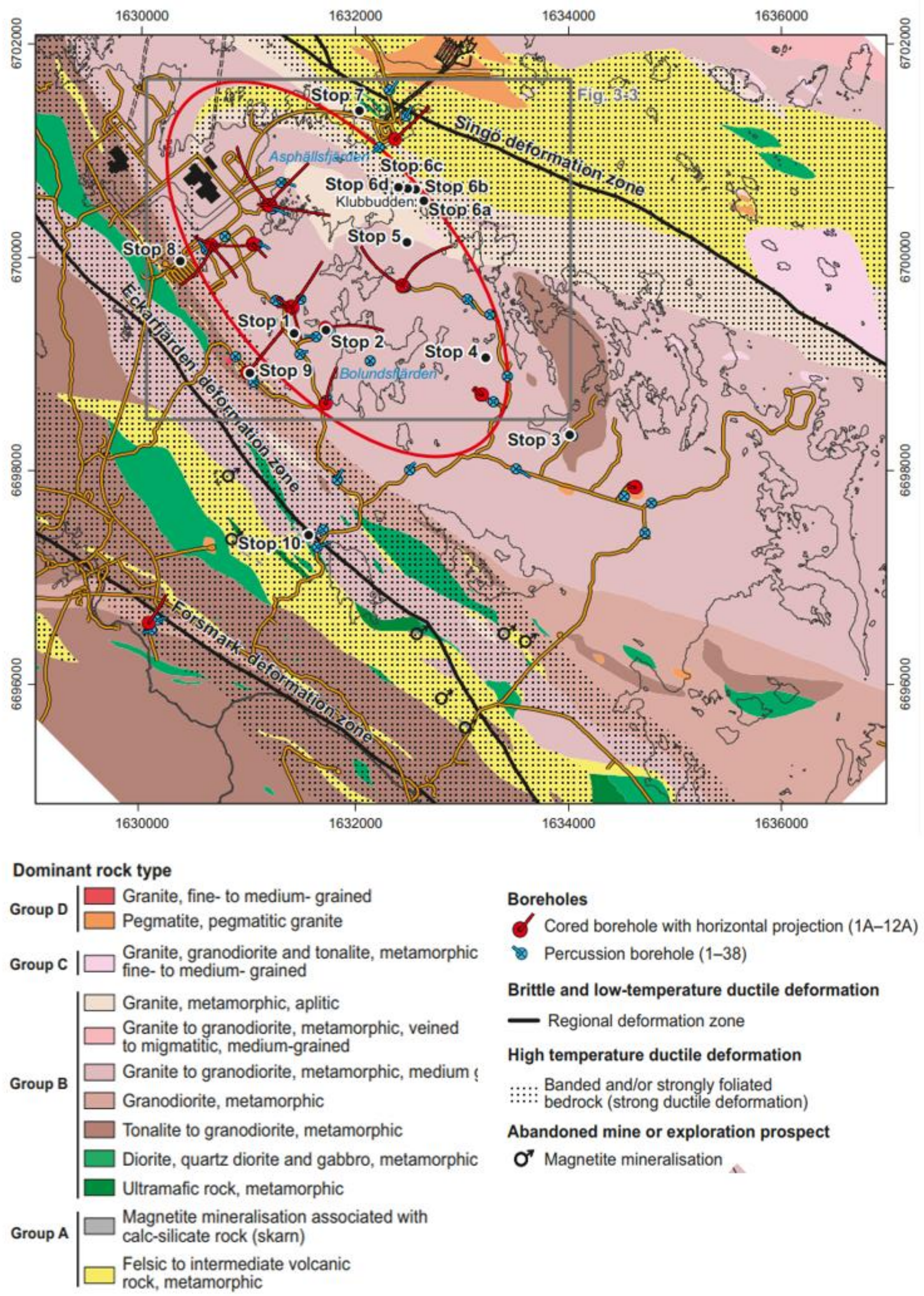

Figure 4.3. Bedrock map of the Forsmark site

Table 4.1. Major rock groups and rock units at the Forsmark site (Stephens et al. 2005)

Rock Group	Dominant Rocks	Subordinate Rocks
D	- Granite - Pegmatite	Granite and pegmatite dykes
C	- Granite - Tonalite - Granodiorite	Metagranitoid as dyke
B	- Granite - Tonalite - Granodiorite - Diorite	Amphibolite, metamorphosed diorite
A	-Felsic to intermediate igneous rocks	Calc-silicate rocks

Each major group consists of at least two different major rock types. The bedrock is dominated by meta-intrusive rocks formed between 1.85 and 1.89 Ga. In general, the rocks across the four groups different variations of granitoids over a wide range of degrees of metamorphism. Rocks in groups C and D show a lower degree of metamorphism than those in groups A and B. In addition to the granitoids, rock groups C and D include subordinate felsic to ultrabasic rocks which metamorphosed under amphibolite facies conditions.

4.1.1.2 Geological Setting of Cobourg Limestone

The Cobourg formation is an Ordovician argillaceous limestone with light grey, calcite-rich nodules surrounded by dark-grey, clay-rich grains with fossils in the inter-nodular layers. Outcropping bedrock in southwestern Ontario consists of clastic and carbonate rocks which were deposited in the Michigan and Appalachian basins (Frizzell et. al., 2008). The two basins are separated by the Algonquin arch with the Michigan basin on its west side and the Appalachian basin to the east. The two basins were formed in similar environments in the middle Ordovician period, when the Cobourg limestone was deposited.

The sequence within which the Cobourg limestone was deposited is the Trenton group. Within the Trenton group, the Cobourg formation is overlain by the Upper Ordovician shale Formations of the Blue Mountain, Georgian Bay and Queenston, and is underlain by Middle Ordovician limestones that site on top of the Cambrian sandstone and Precambrian basement rocks.

4.2 Determination of Hoek-Brown Envelopes

Laboratory test data from the Swedish Nuclear Fuel and Waste Management Company (SKB) served as the major part of the dataset for which comparisons between estimated m_i's using both the photo-analysis and curve fitting approaches are made. The rocks examined were all medium to coarse grained rocks of the granite family, obtained at the Forsmark site. The data set included Brazilian tensile strength (BTS), uniaxial compressive strength (UCS), porosity and triaxial tests performed for at least four confining pressures, performed from 2004 to 2007. All the geomechanical tests were carried out under similar conditions. A summary of all rock types used in this study is shown in Table 4.2.

Table 4.2. Summary of database of rock types and laboratory test types used in the determination of m_i parameter

Rock Type	Test Type	References
Avro Granite	BTS	Jacobsson, 2004 (P-04-263)
	UCS	Jacobsson, 2004 (P-04-261)
	Triaxial	Jacobsson, 2004 (P-04-262)
Medium Grained Granite	BTS	Jacobsson, 2005 (P-05-98)
	UCS	Jacobsson, 2005 (P-05-97)
	Triaxial	Jacobsson, 2005 (P-05-100)
Granite-Granodiorite	BTS	Jacobsson, 2004 (P-04-173)
	UCS	Jacobsson, 2004 (P-04-225)
	Triaxial	Jacobsson, 2004 (P-04-229)
Granodiorite-Tonalite	BTS	Jacobsson, 2004 (P-04-173)
	UCS	Jacobsson, 2004 (P-04-225)
	Triaxial	Jacobsson, 2004 (P-04-229)
Tonalite-Granite	BTS	Jacobsson, 2004 (P-04-173)
	UCS	Jacobsson, 2004 (P-04-225)
	Triaxial	Jacobsson, 2004 (P-04-229)
Cobourg Limestone	BTS, UCS and Triaxial	Gorski et al., 2010 (TR-08-24)
Cobourg Limestone	Sample pictures	This study
Bedretto Granite	BTS	Keller and Schneider, 1982
	UCS	Huber, 2004
Pegmatite	BTS	Jacobsson, 2005 (P-05-121)
	UCS	Jacobsson, 2005 (P-05-120)
Diorite/Gabbro	BTS	Jacobsson, 2006 (P-06-38)
	UCS	Jacobsson, 2006 (P-06-37)
Quartz Monzodiorite	BTS	Jacobsson, 2006 (P-06-271)
	UCS	Jacobsson, 2006 (P-06-270)
Albitic Granite	BTS	Jacobsson, 2007 (P-07-146)
	UCS	Jacobsson, 2007 (P-07-145)

Mechanical tests for BTS were carried out by the Swedish National Testing and Research Institute in a load frame where the crossbar is mechanically driven by screws and has maximum load capacity is 100 kN in compression. The axial compressive loads are measured by an external 100 kN load cell with an uncertainty of less than 1%. The frame is equipped with a pair of curved bearing blocks, radius 39 mm and width 29 mm, with pins for guiding the vertical deformation (see Figure 4.4).

The UCS and triaxial tests were also carried out by SP Swedish National Testing and Research Institute in a servo-controlled testing machine specially designed for rock tests which comprises a load frame, a hydraulic pump unit, a controller unit and various sensors. The system allows the UCS of rocks as well as their elastic parameters, represented by Young's modulus and Poisson's ratio. The axial load is determined using a load cell, which has a maximum capacity of 1.5 MN and uncertainty of less than 1%. Rock deformation is measured with calibrated LVDTs with measurement range of ± 2.5 mm. Axial deformation is measured with an assembly that consist of two aluminium rings attached to the specimen and an LVDT pair that measures the distance between the aluminium pair.

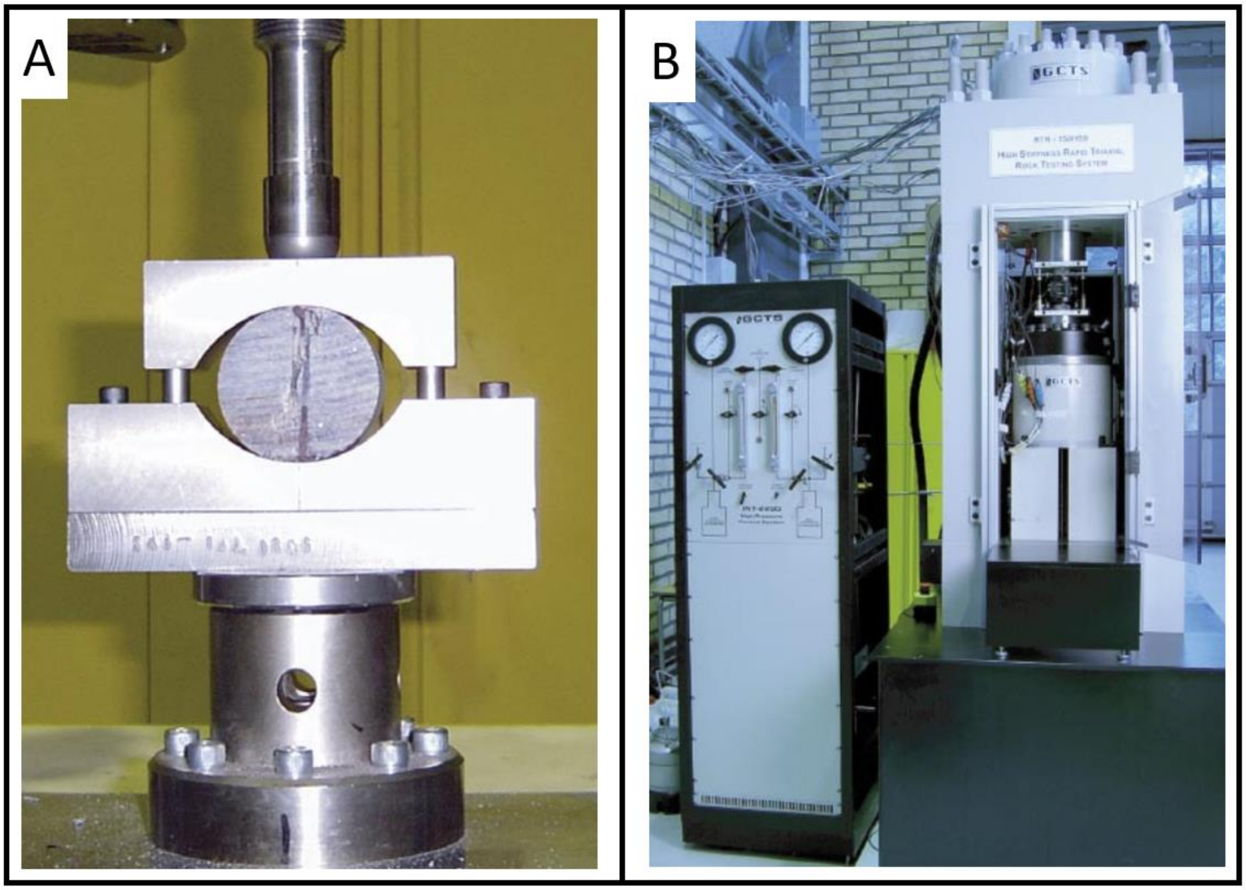

Figure 4.4. Rock testing apparatus showing (A) loading frame for BTS tests, (B) servo-controlled system for UCS and triaxial tests

For an intact rock, the original Hoek-Brown envelope uses laboratory test results to determine the values of parameters, σ_c and m_i, while the parameter a and s are fixed to constant values of 0.5 and 1 respectively. The parameters are used to produce a strength envelope that defines the intact rock strength under tensile and compressive conditions.

4.2.1 Determining m_i by Regression Analysis

Regression analysis is a powerful tool for establishing empirical relationship between two or more variables. In the case of the Hoek-Brown criterion, the variables are the major and minor principal stresses, which define the stress state of a rock. It is recommended the regression be performed on sets of BTS, UCS and triaxial tests to determine the m_i parameter. There are several curve fitting methods that are frequently used in the rock engineering community to develop failure envelopes for rocks. While all of them exist to achieve the same purpose, differences in their nature results in subtle differences in m_i's obtained for the same dataset. One of the most important distinctions that has to be noted for a Hoek-Brown regression is that unlike for other typical linear or nonlinear regressions, the direction of residuals in a Hoek-Brown regression is not constant through the entire dataset. In the tensile region, errors and residuals occur in the direction of σ_3, whereas the errors and residuals occur along σ_1 in the uniaxial and triaxial regions, as illustrated in Figure 4.5.

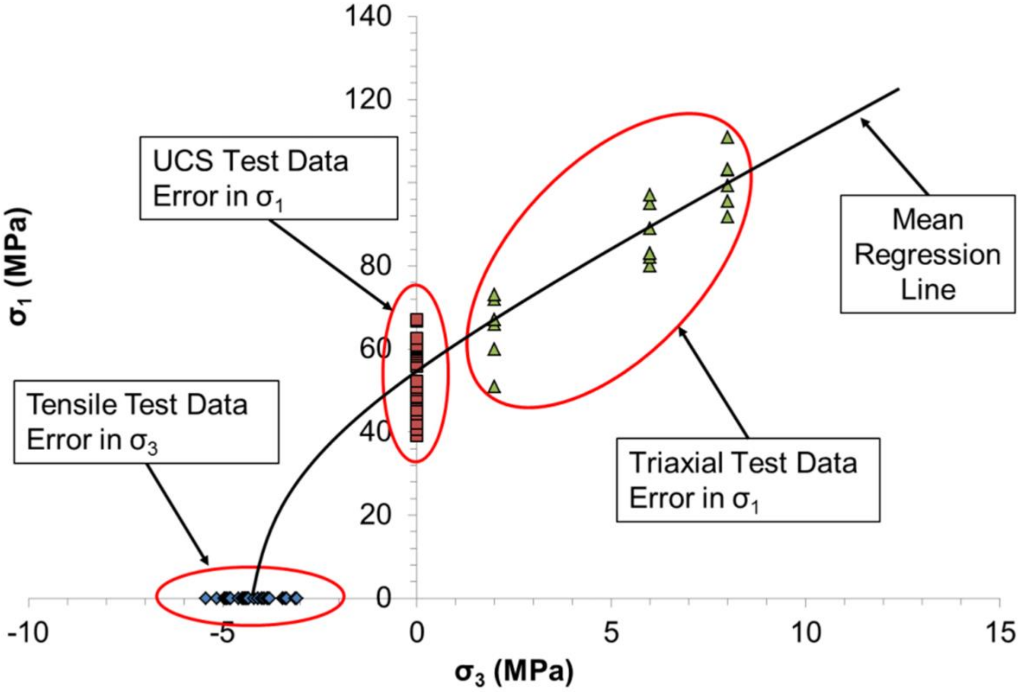

Figure 4.5. Principal (σ1-σ3) stress space showing triaxial, uniaxial and tensile test data and their corresponding directions of error (from (Langford, 2013).

In statistical modelling, linear regression is one of the simplest approaches to estimating the relationship between an independent variable and a dependent variable. The regression approach assumes that the relationship between the two variables is linear. The most common approach to fitting a line through a dataset is by the ordinary least squares method, which calculates the regression line by minimizing the sum of the distances between the true data points and the regression line. This method can be applied on a laboratory dataset to determine the Hoek-Brown envelope, despite the envelope being nonlinear. This is achieved by transforming all triaxial, UCS and tensile data points into a linear stress space such that the Hoek-Brown failure envelope transforms into a linear function of the form y = ax + b, where;

$$y = (\sigma_1 - \sigma_3)^2 \tag{10}$$

$$x = \sigma_3 \tag{11}$$

$$a = m_i * \sigma_c \tag{12}$$

$$b = {\sigma_c}^2 \tag{13}$$

Using the vertical error summation method, the regression solutions, *a* and *b* are solved, from which the parameters m_i and σ_c can be derived. RocData allows the sum squared residual (RSS) to be computed either as absolute or relative values (see Figure 4.6). Relative residuals allow normalization of the errors to σ_3. This is sometimes necessary because in triaxial datasets that span across a wide range of confining pressures, errors may increase with larger values of σ_3.

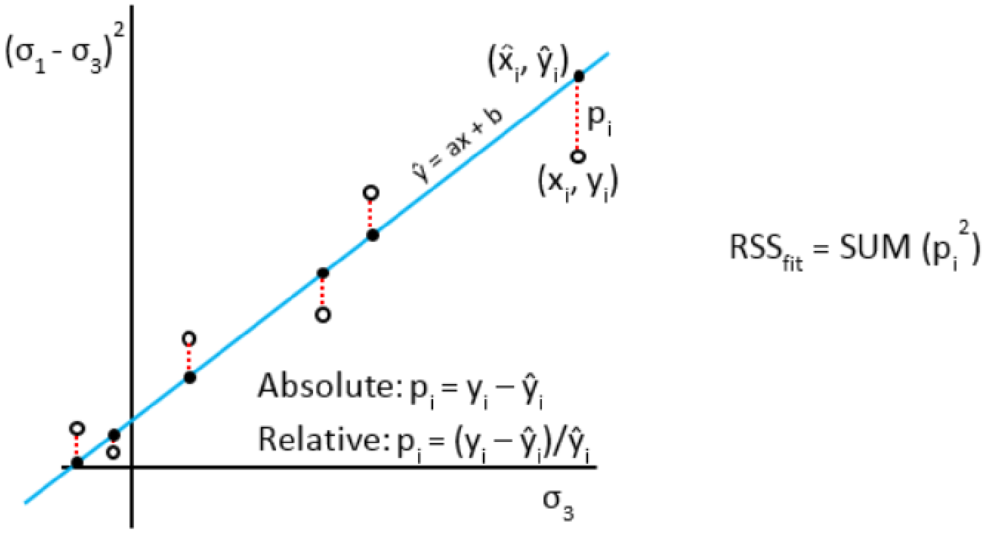

Figure 4.6. Illustration of linearized Hoek-Brown strength envelope. Regression is performed using the ordinary least squares method by minimizing the sum squared residuals (RSS_{fit})(Langford, 2013)

4.2.2 An Empirical Equation for Calculating the Material Constant

In the classical definition of the Hoek-Brown failure criterion, the material constant, m_i is considered to be a function of the fabric and granular properties of a rock. The implication is that the m_i constant is subject to a higher degree of variability for any given rock type due to the inherent heterogenous nature of rocks. Analysis on existing databases on rock material properties by Richards and Romana, (2011) showed that there is a poor correlation between rock lithology and m_i values (see Figure 4.7). Carter and Marinos, (2020) considers this as a strong reason for rock engineering practitioners to put more focus on the geological characterization of project sites in order to improve the definition of key input parameters in numerical models. Individual influences on the m_i parameter and the overall strength of rocks have been discussed in Chapter three of this thesis.

Based on regression analysis of existing rock data and a compilation of various studies on the strength dependence on rock material parameters, Carter and Marinos (2020) formulated an expression that relates m_i with groups of controlling parameters that captures the variability in different rock type conditions. The expression is defined as;

$$m_i \cong f\left(\left(\frac{\sqrt{d}, \xi}{\psi, \varphi^g}\right) . \left({}^{\sigma_c}/_{|T|}\right)^{-log k_{G\phi}}\right) \tag{14}$$

The expression takes into consideration the influence of interlocking grains or crystals, ξ, the modal grain size, d, fabric anisotropy, ψ, void content or porosity, φ, and a Kurtosis modifier term, $K_{G\phi}$, to describe uniformity and intermixing characteristics of the grains within the rock. The expression is intended to serve as a modification of the power relationship obtained through linear regression analysis by Hoek and Brown, (2019);

$$m_i = 1.2R^{0.8} \tag{15}$$

Where R is the Sheorey quotient, defined as

$$R = \frac{\sigma_c}{|T|} \tag{16}$$

Based on optimization through multiple regression checks on the groupings of the parameters Carter (2020) finalized Eqn 14 as;

$$m_i = (1+\xi).\{d^{0.5}.(1.001-\psi)\}^{0.16}.(1.2-\varphi^{0.5}).\left({}^{\sigma_c}/_{\sigma_T}\right)^{(0.8-logK_{G\phi})} \tag{17}$$

Each term in the expression serves as modifier to the Sheorey quotient that captures the influence of a specific rock material parameter, as detailed below.

1. **The interlock term, $(\mathbf{1}+\boldsymbol{\xi})$ -** Expressed as a percentage increase to the value of m_i based on the degree if interlock and angularity of crystal grains. The effect of interlock

on rock strength gets magnified in porphyritic rocks in which larger grains (phenocrysts) are contain in a matrix of fine-grained ground mass.

2. **Grain Size Term,** ($\boldsymbol{d^{0.5}}$) – The strength scaling of rocks with grain size is considered by many authors to be governed by the Hall-Petch relationship. This relationship has been empirically demonstrated in pure metals and alloys (Cordero et. al., 2016).
3. **Anisotropy,** ($\boldsymbol{1.001 - \psi}$) – The presence of anisotropy in the form of foliations or layers tend to decrease the overall strength of rocks since they serve as planes of weaknesses along which grains can easily slip past each other. However, as demonstrated by Ghazvinian et. al, (2013), rock strength degradation is merely a function of type and number of planes. It is strongly dependent on the axis of loading, relative the existing planes of weaknesses.
4. **Porosity,** ($\boldsymbol{1.2 - \varphi^{0.5}}$) – Archie's first law (Archie, 1942) is used in petroleum engineering to calculate the cementation exponent of rock units, which can be used to estimate the porosity of the rock.

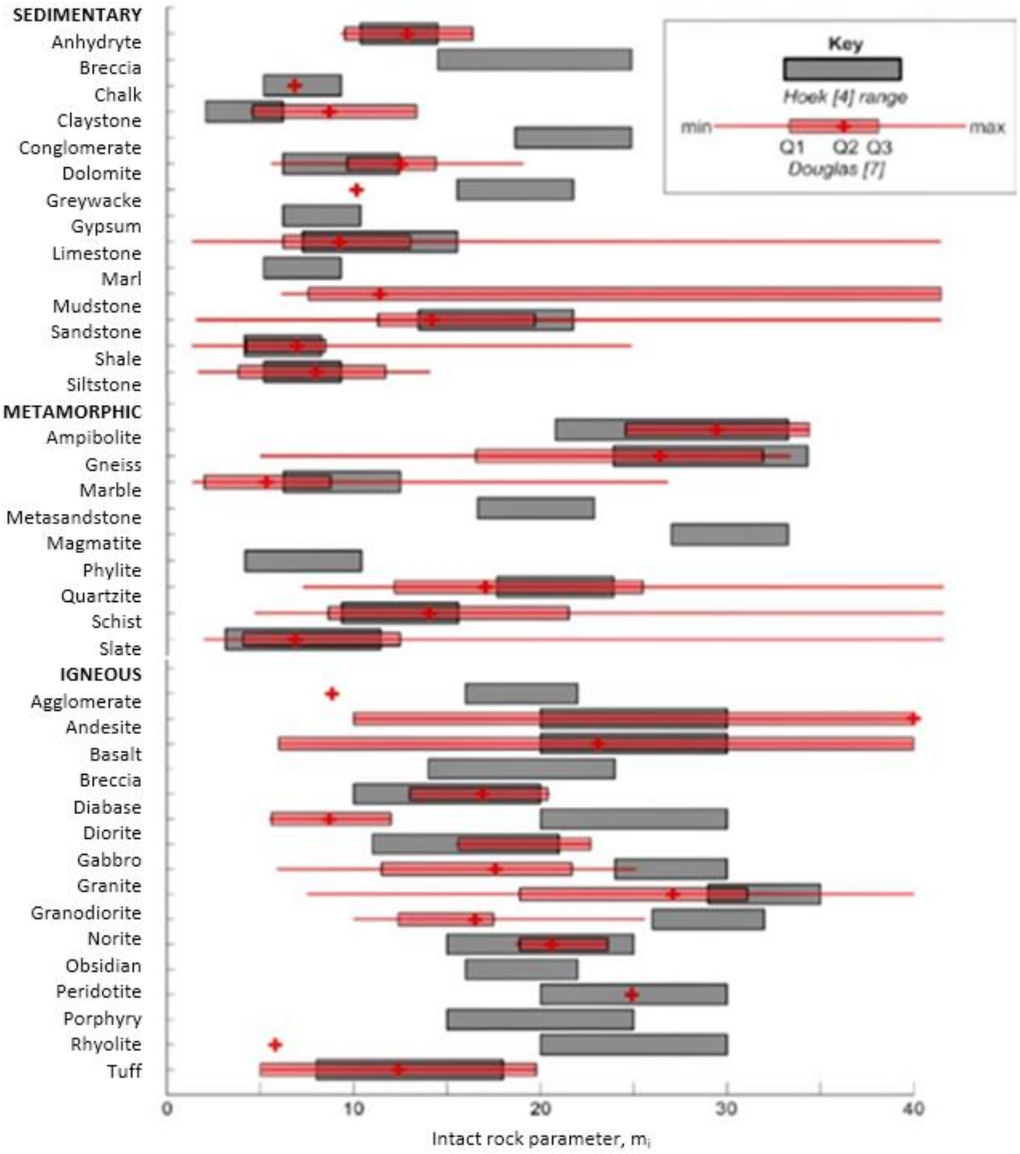

Figure 4.7. Box plot of measured m_i ranges for different rock types compared with Hoek, (1999) tabulations (from Richards and Romana, (2011)

4.2.3 Photo-Analysis

Determining grain size and interlocking characteristics, as well as other geological characteristics of a rock sample, is rare in most rock engineering lab testing, but can be achieved relatively straightforwardly using thin sections, scanning electron microscopy, or other rock surface digital imagery and/or visual inspection techniques. Digital analysis of optical and scanning electron microscope imagery is one of the preferred techniques nowadays in the metallurgical testing field as it can be accurately implemented at a wide variety of scales. However, for coarser grained samples the same techniques can be applied for analyzing pictures of outer surfaces of samples as an aid to quantifying visible geological factors that may influence intact rock strength.

A software program called ImageJ, an open-source photo-analysis software (Ferreira and Rasband, 2012), can be used to process a batch of photos to examine the percentage of grain types within a sample, sufficient to determine grain size distributions and even fabric angle orientations. An example of the steps to identify quartz content within a graphitic schist sample is shown in Figure 4.8. The first step is to take the raw image and digitally process it to remove any imperfections such as small saw scratches, uneven lighting, and shadows. This is accomplished by modifying the color balance of the image, separating and editing color channels, and performing pixel-level mathematical operations, either on a local distorted region or the entire image. After small imperfections are removed, the contrast is increased to make minerals more distinguishable and grains more defined.

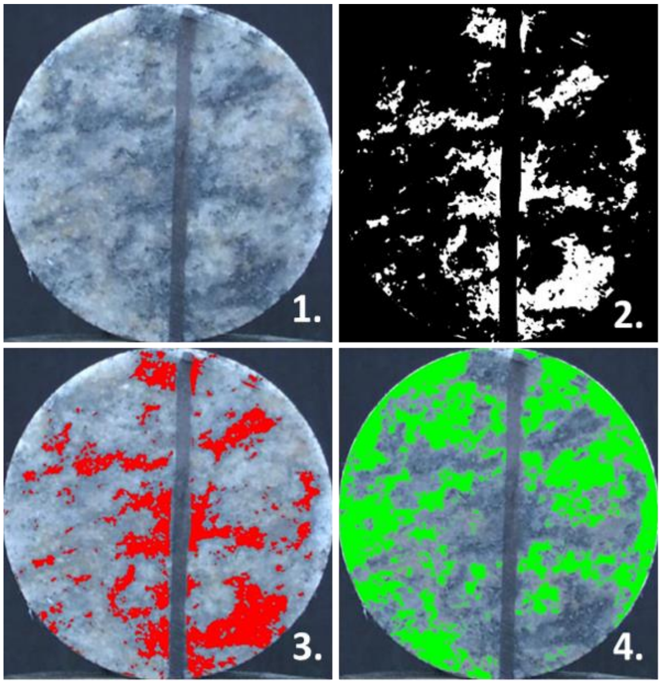

Figure 4.8. Example photo analysis on medium grained granite to determine the percent mineral content by taking the raw image (1), processing it to remove surface markings, converting it to a grayscale and thresholding it to obtain a binary image (2), counting the percentage of the red areas to obtain the mineral content (3) and different threshold ranges to identify different mineral content in the sample (4) (Jacobsson, 2005)

The image is then converted to 8-bit grayscale, where pixel intensity values are set to vary from 0 (black pixels) to 255 (white pixels) with values in between being linearly varying shades of gray. Different minerals will thus occupy different grayscale ranges and by thresholding the image, the minerals of interest can be selected. The result of the thresholding process produces a binary black and white image (Figure 4.8(2)), with white pixels denoting the pixels of the image that lie within the threshold limits and black pixels representing the pixels that fall outside the threshold limits that represent the mineral in question.

The thresholding process is used to digitally filter out different minerals one at a time from the rock sample. Figure 4.8(3) and Figure 4.8(4) show two different minerals filtered from the rock sample by setting two different threshold ranges. The red and green highlighted areas are the pixels of the image that correspond to a specific mineral within the rock. The ratio of the highlighted pixels to the total number of pixels within the rock sample is the corresponding mineral’s content of the rock sample. Since the relative mineral content can vary within the rock sample, the above process is repeated across images taken from different sides of the sample. Averaging the results obtained for each side gives a more accurate estimate of a mineral’s content within the rock. If the quality of the picture is adequate, the grains of the rock are clearly visible in the picture, and a reference length, such as a ruler, exists in the photograph, the above process can be used to measure the grains’ average size and their distribution across the sample. By setting appropriate thresholds to filter out the grains from the rock sample, the software can count the number of pixels that fall within a grain. Using the reference length in the image, a unit of length can be mapped to a pixel’s length. By counting the number of grains in the image, their relative size in pixels per grain and the pixel-to-real length ratio, the grain size and their distribution can be obtained for the sample.

Using the above techniques if good photographs has been taken of laboratory samples, one can extract grain size character and distribution and other geological indications in a relatively straightforward manner. The application of the types of photo analysis explained above to examine geological characteristics of all rock samples being tested for routine lab tests (such as UCS) would however be more effective industry-wide if a universal standard procedure could be developed and then adopted for taking the photos. Thin sections and photos from them should also be produced alongside undertaking the normal procedures for the testing so that overall characteristics of each tested sample can be better determined than in current practice. The trend from just testing to collect numbers back to testing to establish and understand geological variability needs to be reversed. We need to regain lost insight regarding how geological characteristics control rock strength test results.

4.3 Estimation of Parameter Values

The effectiveness of the novel technique depends not only on the availability of high-quality photos, but also on an established procedure for parameter estimation that is consistent and repeatable. In this research the ImageJ software was used to estimate the values of grain size and kurtosis modifier terms, while the remaining parameters were estimated by direct observation of sample photos and existing laboratory data. Ideally sample photographs should be taken orthogonal to the rock surface with a scaling tool such as a ruler visible in the image. ImageJ is an automated recognition software that significantly reduced to time required identify grain boundary, compared to a user manually identifying boundaries. However, care much be taken to ensure the accuracy of the digital rock boundaries and adjustments made as necessary.

4.3.1 Grain Size, d

Grain size is one of the most recognized parameters for describing rock material composition. As was previously discussed in chapter three, the magnitude of the grain size parameter is expressed as the most commonly occurring (modal) grain size in the rock. ImageJ software cannot directly measure the diameter of a closed grain boundary. It measures the 2D surface area, from which the equivalent diameter is calculated. In fact, the term “grain size” on its own is ambiguous since the measured diameter of a grain is dependent on the direction of measurement, especially for grain with very eccentric shapes. Any individual grain will have a diameter between a minimum and maximum limit, depending on the axis of measurement relative to the grain shape. In this study the grain sizes are obtained by computing the equivalent diameter of assumed area equal to area of the grain. It is obvious that this calculated value completely ignores the shapes of the grain. However, the influence of grain shapes are accounted for by the interlock (ξ) and anisotropy (ψ) parameters.

4.3.2 Grain Interlock, ξ

The grain interlock component is represented as a percentage increase or decrease in the overall m_i based on the extent of frictional resistance between the rock grain. Studies show that grain interlock is inter-related to porosity, grain angularity and clast to matrix ratio (Richards and Read, 2011; Cowie and Walton, 2018). Angular grains tend to interlock with each other and offer a higher resistance to shearing, thus resulting in higher m_i. Since the interlock parameter depends strongly on the level of contact between mineral grains, the percentage of phenocrysts present in the rock has an influence on the magnitude of the parameter. The percentage interlock value can be visually estimated following the guidelines shown in Figure 4.9(A).

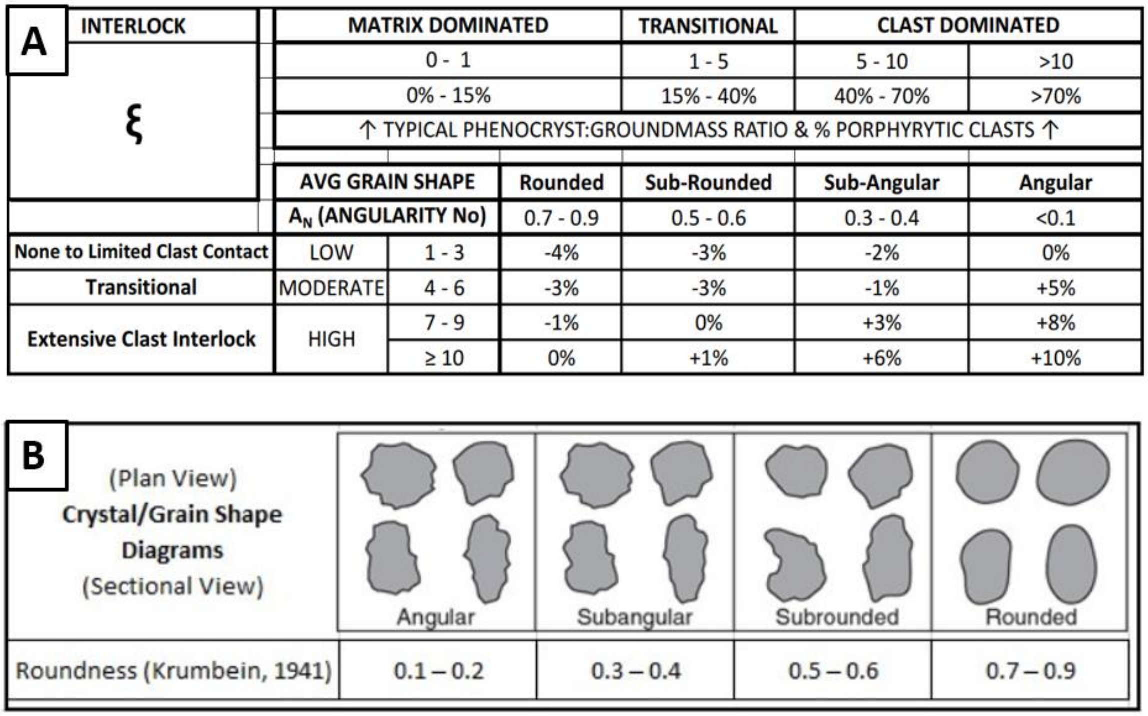

INTERLOCK	MATRIX DOMINATED			TRANSITIONAL	CLAST DOMINATED	
ξ	0 - 1			1 - 5	5 - 10	>10
	0% - 15%			15% - 40%	40% - 70%	>70%
	↑ TYPICAL PHENOCRYST:GROUNDMASS RATIO & % PORPHYRYTIC CLASTS ↑					
	AVG GRAIN SHAPE		Rounded	Sub-Rounded	Sub-Angular	Angular
	A_N (ANGULARITY No)		0.7 - 0.9	0.5 - 0.6	0.3 - 0.4	<0.1
None to Limited Clast Contact	LOW	1 - 3	-4%	-3%	-2%	0%
Transitional	MODERATE	4 - 6	-3%	-3%	-1%	+5%
Extensive Clast Interlock	HIGH	7 - 9	-1%	0%	+3%	+8%
		≥ 10	0%	+1%	+6%	+10%

Roundness (Krumbein, 1941)	0.1 – 0.2	0.3 – 0.4	0.5 – 0.6	0.7 – 0.9

Figure 4.9. (A). Definition interlock component as a function of angularity and clast to matrix ratio,(Carter, 2020). A visual guideline for the estimation of angularity No from (Krumbein, 1941) is provided in (B)

Rocks containing fewer phenocrysts separated by a sea of matrix will have a lower area of contact, resulting in lower interlock values. The figure above gives an estimate of the parameter by taking both the overall angularity of mineral grains and matrix to clast ratio, with typical values ranging from -4% to 10%. Carter (2019) suggested that with a high interlock value, exceeding 10, cracking occurs through grains, whereas with a low interlock value, cracking occurs as a separation between individual grains resulting in a rolling failure. The angularity numbers in the table is are adapted measurements of roundness, as defined by Krumbein (1941) as a measure of the curvature of the corners of a sedimentary particle expressed as a ratio of the average curvature of the particle as a whole. While it will be most ideal to use a software to measure this “roundness” parameter, the software has to be independently capable of identifying the corners of each grain. The ImageJ software is not suitable for this process. Therefore, it was decided in this this study to make estimates of this parameter visually, based on Carter's (2020) visual guideline shown in Figure 4.9(B).

4.4 Visual Vs. Laboratory m_i Values

The first step in assessing the feasibility of the photo-analysis procedure is by comparing visual estimates of m_i with their corresponding laboratory estimated values. The primary image dataset for testing the image-analysis procedure consisted of the five granitic rocks obtained from SKB, and Cobourg limestones from the Bowmanville quarry, whose m_i parameters were calculated from existing laboratory data. It is important to note that the laboratory test data for the Cobourg limestones were collected from rock samples obtained from sedimentary bedrock at the Bruce site near Kincardine, Ontario, where a Deep Geologic Repository (DGR) has been proposed by Ontario Power Generation (OPG). However, sample pictures on which the photo-analysis procedure were performed are Cobourg limestones that originate from the

Bowmanville quarry. Based on mineralogical analysis using X-ray diffraction (XRD) and Scanning Electron Microscopy (SEM) performed by Day (2016, 2017), the only difference between the limestones from the two sites appears to be the relative proportion of the clay matrix compare to the other constituent minerals such as Calcite and Ankerite, as shown in Figure 4.10 and Figure 4.11.

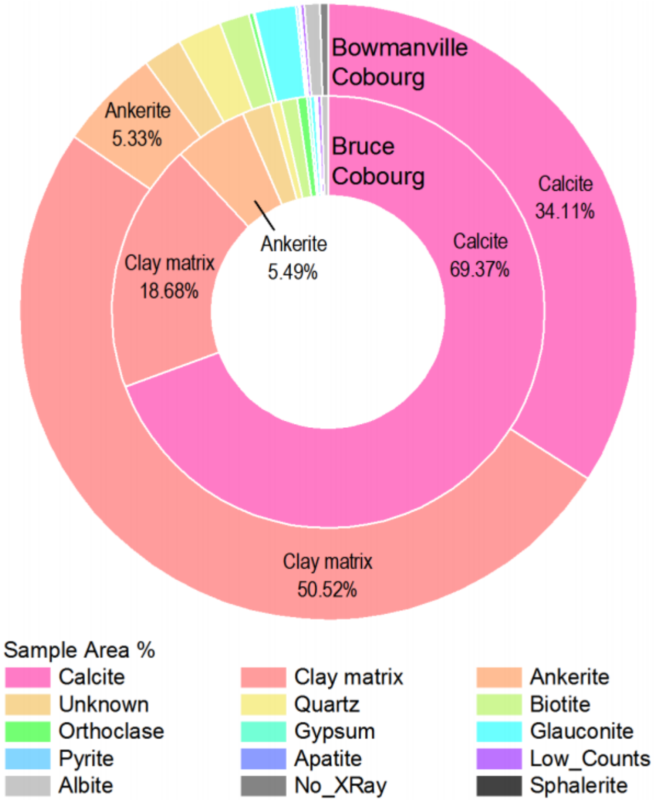

Figure 4.10. Modal mineralogy, thin section analyses results of Bowmanville and Bruce Cobourg limestones (Day, 2017)

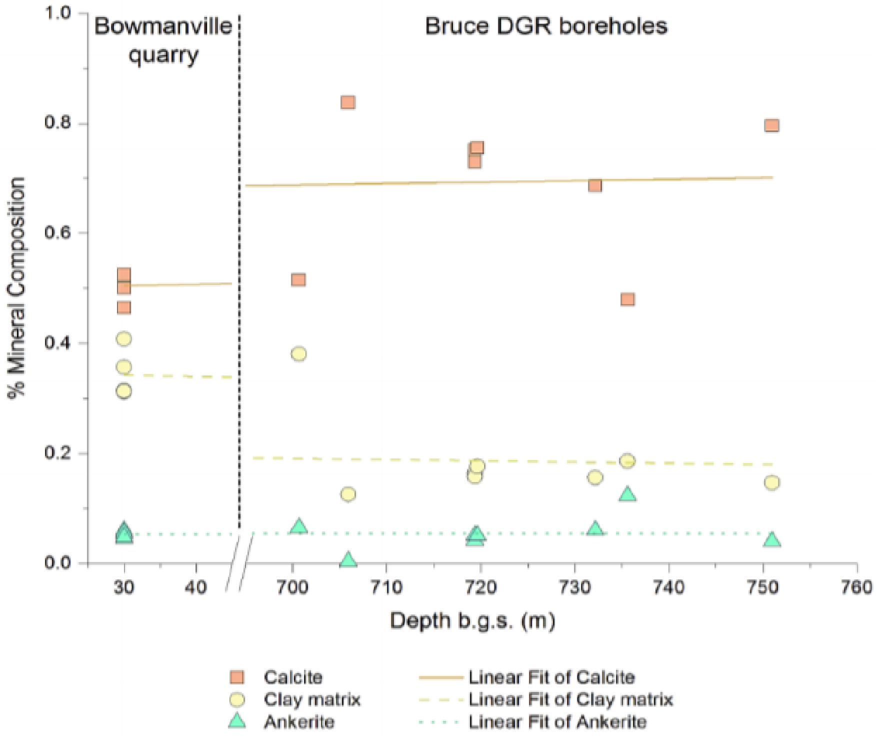

Figure 4.11. Comparison of the mineral composition of Cobourg limestones from Bowmanville quarry and DGR boreholes for different depths below ground surface (Day, 2016)

In general, the clay matrix takes up to 50% of the overall rock composition in the Bowmanville quarry, but reduces to only about 20% for the Bruce DGR boreholes, except at a depth of 700 m, which it is close to 40%. Jaczkowski (2017) noted that the relative consistency in the composition of the Bowmanville quarry is mostly due to the samples being taken at the same depth of 30 m. Should those samples have been taken for various depths as is the case for the DGR borehole, it is possible there would have been a wider spread in composition. That being said, Jaczkowski (2017) considers the rocks from the quarry to be a readily available analogous to those from the Bruce site. Laboratory UCS tests performed by Paraskevopoulou et al. (2017) on nine Cobourg limestones from the Bowmanville quarry showed an average UCS of 125 MPa. This is reasonably close to the average of 114.8 MPa obtained for the Bruce DGR limestone used in the image analysis. The image analysis procedure in this study however has a level of dependence on overall grain composition and so results for the limestone can only be loosely interpreted, compared to those for the granites obtained from SKB.

Each rock type from the SKB dataset included images of BTS (flat disc-shaped) and cylindrical UCS and triaxial samples, while the Cobourg limestones were all BTS samples. As noted earlier, flat surfaced samples are the most desirable for any photo-analysis operation. The choice of images to estimate the m_i on was therefore biased towards the BTS samples. Each rock types contains quartz, plagioclase feldspar, K-feldspar and biotite, with the major differences between the different rocks being the relative abundance of the constituent minerals. Estimates of grain size and kurtosis modifier parameters represent the overall grain distribution and does not account for the different minerals present in the rock. In the photo-analysis operations however, the different minerals were distinguished, but ultimately aggregated together for the parameter estimates This process is illustrated in Figure 4.12 (see Appendix A for full list of raw and processed images). Due to difficulties in precisely determining each parameter from the sample photographs, it was decided to make estimates of the ranges of values of each parameter, except for porosity, which has already been accurately measured in the laboratory. A high, average, and low estimate for each input value was determined and used to calculate the estimated mi value, as shown in Table 4.3.

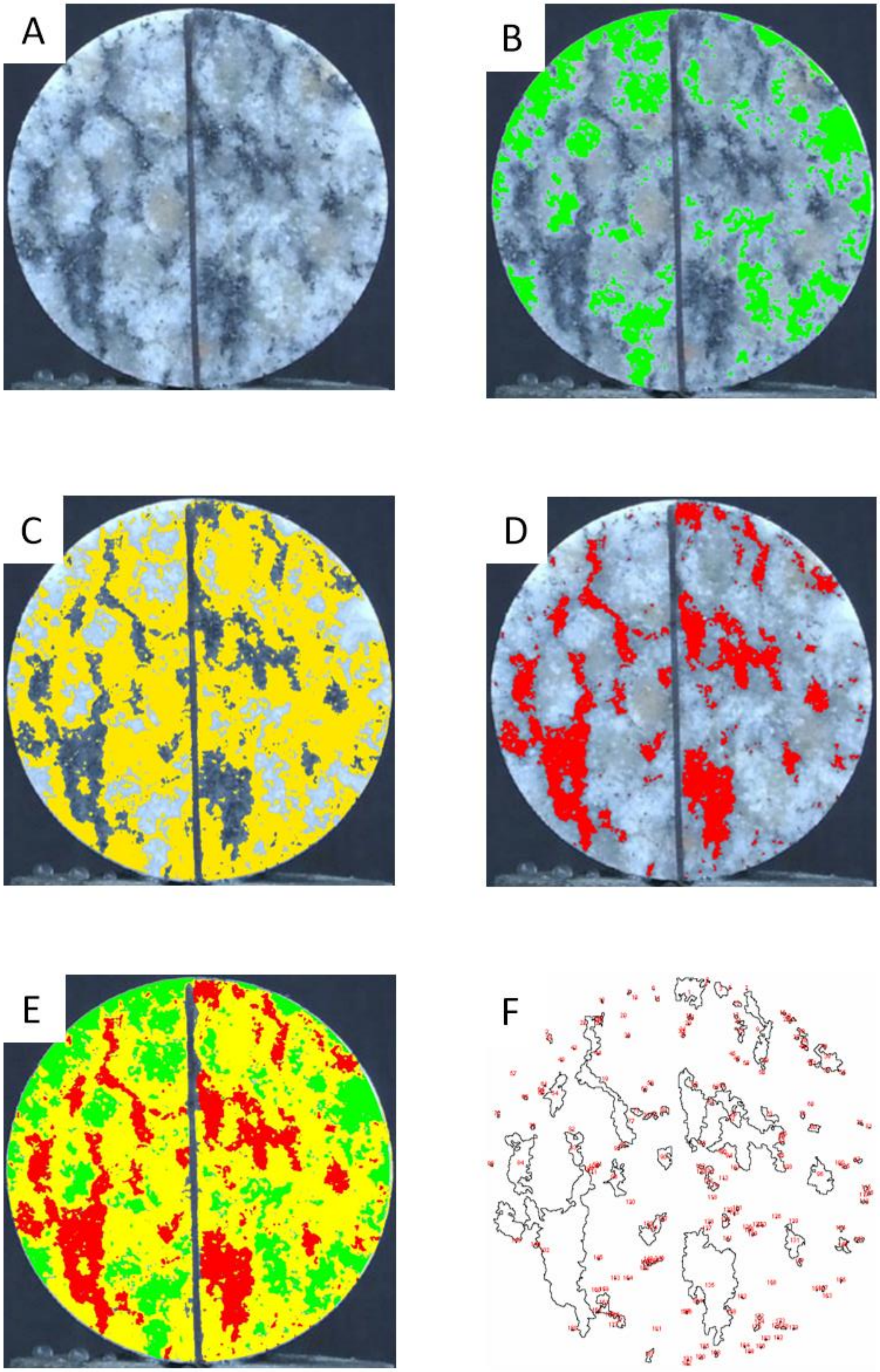

Figure 4.12. Images analysis procedure on medium grained granite showing various stages of the process: (A) Raw image, (B) Feldspars isolated, (C) Quartz isolated, (D) Biotite isolated, (E) Combined parts to show a complete picture of distinguished grains, (F) Isolated outline of grains with indications of grain count (Jacobsson, 2005)

Table 4.3. Range of visually determined inputs from a variety of SKB test reports (Jacobsson 2004, Jacobsson 2005, Jacobsson 2006). The values for "Lab m_i" are shown for the three groups of the laboratory datasets that were used in determining m_i as follows: ^{1}Triaxial data only; ^{2}Triaxial + UCS data; ^{3}Triaxial + UCS + Pseudo DTS data

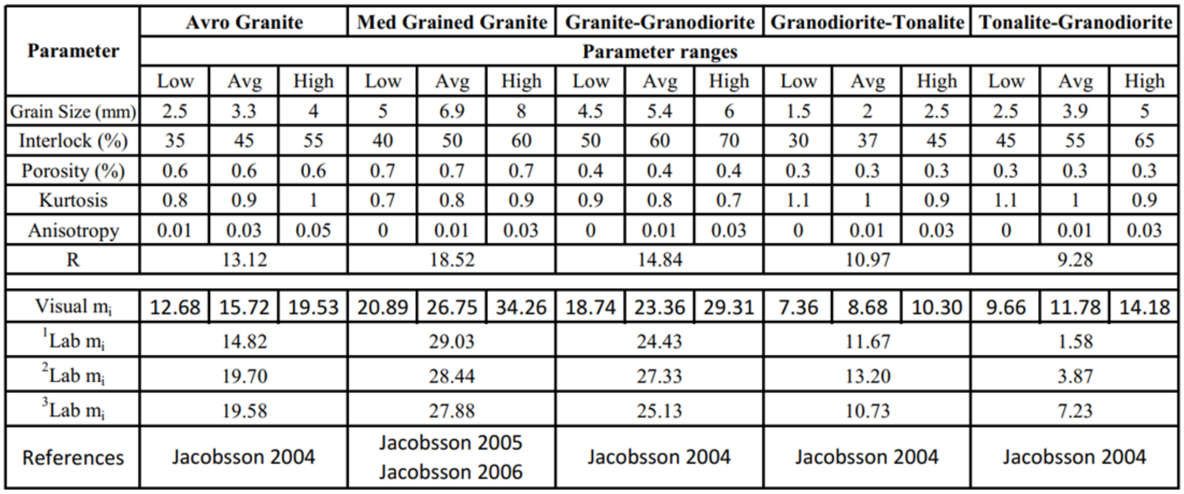

Parameter	Avro Granite			Med Grained Granite			Granite-Granodiorite			Granodiorite-Tonalite			Tonalite-Granodiorite		
	Parameter ranges														
	Low	Avg	High	Low	Avg	High	Low	Avg	High	Low	Avg	High	Low	Avg	High
Grain Size (mm)	2.5	3.3	4	5	6.9	8	4.5	5.4	6	1.5	2	2.5	2.5	3.9	5
Interlock (%)	35	45	55	40	50	60	50	60	70	30	37	45	45	55	65
Porosity (%)	0.6	0.6	0.6	0.7	0.7	0.7	0.4	0.4	0.4	0.3	0.3	0.3	0.3	0.3	0.3
Kurtosis	0.8	0.9	1	0.7	0.8	0.9	0.9	0.8	0.7	1.1	1	0.9	1.1	1	0.9
Anisotropy	0.01	0.03	0.05	0	0.01	0.03	0	0.01	0.03	0	0.01	0.03	0	0.01	0.03
R	13.12			18.52			14.84			10.97			9.28		
Visual m_i	12.68	15.72	19.53	20.89	26.75	34.26	18.74	23.36	29.31	7.36	8.68	10.30	9.66	11.78	14.18
^{1}Lab m_i	14.82			29.03			24.43			11.67			1.58		
^{2}Lab m_i	19.70			28.44			27.33			13.20			3.87		
^{3}Lab m_i	19.58			27.88			25.13			10.73			7.23		
References	Jacobsson 2004			Jacobsson 2005 Jacobsson 2006			Jacobsson 2004			Jacobsson 2004			Jacobsson 2004		

Figure 4.13 shows a comparison of visual m_i's for each rock type, compared with its corresponding laboratory-determined m_i. The bars above the dashed line show the results of those rocks for whose both pictures and laboratory test results were available. For the rock types below the dashed lines, only sample pictures were available. The Cobourg limestone included samples from two boreholes (DGR3 and DGR4). The samples from these boreholes were analyzed separately and also analyzed combined.

The three methods of determining the laboratory m_i produced values that were relatively close to each other, except for tonalite-granodiorite. Similarly, average visual estimates of m_i for each rock type, except tonalite-granodiorite and Cobourg limestone (DGR3), were within 80% of their corresponding laboratory determined m_i's. The discrepancy found in the results of tonalite-granodiorite can be partly attributed to a smaller number of datapoints for curve fitting (a total of 14 spread across the tensile, compressive and triaxial spectrum) and the presence of a datapoint outlier in the triaxial region which would affect the value obtained from the curve-fitting process. This also resulted in large variations among the three laboratory-estimated m_i values compared to the other rocks.

In general, Eqn 17 produced good estimates of m_i with an accuracy of up to 96% for the medium grained granite, but the parameter was overpredicted by more than 60% for tonalite-granodiorite. The accuracy visual m_i values in this case is calculated as the closeness to the laboratory-estimated m_i values, expressed as a percentage according to the expression below;

$$Accuracy = 100 - \left(\frac{|m_i(lab) - m_i(visual)|}{m_i(lab)} \; x \; 100\% \right) \tag{18}$$

There is a better match of visual and laboratory estimates for DGR4 than DGR3. As noted earlier, the sample pictures were not obtained directly from the DGR boreholes and so the idea of separating them into DGR 3 and 4 is only applicable to the laboratory test results. Analysis of the m_i equation shows that the m_i estimate is most sensitive to changes in kurtosis due to its exponential relationship with the Sheorey quotient, R, and also the assumed power constant of 0.8 based on curve fitting the most reliable tensile data points listed by Hoek and Brown (2018).

Additional data may help to shed better light on the accuracy of these fit parameters. Nevertheless, the digital imagery determinations clearly show that $k_{(G\emptyset)}$, alongside the modal grain size, d, are amongst the easiest of the Eqn. 17 input parameters to measure most accurately. Consistently defining these two image-determined parameters proves much easier when high resolution photos and digital photo analysis is employed, compared with interlock, ξ, which requires a more subjective interpretation of the angularity of the individual grains. It is therefore recommended that ξ should always be estimated as a range instead of a single deterministic value.

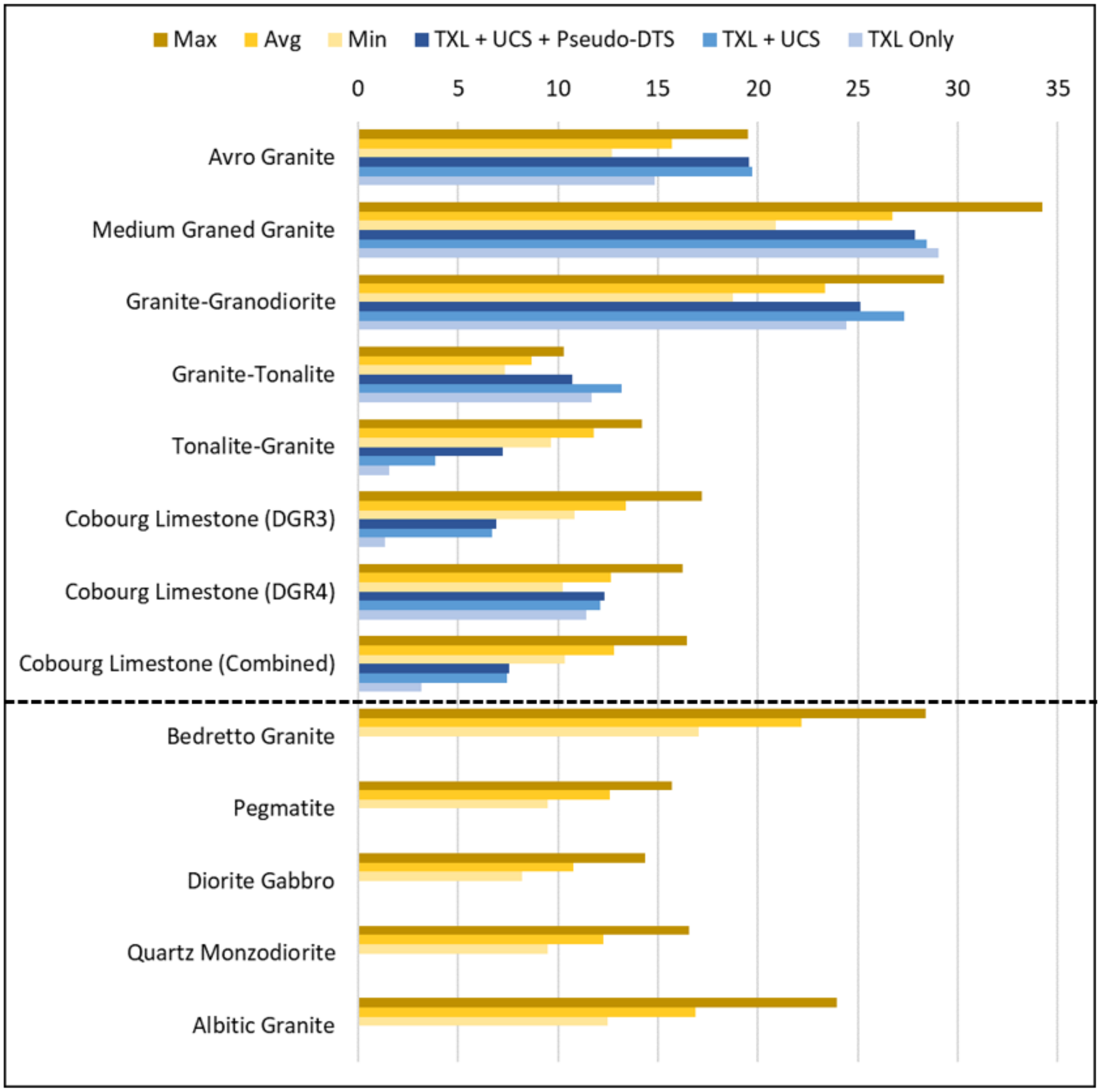

Figure 4.13 Comparison of visual estimates of Hoek-Brown mi with laboratory test results

The m_i equation however shows promise for providing a potential first estimate of the m_i value for a given rock type prior to rigorous test data availability, but will require high-resolution photo documentation of rock samples in order to be applied as a general technique. Further analysis of additional lab data that encompasses a larger sample size and a wider range of rock types is needed though in order to further assess reliability and limitations of this m_i estimation approach. The findings show the importance of m_i as a rock material parameter and the need to take extra steps to determine the value of the parameter as accurately as possible. Changes in the m_i parameter can influence the results of numerical models. This is demonstrated with a case study in the next chapter.

CHAPTER 5. BACK ANALYSIS TO DETERMINE THE STRESS STATE AROUND THE BEDRETTO ADIT, SWITZERLAND

This section further explores the influence of rock m_i on numerical models. A deep-seated tunnel was used as a case study by performing a numerical back-analysis procedure to estimate the potential stress field around it.

5.1 Design and Construction of the Bedretto Adit

The Bedretto adit is a 5.2 km long passageway to the Furka Base tunnel in the Swiss Alps. It was excavated to provide an access point to aid in the construction of the Furka Base tunnel, which connects Realp with Oberwald in Switzerland (Amberg, 1983). This was necessary due to the relatively long stretch of the Furka tunnel (15.4 km) and the difficult hydrogeological and geomechanical conditions which were encountered during construction (Amberg, 1983). Construction of the Furka tunnel was completed in 1982, ten years after the construction was initiated. As shown in Figure 5.1, the tunnel passes through several rock units including granites, gneiss and permocarboniferous series. The general trend of the rock units is NE-SW, which happens to be more or less parallel to the direct line joining Realp and Oberwald. A study by Keller and Shneider, (1982) indicated that fault zones are pervasive in the area, with the foliation mostly steep to vertical.

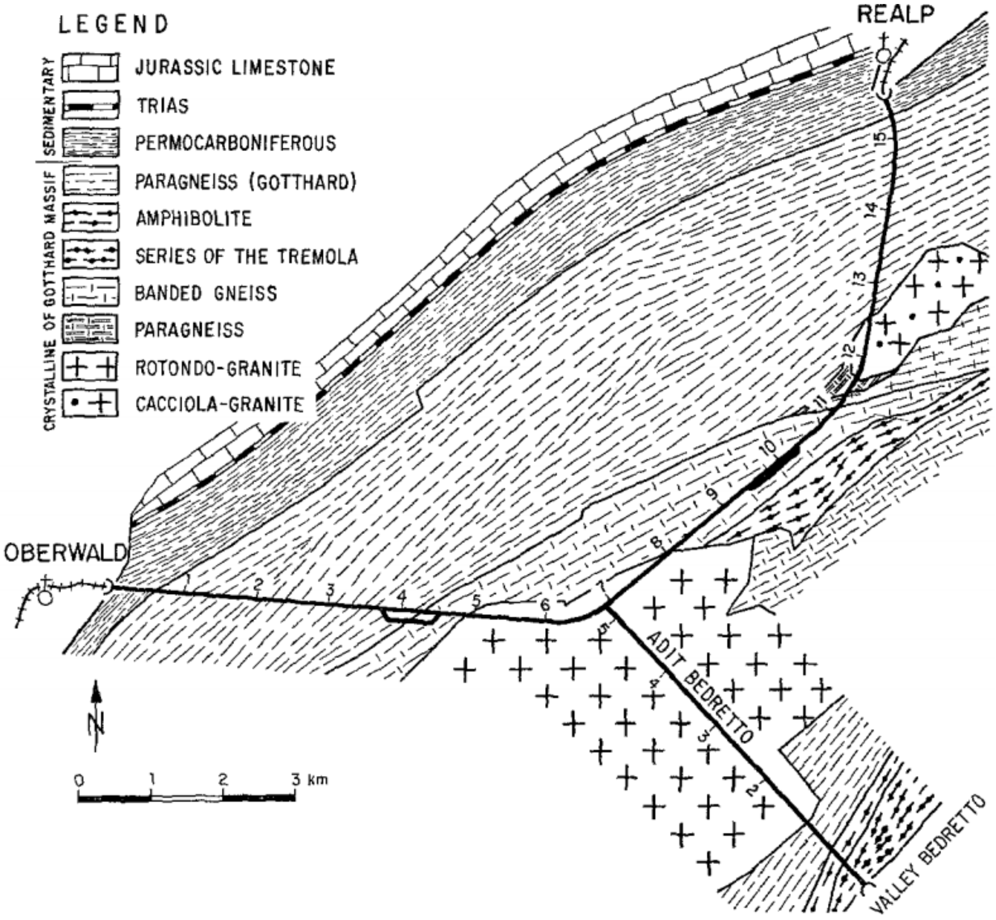

Figure 5.1 Geology of the central Swiss alps showing the routes of the Furka base tunnel and Bedretto adit (Amberg, 1983)

Due to the poor mechanical properties of phyllite in the permocarboniferous rock series in the region, coupled with the unfavorable trend of the rock layers with respect to the initial proposed alignment of the tunnel, it was later decided to adopt the route shown in Figure 5.1 (Amberg, 1983). The aim of this line was to ensure the tunnel passed through the stronger gneissic and granitic rock units as much as possible and reduce passage of the tunnel through the permocaboniferous series to only the two ends of the tunnel as well as change the orientation of the tunnel to a more favorable geomechanical orientation The curved route resulted in an additional 3.5 km length of tunnel compared to a straight line connecting the two towns. This necessitated the construction of the Bedretto adit close to the midpoint of the Furka tunnel to serve as an additional access point for construction to speed up the excavation.

In addition to its original role as an access point, the option was also open for the Bedretto adit to serve as a railway link between Realp, Oberwald and the southern regions, including the municipality of Ronco (Meier, 2017). The adit has a horseshoe cross section with a width of 2.8 m and an elliptical crown (Figure 5.2). The adit trends NW-SE and its cross section is uniform throughout its 5.2 km span, except for a few places where the passageway was widened to accommodate double train passage. During construction, the adit was supported with mesh and bolts in areas with excessive overbreak and with timber and steel liners in fault zones. However much of the rest of the adit is unlined. As indicated in Figure 5.3, the adit lies mostly in the Rotondo granite, with overburden depths that range from close to zero to just over 1500 m.

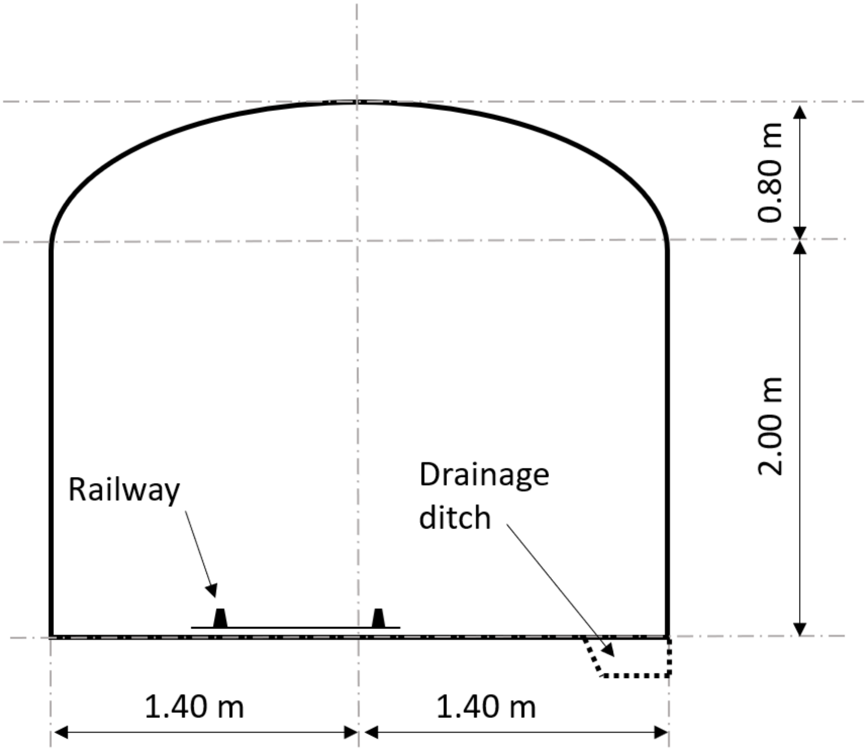

Figure 5.2 Design cross section of the Bedretto adit (modified from Huber, 2004)

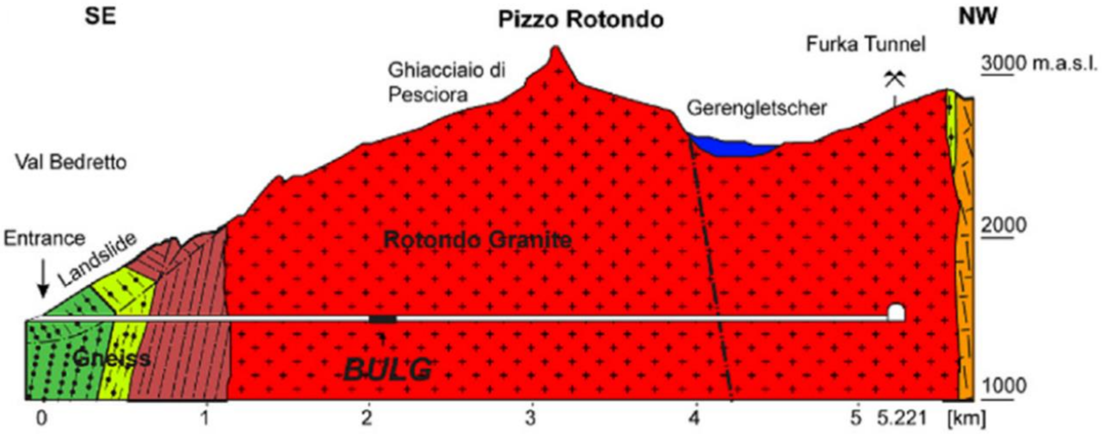

Figure 5.3 A simplified geological cross-section of the Bedretto adit (Gischig et al., 2020)

The Bedretto adit was abandoned after the completion of the Furka Base tunnel, leaving many areas unsupported. This provided a rare opportunity to directly observe the behavior of an unlined tunnel under high stress that has been open for 37 years. Brittle failure of the walls of the adit were observed during construction of both the tunnel and its adit and to this day, spalling slabs continue to fall from the exposed adit walls (personal observations by co-authors).

5.2 Geology of the Leventina District

The Bedretto adit is located in the Italian-speaking canton of Leventina. The locality is characterized by alpine mountain ranges consisting of mostly granitic and gneissic rocks with the peak occurring at the Pizzo Rotondo at an elevation of 3192 m a.s.l. Among the geological units in the region, the most relevant to the study is the Gotthard massif. The tunnel lies mostly in the Rotondo granite, whose name was derived from the Pizzo Rotondo (Figure 5.4).

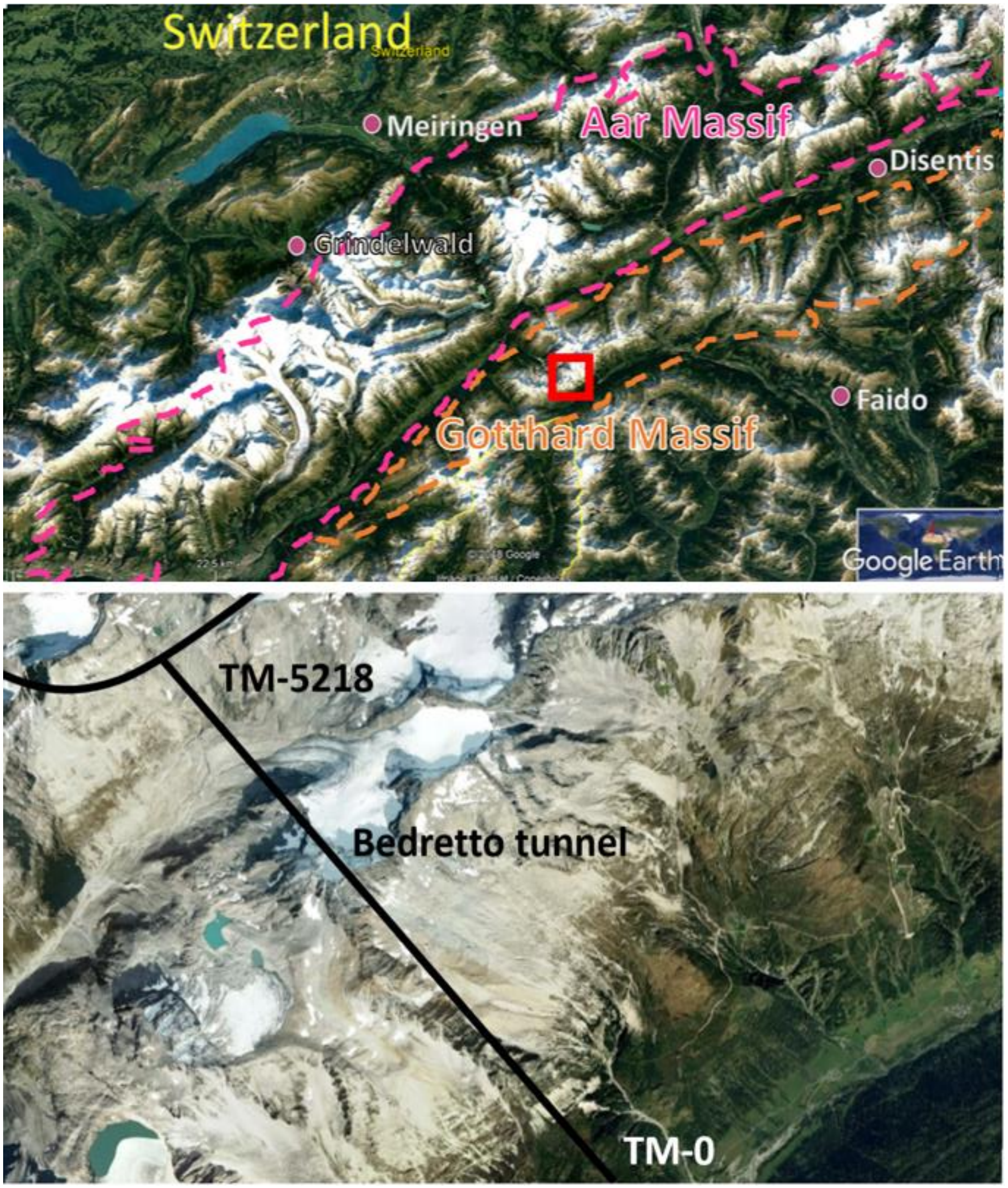

Figure 5.4. Geology of Leventina district showing the boundaries of the Aar and Gotthard Massifs and the location of the Bedretto adit (red square), with the lower image showing the Bedretto tunnel (adit) alignment and connection to the Furka base tunnel at TM-5218

The granite is one of the many granitic plutons present in the Gotthard massif (Lutzenkirchen 2002). The Gotthard massif consists of pre-Variscan gneisses and granitoids of the Ordovician period. The gneisses are sometimes referred to as striped gneiss due to a characteristic lineation of foliation planes on the rocks which is thought to have occurred during a late Caledonian phase of overprinting (Heim 1981, from Lutzenkirchen 2002)). The Gotthard massif lies adjacent to the geologically similar Aar massif, although the two are separated by a thin zone of metasediments consisting mostly of schists, dolomites and carbonates (Lutzenchirchen, 2002). The Rotondo granite consists of biotite, characterized by schistosity and elongated grains of quartz and feldspar (Huber, 2004). Along the adit, the granitic body is intruded by sub-vertical aplite and lamprophyre dykes and usually associated with fault zones. The elongation in the Rotondo granite is aligned perpendicular to the adit axis. This alignment coincides with the general alignment of the fault structures as discussed in the next chapter. Foliation in the granite is subtle, nearly invisible to the naked eye, and will require detailed mineralogical examination to properly characterize. Using the point counting method on thin sections, Huber (2004) estimated the relative abundance of the constituent minerals in the granite across TM 4672 to 5117. In total, six major groups of minerals were identified as shown in Figure 5.5 .

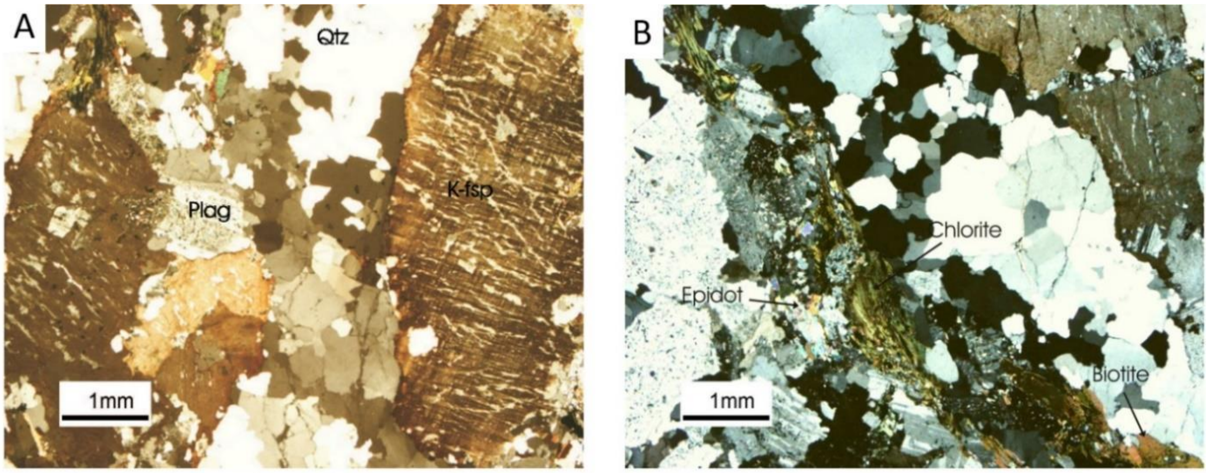

Figure 5.5. Thin sections of granite rock specimens from adit showing the various minerals. Sample A) was taken from intact rock while B) was obtained from a fracture zone (from Huber, 2004)

5.3 Geotechnical and Structural characteristics of the Bedretto Adit

5.3.1 Fault Structures

Field measurements indicate that the adit passes through a major fault zone that strikes perpendicular to the adit. The granitic rock is also a host to joints of various degrees. The Bedretto adit provides a very good scanline for surface fracture mapping due to its perpendicular relationship with the fault zones. Scanline surveys on surface outcrops and along the adit profile performed by Priest (1993) indicated that there are at least four joint sets associated with the major faults (summarized in Table 5.1). The mean spacing of surface fractures along the scan line was estimated to be 31.8 m, although it varies from a low of 15 m in the northern section to a high of 84 m in the southern section of the adit (Lützenkirchen & Loew, 2011) It should be noted that all the observed joints sets are almost vertical, making it easier to infer the location of the joints in the adit based on ground surface observations. Ofterdinger (2004) noted that joint sets 1 and 2 were much more abundant on the terrain surface, while joints 3 and 4 were mostly only observed with the tunnel. This could imply that joint sets 3 and 4 were more influenced by the construction of the adit. In mountainous regions such as the Swiss Alps, fault zones on the terrain surface can be identified from a geological feature known as fault scarps, which are linear offsets on the ground surface created due to relative movement of the two sides of a fault zone. Some authors consider joint sets 1 and 2 to be minor fault zones. Lutzenkirchen (2011) noted that in most of the fractures, a damage zone could be identified around the core, where most deformation occurs. A fault zone is defined by a tabular region containing many parallel faults. By this definition, joint sets 1 and 2 can be considered to be fault zones. The sets were also characterized by brecciation and geochemical alteration.

Table 5.1 Attitudes of joint sets in the Bedretto adit (Ofterdinger, 2004)

Set Number	Mean Orientation (Strike/Dip)	$\lambda_{surface}$ (m^{-1})	λ_{adit} (m^{-1})
1	049/75 SE	2.1	0.5
2	080/83 SE	1.5	0.2
3	140/86 SW	0.7	2.6
4	170/79 SW	0.04	0.3

λ = Mean facture frequency

The joint sets are mostly concentrated at the northern section of the adit (i.e., between Tm 4000 – 5218) (see Figure 5.6). These joint sets strike predominantly in the SW-NE to WSW-ENE. Within the Bedretto adit, more than half of the minor brittle fault zones are associated by ductile structures such as cataclasites and fault gouge material. The individual faults and joints have relatively low apertures, mostly below 10 cm. A study of the occurrence of fault zone in the Gotthard Massif by Lutzenkirchen (2002) showed that the vast majority of faults in the region trend approximately NE-SW to ENE-WSW, similar to the surface faults mapped above the Bedretto adit (Davies, 2019). This provides a strong argument that the existing faults are regional faults. Therefore, other faults mapped within the adit which trend in a different direction are more likely to have be during construction of the adit.

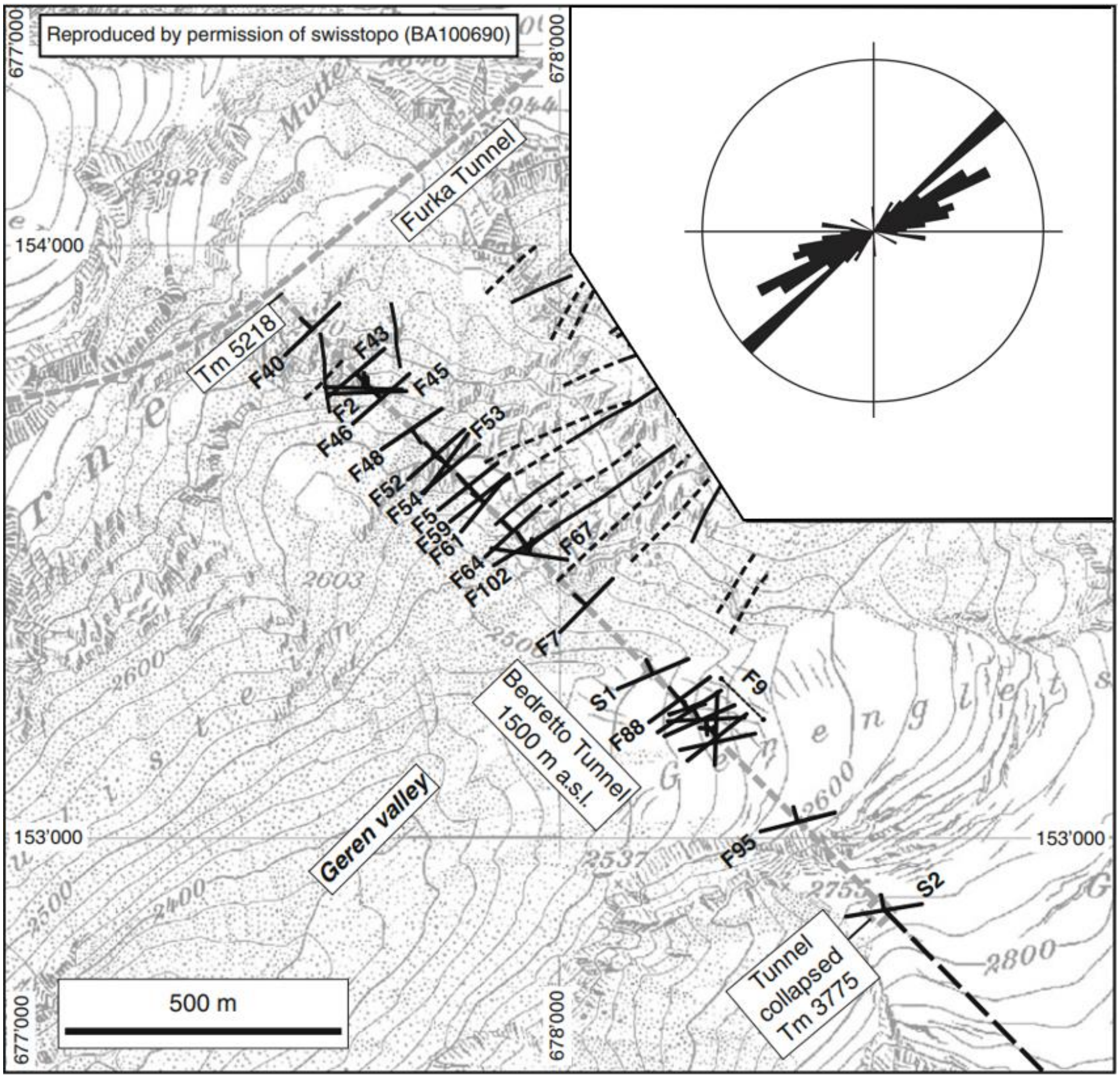

Figure 5.6: Surface faults mapped on the surface above the Bedretto adit (Schneider, 1985)

5.3.2 Water Flow

During the construction of the Bedretto adit, large quantities of water was encountered. This was however anticipated due to the presence of fracture networks in the Rotondo granite and as such methods for supporting the rocks and dealing with the groundwater were established to maintain the speed of construction (Amberg, 1983). At the time of construction, water inflow up to 100 l/s were measured for short periods.

Groundwater monitoring of the alpine region by Ofterdinger (2004) which included hydrochemical sampling and measurements of water inflow in the Bedretto adit showed that water seepage into the adit was partly influenced by the NE-SW orientation of the fractures. Figure 5.7 shows a record of measured water inflow rates at two sampling locations over a period of one year (July 1999 to July 2000). Discharge rates at individual sampling locations range from 0.56 l/min to 33.8 l/min, which is a significant drop from the rates measured during construction of the adit. The estimated hydraulic conductivity of the rock mass within the vicinity of the major fault zone is up to 10 times higher than in other locations of the adit (Table 5.2).

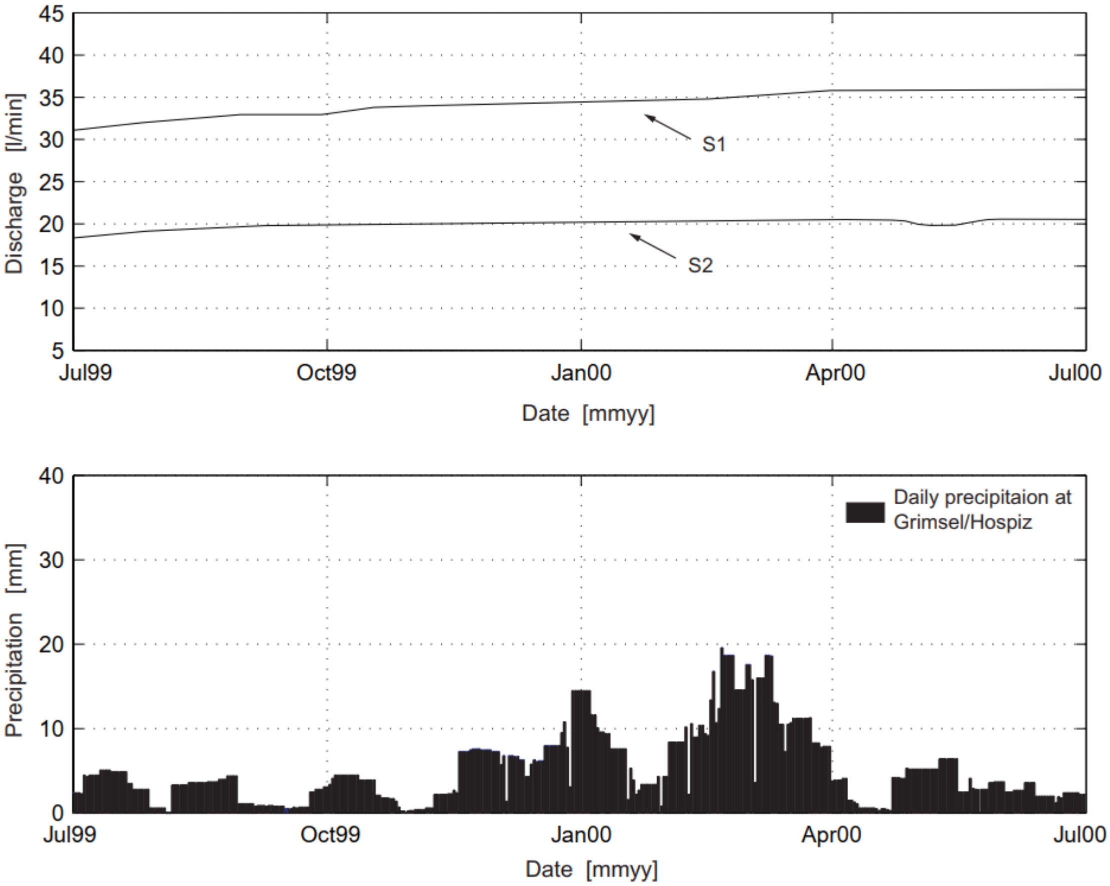

Figure 5.7. Daily record of water discharge measurements at two sampling locations in the adit (S1 and S2) and corresponding daily precipitation (Ofterdinger, 2004)

At most sampling stations, only small day to day variations of inflow rates were recorded. Despite the seasonal variations in precipitation, there were no corresponding changes to the discharge rates. There is however a noticeable trend of consistently increasing discharge rates throughout the year.

The increasing trend was speculated to be a response to long term annual increase in precipitation in the region. Records show that prior to the measurements, there had been approximately 50% year over year increases in annual precipitation in the Grimsel area for the previous four consecutive years. Hydrochemically, the water is slightly alkaline (pH from 8.9 to 9.3) and contains ions including Na^+, Ca^{2+}, HCO_3^- and SO_4^{2-}. Weathering results in the release of sodium from the granite rocks which contains up to 35% albite, resulting in an increase in alkalinity.

Table 5.2. Calculated Ranges of Hydraulic Conductivities of the Bedretto Adit (Ofterdinger et al, 2014)

Section of Bedretto Adit	Range of Hydraulic Conductivities (m/s)
Fault Zone	$6.0 – 8.2 \times 10^{-8}$
Remaining Adit Sections	$6.0 – 8.3 \times 10^{-9}$
Overall	$1.0 – 1.4 \times 10^{-8}$

Numerical models by Ofterdinger et al. (2014) indicated that the Geren glacier that sits on the ground surface above the adit contributes to flow through the fault zones and their preferred orientations result in an anisotropic flow through the Rotondo granite. The fault zones themselves do not significantly influence the regional groundwater table. Water inflows to the adit flow southwards towards the Ronco portal and most of the inflows into the Furka base tunnel flow westward towards the Oberwald portal (Figure 5.8).

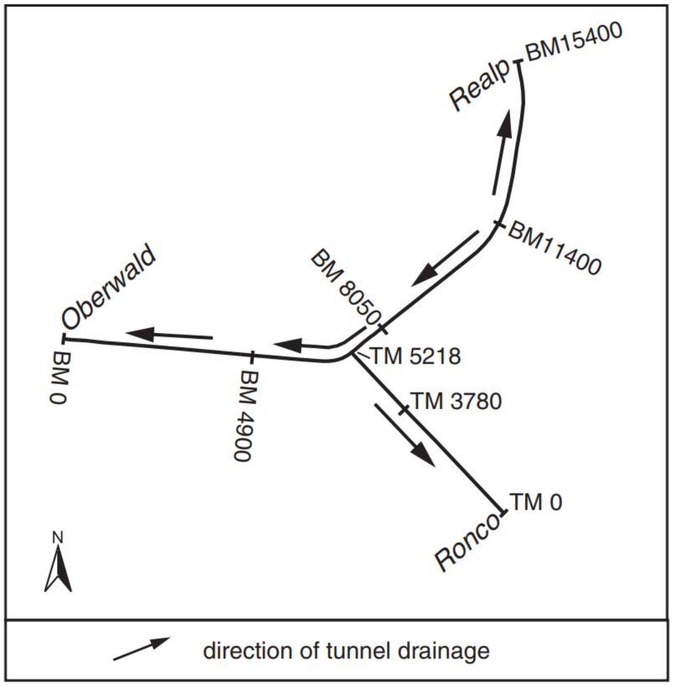

Figure 5.8. Trace of drainage in the Furka tunnel and Bedretto adit (Ofterdinger et al., 2014)

5.4 Stress State Calibration Steps

The aim of this study was to use a numerical back analysis procedure using RS2 by Rocscience to determine the stress state of the rock mass within the vicinity of the Bedretto adit. The Bedretto adit is a good candidate for a numerical analysis because of the abundance of unlined walls with spalling rocks, which allows for the extent of rock damage to be directly determined and be used as a inputs for numerical back analysis when little rock test data is available. The study involved a calibration process whose major objective was to determine the magnitude and direction of tectonic stresses prevalent in the mountainous region. Prior to the calibration process, a scanned section of a 2 km length of the adit was produced with Light Detection and Ranging (LiDAR) equipment by Alcaíno-Olivares, (2017). This enabled a precise measurement of the damage geometry by comparing it to the original design of the horseshoe-shaped adit. For each scan section, five planar cross-sectional damage models were produced at 2 m intervals and the accumulated damage since construction of the adit was determined (Figure 5.9). Each scan section represents roughly 12 meters of the adit (see appendix B for full data on scans). In this paper, specific locations within the Bedretto adit are represented using the common Tunnel Meter (Tm) notation. The southernmost point of the adit is Tm 0000 and the northern part Tm 5200 where the adit connects to the Furka base tunnel.

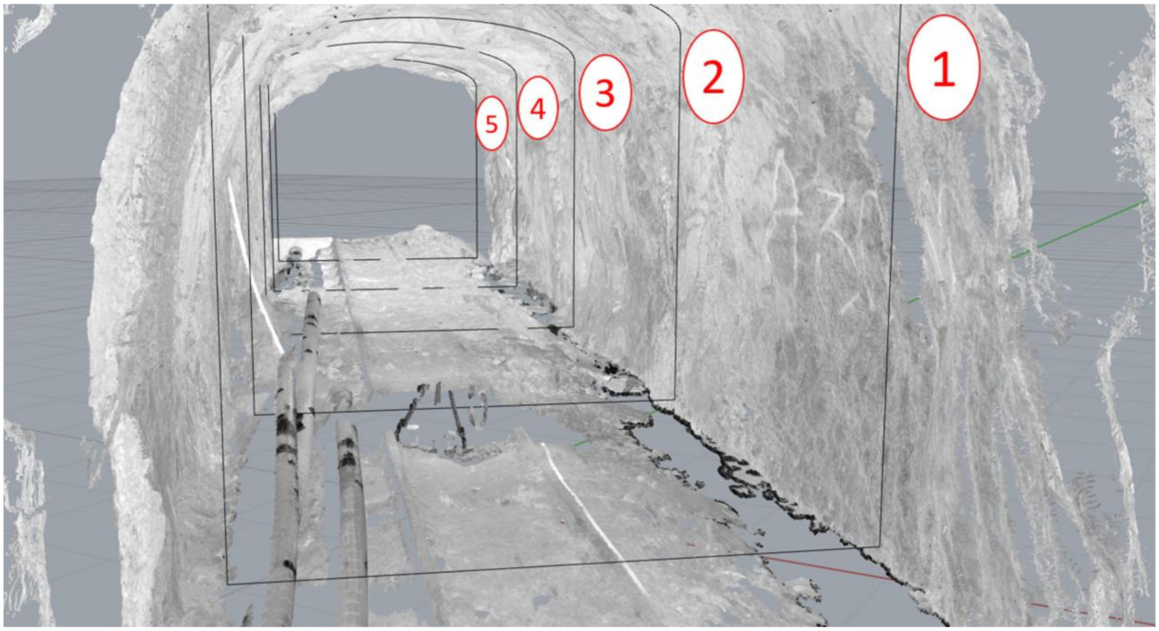

Figure 5.9.Processed point cloud data at TM 5104 with illustrated locations for cross sections

5.5 Constitutive Model and Failure Criteria

The Hoek-Brown failure criterion (Hoek et al. 2002) is one of the most widely implemented failure criterion for modelling rock mass behavior. Some authors have made the argument that friction only plays a role in the failure process away from the excavation boundary (Martin and Chandler, 1994; Hajiabdolmajid et al., 2002; Diederichs, 2007). In the vicinity of the excavation wall, extensile cracking processes dominate due to the free surface. This is based on the fact that friction plays a very limited role in a lab scale sample during unconfined compression loading near the crack initiation threshold, and only starts getting mobilized after a significant loss in cohesive strength. This was demonstrated by Martin and Chandler (1994) through damage testing of samples of Lac du Bonnet granite obtained from Canada's underground research laboratory in Manitoba.

Diederichs (2007) proposed a composite failure envelope composed of distinct "damage initiation" and "spalling limit" envelopes, aggregated as the Damage Initiation, Spalling Limit (DISL) method. While the DISL method does not directly utilize friction and cohesion parameters of a rock material, the Hoek-Brown parameters are selected such that the equivalent Mohr-Coulomb parameters conceptually represent a post yield cohesion reduction and friction mobilization, similar to the approach of Hajiabdolmajid et al. (2002) and Walton (2019). The damage initiation threshold is defined by Perras and Diederichs (2016) pointed out that this approach yields strain weakening behavior close to the tunnel surface (low confinement) and strain hardening behavior away from the surface (high confinement). For the damage initiation curve, the Hoek-Brown *a* parameter is set to 0.25, and *m* and *s* are calculated from the equations below;

$$s = \left(\frac{CI}{UCS}\right)^{\frac{1}{a}} \tag{19}$$

$$m = s\left(\frac{UCS}{|T|}\right) \tag{20}$$

Where *UCS* is the uniaxial compressive strength and T is the tensile strength

The spalling limit curve has parameters of a = 0.75, s = 0.001 and *m* ranges from 6 to 12, as reported by Perras and Diederichs (2016). The composite DISL curves are shown in Figure 5.10. The DISL model was implemented in RS2 and used in the calibration process. Material properties used for model input (Table 5.3) were compiled from previous field tests and measurements in the Bedretto adit by Huber (2004) and Keller and Schneider (1982). The uniaxial compressive strength was derived from the point load strength indices with a conversion factor of 18.7 by Huber (2004). The resulting intact, damage initiation and spalling limit curves used in the models are shown in Figure 5.10. Sensitivity analysis was performed to determine the optimum mesh size, which can be a limiting factor to the resolution of the model results.

Table 5.3 Material properties for intact granite rock where the adit lies (from Huber 2004; Keller and Schneider 1982)

Parameter	**Value**
Density (kg/m^3)	2650
Uniaxial Compressive Strength (MPa)	165
Tensile Strength (MPa)	5
Young's Modulus (GPa)	20
Poisson's ratio	0.25

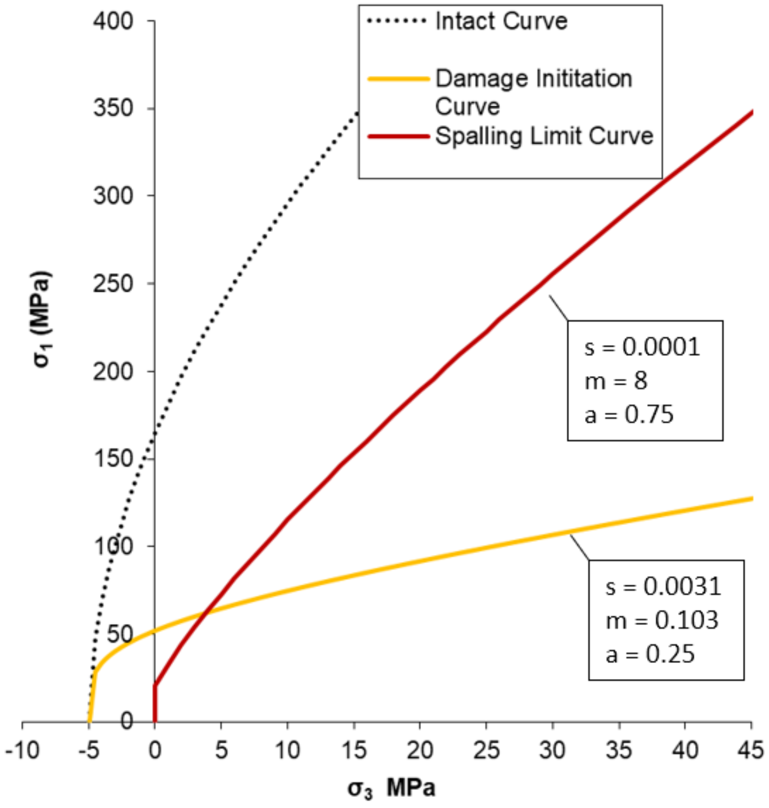

Figure 5.10. Hoek-Brown envelopes for the Bedretto adit showing intact failure envelope and DISL limit curves based on Diederichs' (2007) recommendations

5.6 Calibration Parameters

The first step in the modelling process was to generate a gravitational model to establish the base stress regime based on the overburden above the adit. As was expected, this was not sufficient to successfully predict the damage geometry due to the prevalence of tectonic stresses within the Swiss Alps. The tectonic stress was then applied as a variable input parameter described by the tectonic compressive stress, angular deviation and tilt, to be calibrated against the observed damage geometry, with ranges summarized in Table 5.4 and illustrated in Figure 5.11.

The models were calibrated by successively varying each of the variable parameters within the specified range and comparing the modelled damage geometry with field measurements. The ranges of σ_{tect} and φ were constrained based on results of *in situ* stress measurements reported by Ziegler et al. (2014) from different borehole techniques in the Grimsel area (14 km away from the Bedretto adit) to estimate the regional near-surface stress magnitudes and orientations. Their results indicated that the difference between σ_h and σ_H ranged from 7 MPa near the ground surface to 10 MPa at a depth of 680 m, where σ_h and σ_H are the minimum and maximum horizontal stresses, respectively. Their best estimate of the mean regional tectonic stress orientation was determined to be WNW-ESE. Hence it was decided that the angular deviation, φ will remain within N-S to W-E (anticlockwise) in the calibration process.

Table 5.4 Summary of calibration variables which control the magnitudes and orientation of applied tectonic stress

Applied Tectonic Stress Variable	**Range**
Tectonic Stress magnitude (σ_{tect})	0 to 35 (MPa)
Angular deviation from tunnel axis (φ) in the horizontal plane	0 to 45 (°) anticlockwise
Tilt from horizontal plane (ϴ), with positive upwards	0 to 20 (°) anticlockwise

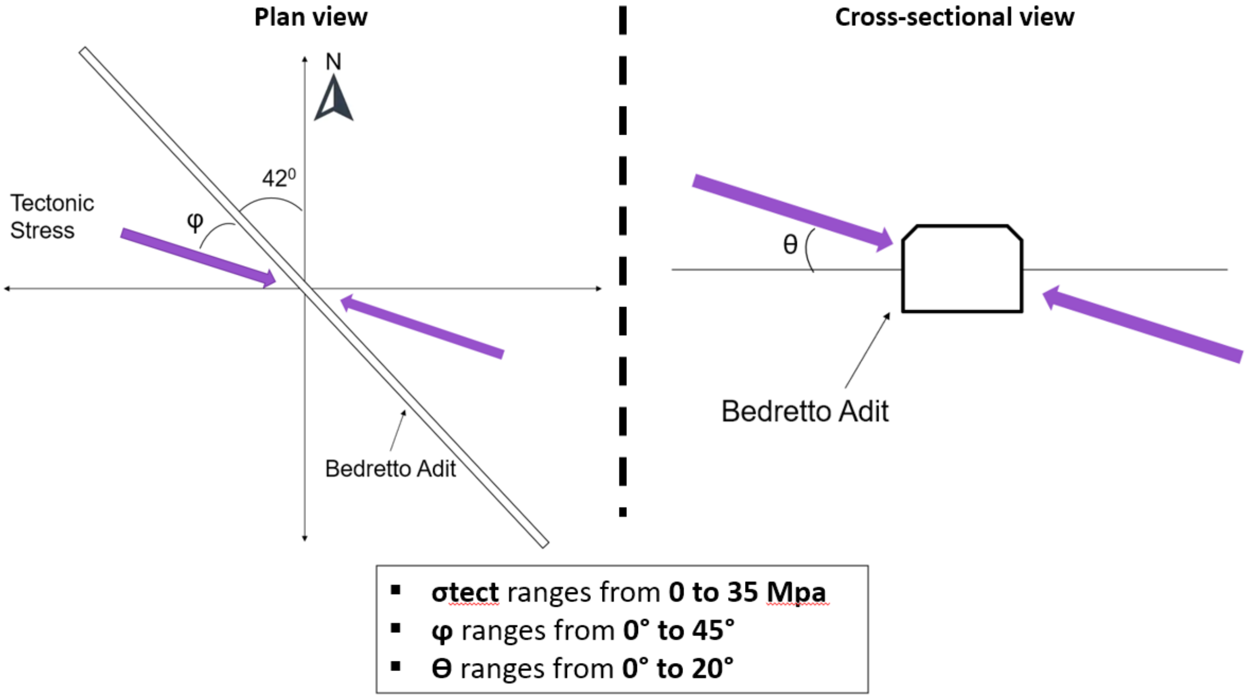

- **σtect** ranges from **0 to 35 Mpa**
- **φ** ranges from **0° to 45°**
- **ϴ** ranges from **0° to 20°**

Figure 5.11. Schematic illustration of the three calibration parameters used in the calibration process

5.7 Results

5.7.1 Measured Damage Geometry

The adit was mostly unsupported except for areas with major damage, where the walls have been supported with mesh and bolt or steel arches. A lot of steel sets have been installed between Tm 4200 and Tm 4600, which is very close to a major fault (between Tm 4125 and Tm 4275), recognized and studied by Lutzenkirchen (2002). Away from the fault zone, individual joints can still be observed in certain places along the walls of the adit. Assessment of water inflow into the adit by Lutzenkirchen (2002) indicated that the flow rate is heavily dependent on the density of joints and their interconnectedness to the major faults in the region, which implies that the flow rate is higher closer to the major fault zone (see Figure 5.12(A)).

Studies have been undertaken in the adit by Huber (2004), who focused on the structural and geological conditions of the adit, as applied to spalling between Tm 4600 and Tm 5200, and Alcaíno-Olivares (2017), who extended Huber's (2004) work to wider scan sections (12 m in length) using LiDAR. This present study expanded the investigations of the previous authors by further examining the LiDAR data collected by Alcaino-Olivares (2017) in more detail and taking a more statistical approach, which enabled a numerical calibration of the local stress field to be performed. Analysis of the LiDAR scans in the present study indicated that the extent of overbreak in the adit only weakly correlates to the depth of overburden.

The extent of overbreak was almost consistently higher on the western wall than that of the eastern wall of the adit. This observation was hypothesized to be due to a combination of the effects of structural influences and a far field stress regime in which σ_1 and σ_3 slightly deviated from the vertical and horizontal planes, respectively. The overall average overbreak depth on the western wall over the 2 km length of scanned sections is 0.49 m (standard deviation of 0.16 m), compared to the eastern wall with an average overbreak depth of 0.38 m (standard deviation of 0.13 m). The ranges of observed depths of damage in Figure 5.12(B) highlights the variability of damage that can occur at two points within a few meters of each other.

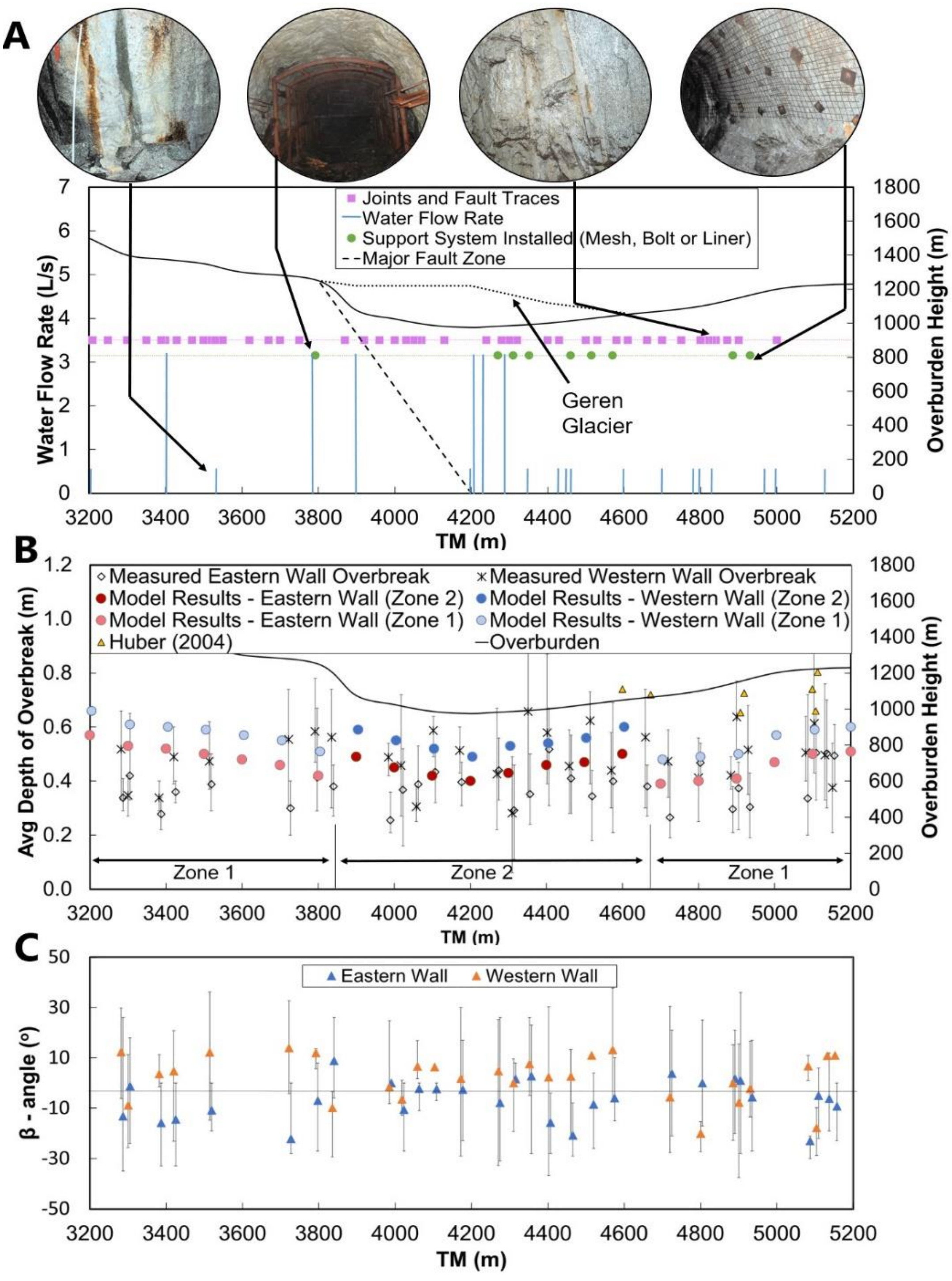

Figure 5.12. (a) Structural observations in the tunnel including compiled data from Lutzenkirchen (2002) and observations from LiDAR scans. (b) Comparison of numerical results with measured depths of overbreak, showing the two damage zones. The error bars are associated with the measured results and represent the range of values within the same scan section, collected by Alcaino-Olivares (2017). Data points, modified by Alcaino-Olivares (2017), from Huber (2004) are single cross-sectional profiles, taken at locations with the highest observed depth of overbreak. (c) Variation of measured β-angles along the adit

Within the 2 km length of LiDAR scanned sections, certain parts of the adit are subjected to increased structural influences which may affect the depth of overbreak. Specifically, the region between Tm 3900 and Tm 4700 is in close proximity to the major fault, has high water inflow rateS through the joints, is beneath a glacier, which influences the effective depth of overburden (see Figure 5.3), and is more frequently supported with steel sets. For this reason, this region (herein referred to as “Zone 2”) was treated separately from the other scanned sections (Zone 1) for the purpose of calibrating the models. These zones are based on previous work in the adit by Alcaíno-Olivares (2017) who divided the adit section into three zones for similar reasons. In this present study, two of Alcaíno-Olivares’ (2017) zones were combined into one for the purpose of calibrating the models.

5.7.2 Numerical Calibration

The model results were interpreted based on an assessment of the simulated excavation damage zones, as described by Perras and Diederichs (2016). The transition between the outer excavation damage zone and inner excavation damage zone was interpreted to represent the outer limit of spalling in the model. The transition can be visually interpreted as an isoline of the volumetric strain reversal point within the plastic yield region of the model.

An illustration of a scanned cross-section and a corresponding model result is shown in Figure 5.13. The full results across the 2 km span is shown in Figure 5.12(a). Despite the lower overburden height above Zone 2, the measured overbreak depth was slightly higher than that of Zone 1. Zone 2 was calibrated first, after which the *in situ* stresses were adjusted to account for the structural influences. This was necessary because it was discovered that it was not possible to calibrate one single numerical model to satisfactorily predict the depth of overbreak across the entire 2 km span.

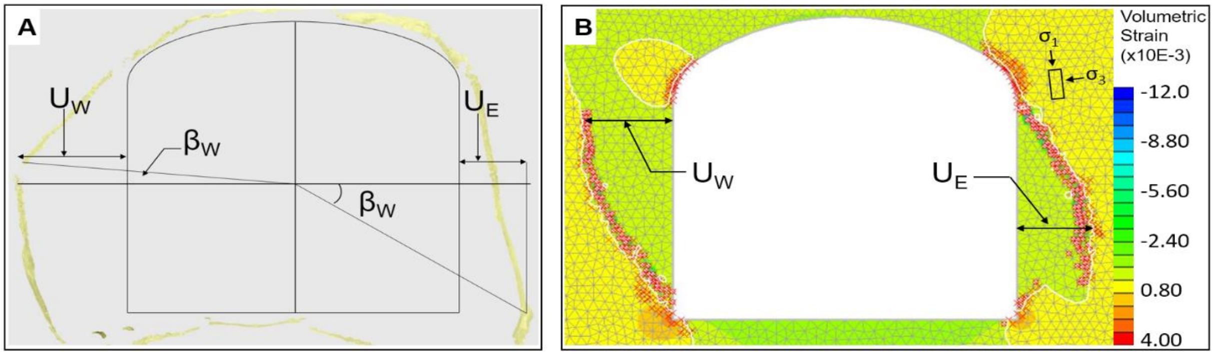

Figure 5.13. Cross sections showing measured parameters from (a) the LiDAR scan cross section and (b) model results, both at Tm 5100. The size of the mesh at the excavation boundary was 0.05m. β-angles below the horizontal centreline are negative

By considering different *in situ* stress scenarios, it was determined that the complex structural differences between Zone 2 and Zone 1, including the glacier on the ground surface is numerically equivalent to an additional surcharge of approximately 3.25 MPa in σ_1 within zone 2. At any given adit location, it was possible to numerically obtain the same depth of damage and β-angle for a few different combinations of the three calibration parameters (σ_{tect}, φ and Θ). However, for all but one of the combinations, the depth of overbreak was either significantly overpredicted or underpredicted at a different adit location within the same zone. The one particular combination which satisfactorily predicted the damage geometry across most of the 2 km length investigated (i.e., σ_{tect} = 20 MPa, φ = 30° and Θ = 15°) was taken as the closest numerical representation of the local tectonic stress conditions around the adit. This translated to a tectonic stress orientation of N108E (approximately WNW-ESE), dipping 15° to the horizontal plane. This orientation is consistent with data contained in the world stress map (Heidbach et al. 2016) and recent stress characterization work performed in the Bedretto underground laboratory by Ma et al., (2019).

5.7.3 Sensitivity of Model to Calibration Parameters

In the calibration process, the shapes of the resulting modelled damage zones were most sensitive to Θ. This variable affects the symmetry of the damage zone. At $\Theta = 0^{\circ}$, simulated damage around the adit is always identical on both sides of the wall, β-angle = 0° on each sidewall and there is no difference between the depths of overbreak on either wall of the adit (U_W and U_E). U_W is more sensitive than U_E to changes in Θ such that at non-zero values of Θ, the difference between U_W and U_E is also non-zero, as illustrated in Figure 5.14(b). However, at $\Theta > 20^0$ damage occurs on the roof of the adit – a situation which was not physically observed in the adit.

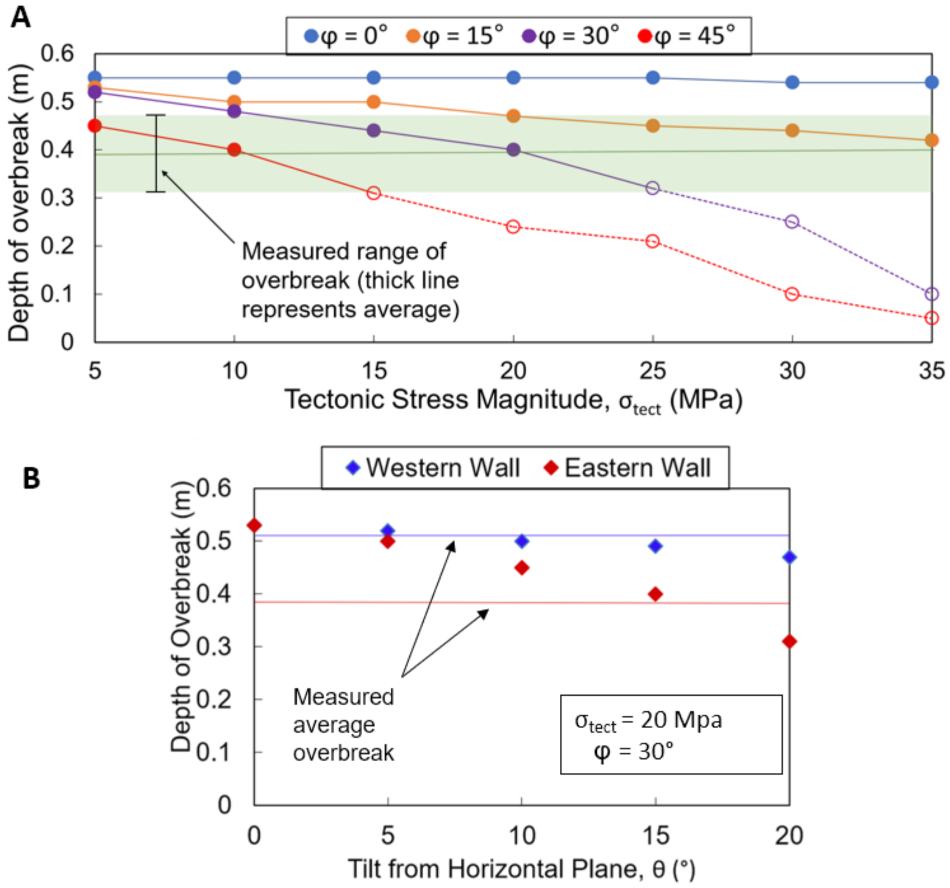

Figure 5.14. Sensitivity of model to changes in (a) σ_{tect} and ϕ, at Tm 4200 and (b) ϑ at Tm 4200. Tm 4200 was the starting point in the calibration process. For simplicity, only the results for the eastern wall are shown in (a). Points within the green zone represent the best model predictions. Hollow circles represent model results with damage concentrated only at corners of adit, which is a limiting factor in considering the final stress state. This process was repeated for other adit locations to determine the overall best calibration parameter.

The effect of the tectonic stress magnitude, σ_{tect} on the numerical damage geometry is partially dependent on its angular deviation from the adit axis, φ. This is a consequence of the damage being more sensitive to stresses perpendicular to a tunnel axis (normal stresses) than stresses parallel to it (Diederichs, 2007). For $\varphi = 0$, applied tectonic stress is parallel to the adit axis, which results in little variation in predicted damage geometry, even for large changes in σ_{tect} (see Figure 5.14). The converse is true for higher values of φ, in which a component of the applied stress acts in a direction normal to the adit axis. The normal stresses reduce the tangential stresses around the adit and resulted in lower depth of damage.

CHAPTER 6. DISCUSSION

6.1 Applications of the Visual m_i Approach

The photo-analysis technique is designed, not to be used as a replacement to traditional laboratory testing methods, but as a first pass approach when testing data is not yet available. Its aim is to provide a reasonable estimation of the Hoek-Brown properties of the rockmass, specific to the project site, allowing preliminary numerical analyses to be made or design parameters to be calculated.

One of the notable ways visual approach can be useful is its implementation in the calculation of the Hoek-Brown strength parameters based on the Geological Strength Index (GSI) characterization. GSI was designed to address the need to deliver more geologically representative data and was formulated as a strength reduction system that takes the intact Hoek-Brown properties of a rock, the degree of weathering and the density of fractures to calculate the corresponding rockmass strength parameters. The GSI for a given rockmass can be calculated in the field using the GSI chart (Figure 2.1). But ultimately, the most common application of the GSI of a rock is using equations 2, 3 and 4 to calculate the Hoek-Brown strength parameters, which require the intact material constant, m_i. In the early design stages, rock engineers typically consult to preexisting datasets or precalculated tables such as that shown in Table 6.1. The table shows the ranges of m_i for the most commonly occurring rocks based on laboratory datasets and estimations by Hoek (2000). It can be observed that the is a reasonable match in the m_i values of the light plutonic rocks (granite, granodiorite and diorite) in the table with their corresponding counterparts in the m_i values obtained from the SKB database, which ranges from approximately 20 to 30. It is recommended that the visual m_i approach be used in conjunction with the rock strength tables to obtain broader sense of rock strengths specific to the project site of interest.

Table 6.1. Values for m_i constant by rock group based on dataset from Hoek (2000) The values in parenthesis are estimates

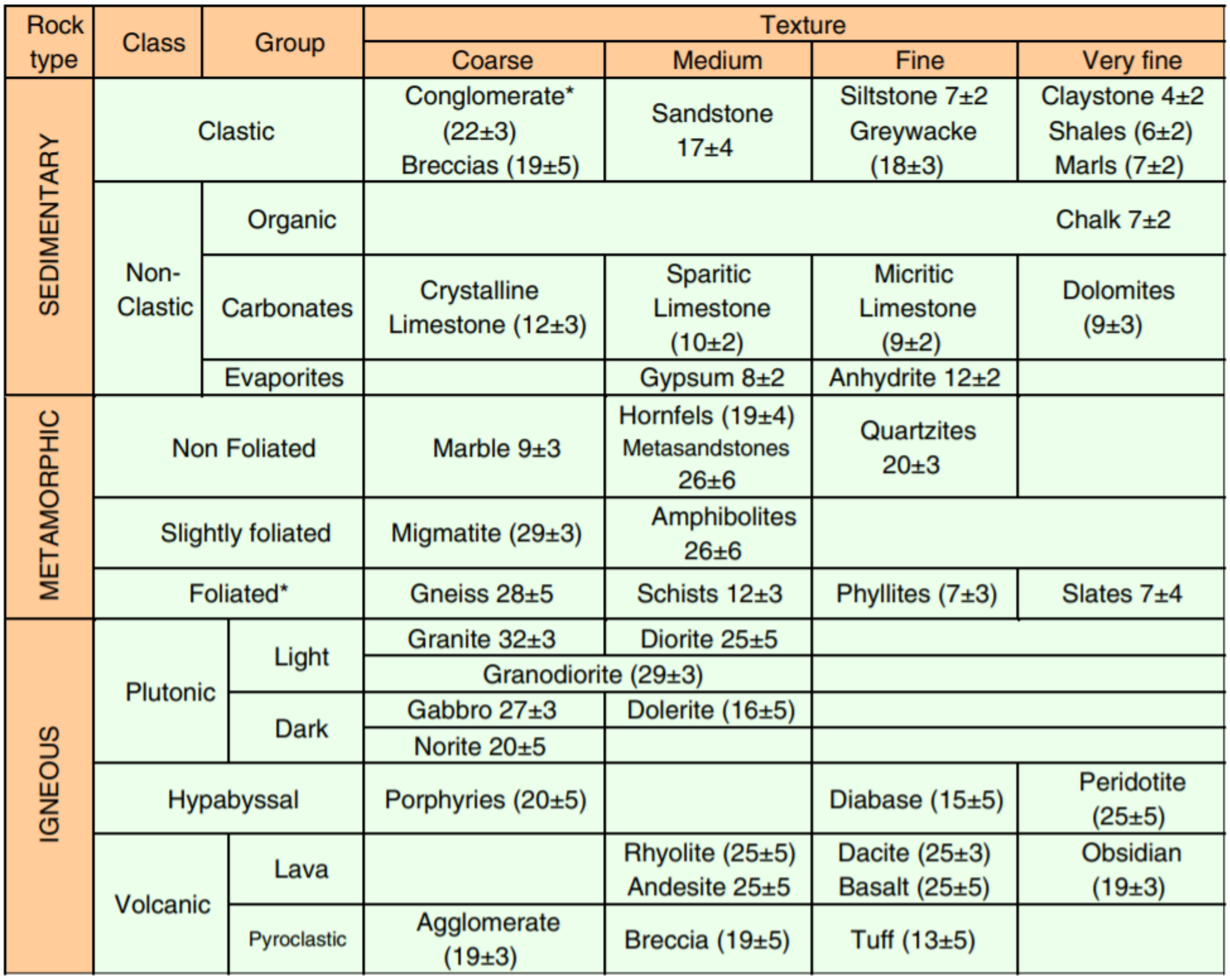

Rock type	Class	Group	Texture			
			Coarse	Medium	Fine	Very fine
SEDIMENTARY	Clastic		Conglomerate* (22±3) Breccias (19±5)	Sandstone 17±4	Siltstone 7±2 Greywacke (18±3)	Claystone 4±2 Shales (6±2) Marls (7±2)
	Non-Clastic	Organic				Chalk 7±2
		Carbonates	Crystalline Limestone (12±3)	Sparitic Limestone (10±2)	Micritic Limestone (9±2)	Dolomites (9±3)
		Evaporites		Gypsum 8±2	Anhydrite 12±2	
METAMORPHIC	Non Foliated		Marble 9±3	Hornfels (19±4) Metasandstones 26±6	Quartzites 20±3	
	Slightly foliated		Migmatite (29±3)	Amphibolites 26±6		
	Foliated*		Gneiss 28±5	Schists 12±3	Phyllites (7±3)	Slates 7±4
IGNEOUS	Plutonic	Light	Granite 32±3	Diorite 25±5		
			Granodiorite (29±3)			
		Dark	Gabbro 27±3	Dolerite (16±5)		
			Norite 20±5			
	Hypabyssal		Porphyries (20±5)		Diabase (15±5)	Peridotite (25±5)
	Volcanic	Lava		Rhyolite (25±5) Andesite 25±5	Dacite (25±3) Basalt (25±5)	Obsidian (19±3)
		Pyroclastic	Agglomerate (19±3)	Breccia (19±5)	Tuff (13±5)	

The visual m_i approach may also be applicable in other numerical modelling applications such as the DISL approach, which is very useful for modelling brittle damage in deep seated tunnel. In DISL models, specific guidelines and equations are used to determine the peak and residual Hoek-Brown envelopes. The DISL approach was used in the previous chapter for calibration of numerical models to determine the stress regime around the Bedretto adit. One observation that can be made is that the equations for the DISL parameters depend only on UCS, CI and tensile strength (see Table 6.2). And so different rocks with the same UCS/T ratio could have the same DISL envelopes, especially when CI is calculated as % UCS rather than obtained independently from acoustic emission data. In the original formulation of the peak failure envelope, Diederichs (2007) considered to be equivalent to the classic Sheorey quotient, “UCS/T”. It is worth noting that the Sheorey quotient is already included in the visual m_i equation (cite equation). The Sheorey quotient has previously been used as a rough estimate of *mi* in the absence of laboratory data (citations). The additional terms in the visual *mi* equation are present to account for rock grain influences om strength and are applied as a multiplied factor or a power relationship with the Sheorey quotient.

In this project, we explored on replacing the Sheorey quotient in the peak envelope used to calibrate the models in Chapter 5 with the visual *mi* obtained for the Bedretto granite. Pictures for the granite rock were obtained from the work of Huber (2004). It has to be noted that available suitable pictures were very few, and since Huber’s (2004) work only spanned between TM 4700 and TM 5100, it may not necessarily be representative of the overall state and mineralogy of the Bedretto granite. The estimated average visual m_i was 22.2, compared to a Sheorey quotient of 33 in the original models.

Table 6.2. Summary of peak and residual equations to determine DISL model input parameters (after Perras and Diederichs, 2006). The circled equation is the one in which the visual m_i can be applied. That is, term “UCS/T” is replaced by the visual m_i value

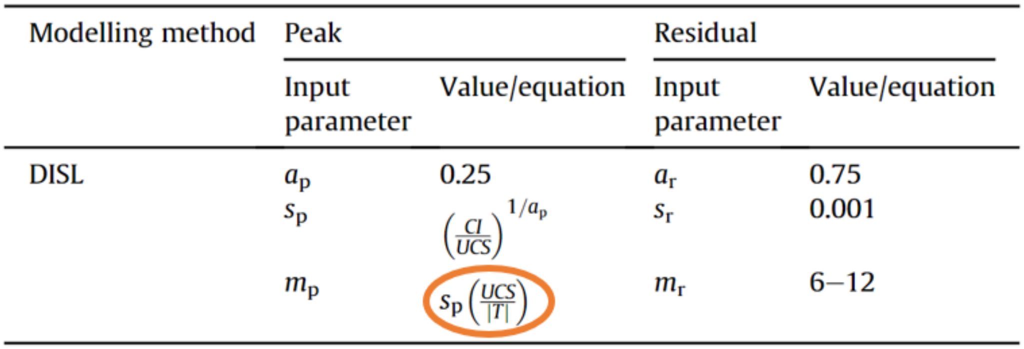

Modelling method	Peak		Residual	
	Input parameter	Value/equation	Input parameter	Value/equation
DISL	a_p	0.25	a_r	0.75
	s_p	$\left(\frac{CI}{UCS}\right)^{1/a_p}$	s_r	0.001
	m_p	$s_p\left(\frac{UCS}{\lvert T\rvert}\right)$	m_r	6–12

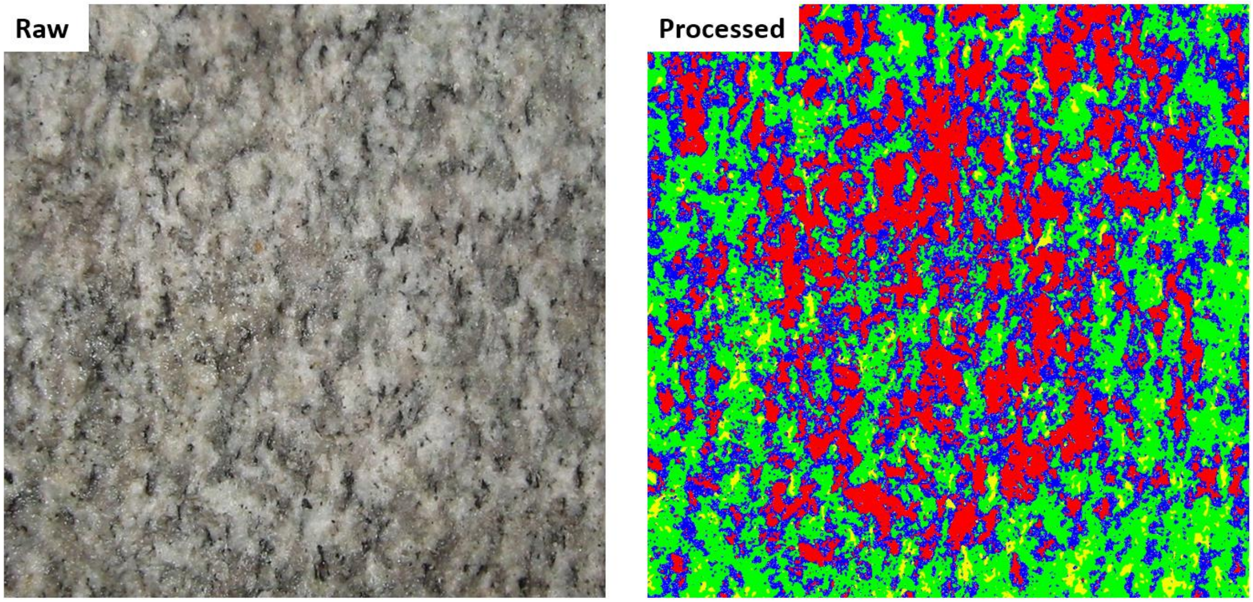

Figure 6.1. Close-up images of Bedretto granite for photo-analysis showing the raw and processed versions

The new peak envelopes were reapplied on the already calibrated and compared with the results of the original models. One such comparison in which the average visual m_i value was compared against the laboratory m_i value is shown in Figure 6.2. As will be expected for a model with a lower m_i value of the rock, the damage was more extensive in the new models. Additional models at the same location, using the minimum and maximum visual m_i values (17.02 and 28.41 respectively) all showed an increase in extent of damage when compared with the model with laboratory-estimated m_i as well as field measured damage depths. These results are summarized in Table 6.3. In the table, the "field measurement" row represents the average of the three groups of field values closest to TM 5100. Overall, there was an increase in damage depths for each of the visual models ranging from a 4% increase (max visual m_i model) to a 35 % increase (min visual m_i model) over the lab m_i model. The lab m_i model shows damage extents that were closest to the field measurements, while the max visual m_i model gives damage values closest to the lab. The average visual model however conservatively overestimates the extent of damage in the adit, which is suitable for preliminary design purposes.

The takeaway is that had the modified peak envelopes be used in the original calibration process, the estimated stress region might have been different, perhaps not to significantly. However, it cannot be stressed enough that the original goal of the image analysis technique is not to be used as a replacement to mainstream modelling procedures used in rock engineering project, and that, rigorous laboratory data is always preferrable over the visual estimate. As such, it should only be used in the early design stages, while laboratory test results.

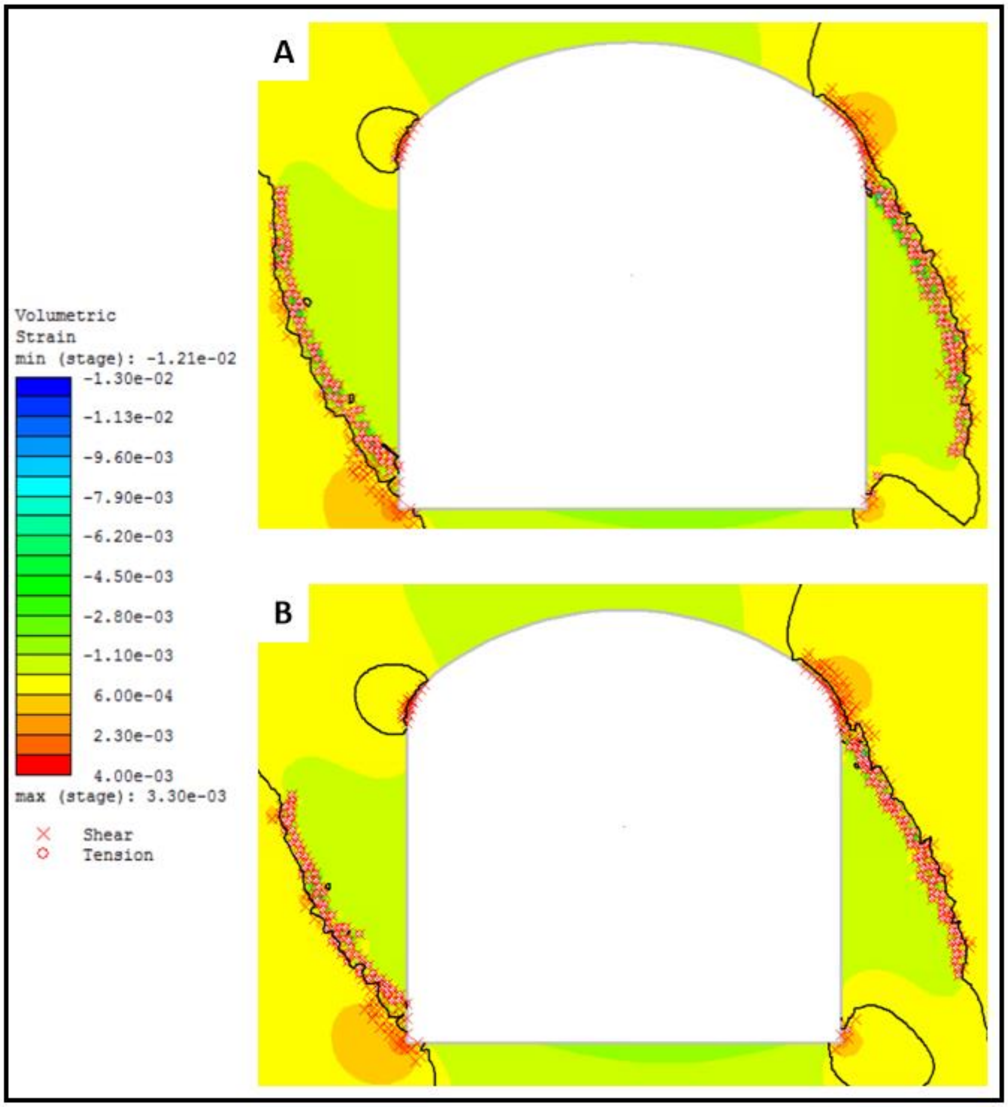

Figure 6.2. Comparison of model results with the (A) Original DISL formulation and (B) Sheorey quotient replaced with average visual m_i at TM 5100. The black isoline is the transition between yield in compression and tension, which represents the depth of overbreak.

Table 6.3. Summary of extents of damage obtained for all model types and field measurement at TM 5100

Model Type	**Extent of Damage (m)**	
	Western wall	**Eastern wall**
Min visual m_i	0.71	0.69
Avg visual m_i	0.63	0.65
Max visual m_i	0.63	0.53
Lab m_i	0.6	0.51
Field Measurement	0.49	0.5

6.2 Limitations of the Visual m_i Approach

The visual approach to making estimates of m_i values is a useful tool that can be used in preliminary rock engineering project designs when applied appropriately. It is however necessary that the boundaries of applicability of this approach be discussed and recognized.

Since the approach directly used sample photos to make estimates of the parameters in Eqn 17, the resolution of the photo can be a limiting factor in the software's ability to distinguish rock grains, particularly for fine grained rocks such as limestone. In general, the theoretically smallest grain that can be individually distinguished is equal to the size of a pixel in the image, thus the accuracy of the approach will be impacted if the pixel size in the photo is larger than the smallest grains in the rock. The ideal sample photos for the visual approach are photos obtained from thin section analyses, which will show very detailed close-up views of the rock grains. If thin section photos are not available, close up pictures taken from a high-quality camera are recommended. For fine grained rocks, regions of similar minerals can be distinguished from the photo technique and the smallest grain size can be approximated.

The visual approach is also only appropriate for photos taken on samples with flat surfaces. This is necessary in order to accurately determine the dimensions of the grain. A sample with curved or bumpy surfaces such as a cylindrical core or an unpolished piece of rock will have faces whose normals are not perpendicular to the plane of the camera, resulting in distortion of the grain shapes. Photos should be taken on Brazilian samples, end of UCS or Triaxial samples or otherwise a rock sample with a flat surface. If curved samples such as cylindrical cores are used, additional pre-processing has to be performed to correct image distortion.

Lastly, because the identification of rock grains involved thresholding certain ranges in the color spectrum, the approach may be difficult to apply on rocks that are visually homogeneous. An example of such a rock is basalt, which it is a dark-colored extrusive igneous rock. Such rocks are often homogenously dark colored, and so all the grains will fall within a very narrow band in the black-white color spectrum, making it difficult to distinguish the grains. In most cases, a thin section photo is the best option, as a true representation of the grain or crystal boundaries can be identified more clearly and in some cases it maybe the only viable method to estimate the m_i parameter with the proposed visual technique.

In order to remove surface impurities and irregularities, it is recommended that rock surfaces be cleaned and polished. However, care must be taken to ensure light reflections caused by polished surfaces are not captured in sample photos. Photos should be taken under uniform ambient light conditions.

CHAPTER 7. SUMMARY AND CONCLUSIONS

7.1 Summary of Findings

1. Many rock grain parameters including grain size and distribution, grain shape and grain orientation exhibit various degrees of influences on the strength of rocks. However, these grain parameters are intricately related to each other such that their influence on rock geomechanical properties cannot be independently accessed. For example,
    - Higher porosity tends to weaken rocks, however, the extent of rock degradation for a given percentage increase depends on grain size distribution. For poorly sorted rocks, there is less degradation of strength per porosity increase compared to well sorted rocks.
    - For most rocks, decreasing overall average grain size results in a corresponding increase in tensile strength. However, for a given average grain size, a higher abundance of sheet minerals such as mica results in degradation on tensile strength.
2. The alternate approach for making estimates of m_i during early design stages shows good promise in their feasibility, when compared to laboratory values. Among the rock types tested, the visual approach showed an overall accuracy of 81%. The procedure works best for coarse grained rocks such as granite, showing an accuracy of up to 96%, but is less suitable for small grained rocks such as limestone, with a 59% accuracy. It can be used as a good alternative to other precalculated rock strength tables. In addition, it is noted that;
    - The accuracy of m_i estimates made from photo-analysis is directly dependent on the quality of photos used in the process. The small grains that can be distinguished by an image analysis software is limited by the pixel sizes of the image (resolution).

    - The photo-analysis technique is most suitable for medium to coarse grain rocks since the grains can be easily distinguished and visual measurements of interlock values are more accurate.
    - The calculated value of m_i is most sensitive to changes in the kurtosis modifier parameter and least sensitive to changes in the anisotropy parameter.

3. A numerical back analysis exercise performed on the Bedretto adit in Switzerland against measured damage geometries inside the adit using LiDAR scanning equipment showed that the adit is subjected to a regional tectonic stress of magnitude approximately 20 MPa, oriented 30° anticlockwise from the adit axis and dipping 15°. This translates to a stress field orientation of N72W (or N108E), representing a WNW-ESE orientation.
4. Minimum, average and maximum visual m_i parameters obtained from a limited set of close-up photos of the granitic rock material in the Bedretto adit were applied into the back-calculated numerical models and compared with the original models which used laboratory-based m_i values. The results showed that the visual estimates were conservative and resulted in an overestimation of the depths of damage by up between 4 - 35%, with the maximum visual estimated m_i value giving the closest depth of overbreak to that measured in the adit.
5. The lab derived m_i value gave a similar depth of failure to that observed in-situ, which speaks to the importance of conducting proper laboratory testing to derive numerical model input parameters for detailed design.

7.2 Conclusions

The re-examination of the database from Perras and Diederichs (2014) with the lens of geological influence on the compressive and tensile strength, has shown that the approach of Carter (2019) is a step in the right direction. Certainly, the influence of grain interlocking, grain size, anisotropy, among other elements, influences the standard laboratory tests the rock engineering community relies on. The high costs associated with laboratory testing and field sampling, as well as and more likely, the desire to make budgets as small as possible, has led many practitioners to rely on estimated values for design. An improved approach, that takes a small amount of additional time during core logging, to estimate the geological characteristics that influence the m_i parameter appears useful to help aid parameter definition, with an overall accuracy of 81%. The approach works best in coarse grained rocks in which the grain can be easily distinguished. Such an approach appears significantly better than simply selecting a value from already published tabulations based solely on the named rock type in question.

A numerical approach to estimating the potential stress field around an adit based on measured brittle damage was performed, the results of which was used as a tool to explore the potential for the visual m_i approach to be applied in numerical modelling applications. The results showed that the adit is subjected to a field stress with a magnitude of 20 MPa, oriented WNW-ESE and dipping 15°. When m_i values of the granitic rock estimated using the visual approach was applied in the models, the models showed conservatively higher depths of damage with overestimations ranging from 4% to 35%. The maximum visual estimated m_i value gave the closest depth of overbreak to that measured in the adit. Further analyses of the data and further laboratory testing to critically compare laboratory-based m_i values with those determined from the novel visual approach are needed.

REFERENCES

Alcaíno-Olivares, R. (2017). *Assessing the Influence of The Environmental Conditions on the Fracture Growth in the Bedretto Tunnel - Switzerland*. University of Leeds.

Aliha, M. R. M. (2014). Indirect tensile test assessments for rock materials using 3-D disc-type specimens. *Arabian Journal of Geosciences*, *7*(11), 4757–4766. https://doi.org/10.1007/s12517-013-1037-8.

Amberg, R. (1983). Design and construction of the Furka base tunnel. *Rock Mechanics and Rock Engineering*, *16*(4), 215–231. https://doi.org/10.1007/BF01042358.

Basu, A., & Aydin, A. (2006). Predicting uniaxial compressive strength by point load test: Significance of cone penetration. *Rock Mechanics and Rock Engineering*, *39*(5), 483–490. https://doi.org/10.1007/s00603-006-0082-y.

Bell, J. S., & Gough, D. I. (1979). Northeast-southwest compressive stress in Alberta evidence from oil wells. Earth and Planetary Science Letters, 45(2), 475–482.

Betournay, M. 1983. Examinatin of URL-1, URL-2, and URL-5 Uniaxial compressive and tensile test data. Canadian Centre for Mineral and Energy Technology, Mining Research Laboratories Division Report, ERP/MRL 83-26(TR).

Bieniawski, Z. T. (1976). Rock mass classification in rock engineering. *Exploration for Rock Engineering, Proc. of the Symp*, *1*, 97–106.

Bieniawski, Z. T., & Bernede, M. J. (1979). Suggested methods for determining the uniaxial compressive strength and deformability of rock materials. *International Journal of Rock Mechanics and Mining Sciences & Geomechanics Abstracts*, *16*(2), 138–140.

https://doi.org/10.1016/0148-9062(79)91451-7.

Cai, M. (2010) Practical estimates of tensile strength and Hoek-Brown strength parameter mi of brittle rock. Rock Mech. Rock Eng. 43(2): 167–184.

Carter, T.G. (2019). A suggested visual approach for estimating Hoek-Brown mi for different rock types. *Rock Mechanics for Natural Resources and Infrastructure Development- Proceedings of the 14th International Congress on Rock Mechanics and Rock Engineering, ISRM 2019*, 491–503.

Carter, Trevor G., & Marinos, V. (2020). Putting Geological Focus Back into Rock Engineering Design. *Rock Mechanics and Rock Engineering*, (0123456789). https://doi.org/10.1007/s00603-020-02177-1.

Churcher, P. L., French, P. R., Shaw, J. C., & Schramm, L. L. (1991) Rock Properties of Berea Sandstone, Baker Dolomite, and Indiana Limestone. SPE International Symposium on Oilfield Chemistry.

Cordero, Z. C., Knight, B. E., & Schuh, C. A. (2016). Six decades of the Hall–Petch effect – a survey of grain-size strengthening studies on pure metals. *International Materials Reviews*, *61*(8), 495–512. https://doi.org/10.1080/09506608.2016.1191808.

Cowie, S., & Walton, G. (2018). The effect of mineralogical parameters on the mechanical properties of granitic rocks. *Engineering Geology*, *240*(April), 204–225. https://doi.org/10.1016/j.enggeo.2018.04.021.

Dan D. Q, Konietzky. H, Herbst M. (2013). Brazilian tensile strength tests on some anisotropic rocks. Int J Rock Mech Min Sci 58:1–7.

Davies, J. (2019) - Geological Characterization of the Bedretto Underground Laboratory for Geoenergies, MSc Thesis, Department of Earth Sciences, ETH Zurich.

Diederichs, M. (2007). The 2003 Canadian Geotechnical Colloquium: Mechanistic interpretation and practical application of damage and spalling prediction criteria for deep tunnelling. *Canadian Geotechnical Journal*, *44*(9), 1082–1116. https://doi.org/10.1139/T07-033.

Diederichs, M. S., & Martin, C. D. (2010). Measurement of spalling parameters from laboratory testing. In *Rock Mechanics in Civil and Environmental Engineering - Proceedings of the European Rock Mechanics Symposium, EUROCK 2010* (pp. 323–326).

Diederichs, M.S., Kaiser, P. K., & Eberhardt, E. (2004). Damage initiation and propagation in hard rock during tunnelling and the influence of near-face stress rotation. *International Journal of Rock Mechanics and Mining Sciences*, *41*(5), 785–812. https://doi.org/10.1016/j.ijrmms.2004.02.003.

Diederichs, Mark S. (2007). The 2003 Canadian Geotechnical Colloquium: Mechanistic interpretation and practical application of damage and spalling prediction criteria for deep tunnelling. *Canadian Geotechnical Journal*, *44*(9), 1082–1116. https://doi.org/10.1139/T07-033.

Eberhardt, E., Stead, D., Stimpson, B., & Read, R. S. (1998). Identifying crack initiation and propagation thresholds in brittle rock. *Canadian Geotechnical Journal*, *35*(2), 222–233. https://doi.org/10.1139/t97-091.

Ferreira, T. and W. Rasband. (2012) ImageJ User Guide. IJ 1.46r. Revised edition.

Frizzell, R., Cotesta, L., and Usher, S. 2008. Phase I Regional Geology, Southern Ontario (OPG

00216-REP-01300-00007-R00). Toronto, Ontario.

Ghazvinian, E., Perras, M., Diederichs, M., & Labrie, D. (2013). The effect of anisotropy on crack damage thresholds in brittle rocks. *47th US Rock Mechanics / Geomechanics Symposium 2013*, *2*(January 2016), 1110–1119.

Ghazvinian, E. (2015) Fracture Initiation and Propagation in Low Porosity Crystalline Rocks: Implications For Excavation Damage Zone (Edz) Mechanics, PhD Dissertation, Dept of Geological Science and Geological Engineering, Queen's University.

Gischig, V. S., Giardini, D., Amann, F., Hertrich, M., Krietsch, H., Loew, S., … Valley, B. (2020). Hydraulic stimulation and fluid circulation experiments in underground laboratories: Stepping up the scale towards engineered geothermal systems. *Geomechanics for Energy and the Environment*, *24*, 100175. https://doi.org/10.1016/j.gete.2019.100175.

Haimson, B. C., & Song, I. (1993). Laboratory study of borehole breakouts in Cordova Cream: a case of shear failure mechanism. International Journal of Rock Mechanics and Mining Sciences And, 30(7), 1047–1056.

Hajiabdolmajid, V., Kaiser, P. K., & Martin, C. D. (2002). Modelling brittle failure of rock. *International Journal of Rock Mechanics and Mining Sciences*, *39*(6), 731–741. https://doi.org/10.1016/S1365-1609(02)00051-5.

Hatzor, Y. H., & Palchik, V. (1997). The influence of grain size and porosity on crack initiation stress and critical flaw length in dolomites. *International Journal of Rock Mechanics and Mining Sciences*, *34*(5), 805–816. https://doi.org/10.1016/S1365-1609(96)00066-6.

Hoek, E., & Brown, E. T. (1980). Empirical strength criterion for rock masses. *International*

Journal of Rock Mechanics and Mining Sciences & Geomechanics Abstracts, *18*(2), 23. https://doi.org/10.1016/0148-9062(81)90766-X.

Hoek, E., & Brown, E. T. (2018). The Hoek-Brown failure criterion and GSI-2018 edition. *Journal of Rock Mechanics and Geotechnical Engineering*, *11*(3), 445–463. https://doi.org/10.1016/j.jrmge.2018.08.001.

Hoek, E. and Marinos, P. 2000. Predicting Tunnel Squeezing. Tunnels and Tunnelling International. Part 1 – November 2000, Part 2 – December, 2000.

Hoek, E., Carranza-Torres, C., & Corkum, B. (2002). Hoek-brown failure criterion – 2002 edition. *Proceedings of the 5th North Amer. Rock Mech. Symp. and 17th Tunnel. Assoc. of Canada Conf.: NARMS-TAC*, 267–273. https://doi.org/10.1016/0148-9062(74)91782-3

Huber, B. (2004). *Stress-induced Fractures in the Deep-seated Bedretto Tunnel: Their Geological and Geomechanical Reasons*. ETH Zurich.

ISRM (1978) Suggested methods for determining tensile strength of rock materials. Int J Rock Mech Min Sci Geomech Abstr 15(3):99–103.

ISRM (1985). Suggested method for determining point load strength. Int. J. Rock Mech. Min. Sci. 22, 53–60.

Jacobsson. L. 2004. Site investigation reports. Swedish nuclear fuel and waste management Co. Technical Reports. P-04-263, P-04-261, P-04-262, P-04-173, P-04-225, P-04-229, P-04-268, P-04-168.

Jacobsson. L. 2005. Site investigation reports. Swedish nuclear fuel and waste management Co. Technical Reports. P-05-98, P-05-97, P-05-100.

Jacobsson. L. 2006. Site investigation reports. Swedish nuclear fuel and waste management Co. Technical Reports. P-06-234.

Keller, F., & Schneider, T. R. (1982). Geologie und Geotechnik Furka Basistunnel. https://doi.org/10.5169/seals-74820.

Krumbein, W. C. (1941). Measurement and Geological Significance of Shape and Roundness of Sedimentary Particles. *SEPM Journal of Sedimentary Research, Vol. 11*. https://doi.org/10.1306/D42690F3-2B26-11D7-8648000102C1865D.

Lajtai, E. Z. (1998). Microscopic fracture processes in a granite. *Rock Mechanics and Rock Engineering*, *31*(4), 237–250. https://doi.org/10.1007/s006030050023.

Langford, J. C. (2013). *Application of Reliability Methods to the Design of Underground Structures*. Queen’s University.

Lee, S. M., Park, B. S., & Lee, S. W. (2004). Analysis of rockbursts that have occurred in a waterway tunnel in Korea. International Journal of Rock Mechanics and Mining Sciences, 41(SUPPL. 1), 1–6.

Lee, M., & Haimson, B. (1993). Laboratory study of borehole breakouts in Lac du Bonnet granite: a case of extensile failure mechanism. International Journal of Rock Mechanics and Mining Sciences And, 30(7), 1039–1045.

Li, L., & Aubertin, M. (2003). A general relationship between porosity and uniaxial strength of engineering materials. *Canadian Journal of Civil Engineering*, *30*(4), 644–658. https://doi.org/10.1139/l03-012.

Lutzenkirchen, V. (2002). *Structural Geology and Hydrogeology of Brittle Fault Zones in the*

Central and Eastern Gotthard Massif, Switzerland. ETH Zurich.

Lützenkirchen, V., & Loew, S. (2011). Late Alpine brittle faulting in the Rotondo granite (Switzerland): Deformation mechanisms and fault evolution. *Swiss Journal of Geosciences*, *104*(1), 31–54. https://doi.org/10.1007/s00015-010-0050-0.

Martin, C. ., Kaiser, P. ., & McCreath, D. . (1999). Hoek-Brown parameters for predicting the depth of brittle failure around tunnels. *Canadian Geotechnical Journal*, *36*(1), 136–151. https://doi.org/10.1139/t98-072.

Martin, C. D., & Chandler, N. A. (1994). The progressive fracture of Lac du Bonnet granite. *International Journal of Rock Mechanics and Mining Sciences & Geomechanics Abstracts*, *31*(6), 643–659. https://doi.org/10.1016/0148-9062(94)90005-1

Martin, C. D. D. (1997). The effect of cohesion loss and stress path on brittle rock strength. *Canadian Geotechnical Journal*, *34*, 698–725. https://doi.org/10.1139/t97-030.

Mishra, D.A. and Basu, A. (2012). Use of the block punch test to predict the compressive and tensile strengths of rocks. Int. J. Rock. Mech. Min. Sci. 51:119–127.

Nålsund R, Jensen, V (2013) Influence of mineral grain size, grain size distribution and micro-cracks on rocks mechanical strength. 14th Euro-seminar on Microscopy Applied to Building Materials, 1–12. Copenhagen, Denmark..

Moos, D., & Zoback, M. D. (1990). Utilization of observations of well bore failure to constrain the orientation and magnitude of crustal stresses: application to continental, Deep Sea Drilling Project, and Ocean Drilling Program boreholes. Journal of Geophysical Research, 95(B6), 9305–9325.

Morris, J.W. 2001 Hall-Petch effect. The influence of grain size on the mechanical properties of steel. In: Takaki S, Maki T, editors. Proceedings of the int symposium on ultrafine grained steels, Tokyo: Iron and Steel Institute; 2001. p. 34.

Ofterdinger, U. S., Renard, P., & Loew, S. (2014). Hydraulic subsurface measurements and hydrodynamic modelling as indicators for groundwater flow systems in the Rotondo granite, Central Alps (Switzerland). *Hydrological Processes*, *28*(2), 255–278. https://doi.org/10.1002/hyp.9568.

Ofterdinger, Ulrich S. (2004). Environmental Isotopes as Indicators for Ground Water Recharge to Fractured Granite. *Ground Water*, *42*(6), 868–879. https://doi.org/10.1111/j.1745-6584.2004.t01-5-.x.

Paraskevopoulou, C., Perras, M., Diederichs, M., Loew, S., Lam, T., & Jensen, M. (2017). Time-Dependent Behaviour of Brittle Rocks Based on Static Load Laboratory Tests. *Geotechnical and Geological Engineering*, *36*(1), 337–376. https://doi.org/10.1007/s10706-017-0331-8

Perras, M. A., & Diederichs, M. S. (2014). A Review of the Tensile Strength of Rock: Concepts and Testing. *Geotechnical and Geological Engineering*, *32*(2), 525–546. https://doi.org/10.1007/s10706-014-9732-0.

Perras, M. A., & Diederichs, M. S. (2016). Predicting excavation damage zone depths in brittle rocks. *Journal of Rock Mechanics and Geotechnical Engineering*, *8*(1), 60–74. https://doi.org/10.1016/j.jrmge.2015.11.004.

Rafiei Renani, H., & Martin, C. D. (2018). Cohesion degradation and friction mobilization in brittle failure of rocks. *International Journal of Rock Mechanics and Mining Sciences*, *106*, 1–13. https://doi.org/10.1016/j.ijrmms.2018.04.003.

Read, R. S. Ã. (2004). 20 years of excavation response studies at AECL's Underground Research Laboratory. *International Journal of Rock Mechanics & Mining Sciences*, *41*, 1251–1275. https://doi.org/10.1016/j.ijrmms.2004.09.012.

Read, S. A. L., and Richards, L. (2012) A comparative study of mi, the Hoek-Brown constant for intact rock material. Proc. 12th ISRM Congress, International Society for Rock Mechanics, Beijing, China, Eds. Qian, Zhou, Paper 139, pp. 805-810.

Read, S. A. L., and Richards, L. R. (2015) Guidelines for use of Tensile Data in the Calculation of the Hoek-Brown Constant mi. Proc. 13th ISRM Int. Cong. Rock Mech., Montreal, 13pp.

Richards, L. R. and Read, S.A.L. 2013. Estimation of Hoek-Brown parameter mi using Brazilian tensile test. Proc. 47th US Rock Mechanics / Geomechanics Symposium, San Francisco, USA 23-26 June, eds, A. Iannacchione et al. (Eds.), Paper ARMA/USRMS 13-465, 14pp.

Richards, L., & Romana, M. (2011). A comparative study of mi, the Hoek-Brown constant for intact rock material. *Proceedings 45th US Rock Mechs / Geomechanics Symposium, San Francisco, USA, 26-29 June 2011, Eds. A. Iannacchione et Al., Paper ARMA / USRMS 11-246*, 805–810. https://doi.org/https://doi.org/10.1201/b11646-147.

Sano, O., Kudo, Y., & Mizuta, Y. (1992) Experimental determination of elastic constants of Oshima granite, Barre granite, and Chelmsford granite. J. Geophys. Res.: Solid Earth, 97(B3).

Shea, W. T., & Kronenberg, A. K. (1993). Strength and anisotropy of foliated rocks with varied mica contents. *Journal of Structural Geology*, *15*(9), 1097–1121. https://doi.org/https://doi.org/10.1016/0191-8141(93)90158-7.

Shen J, and Karakus, M. (2014). Simplified method for estimating the Hoek-Brown constant for intact rocks. J Geot. 0.1061/(ASCE).

Vakili, A., Albrecht, J., & Sandy, M. (2014). Rock strength anisotropy and its importance in underground geotechnical design. *Third Australasian Ground Control in Mining Conference*, (May), 167–179.

Walton, G. (2019). Initial guidelines for the selection of input parameters for cohesion-weakening-friction-strengthening (CWFS) analysis of excavations in brittle rock. *Tunnelling and Underground Space Technology*, *84*(November 2018), 189–200. https://doi.org/10.1016/j.tust.2018.11.019.

Waza, T., Kurita, K., & Mizutani, H. (1980). The effect of water on the subcritical crack growth in silicate rocks. *Tectonophysics*, *67*(1–2), 25–34. https://doi.org/10.1016/0040-1951(80)90162-6.

Wentworth, C.K. (1992) A scale of grade and class terms of clastic sediments. J. Geol., 30: 377-92.

Ziegler, M., Loew, S., & Bahat, D. (2014). Growth of exfoliation joints and near-surface stress orientations inferred from fractographic markings observed in the upper Aar valley (Swiss Alps). *Tectonophysics*, *626*(1), 1–20. https://doi.org/10.1016/j.tecto.2014.03.017

Zoback, M. D. (1985). Well bore breakouts and In situ stress. Journal of Geophysical Research, 90(Figure lc), 5523–5530

APPENDICES

Appendix A: Raw and Processed Sample Images for Visual m_i Determination

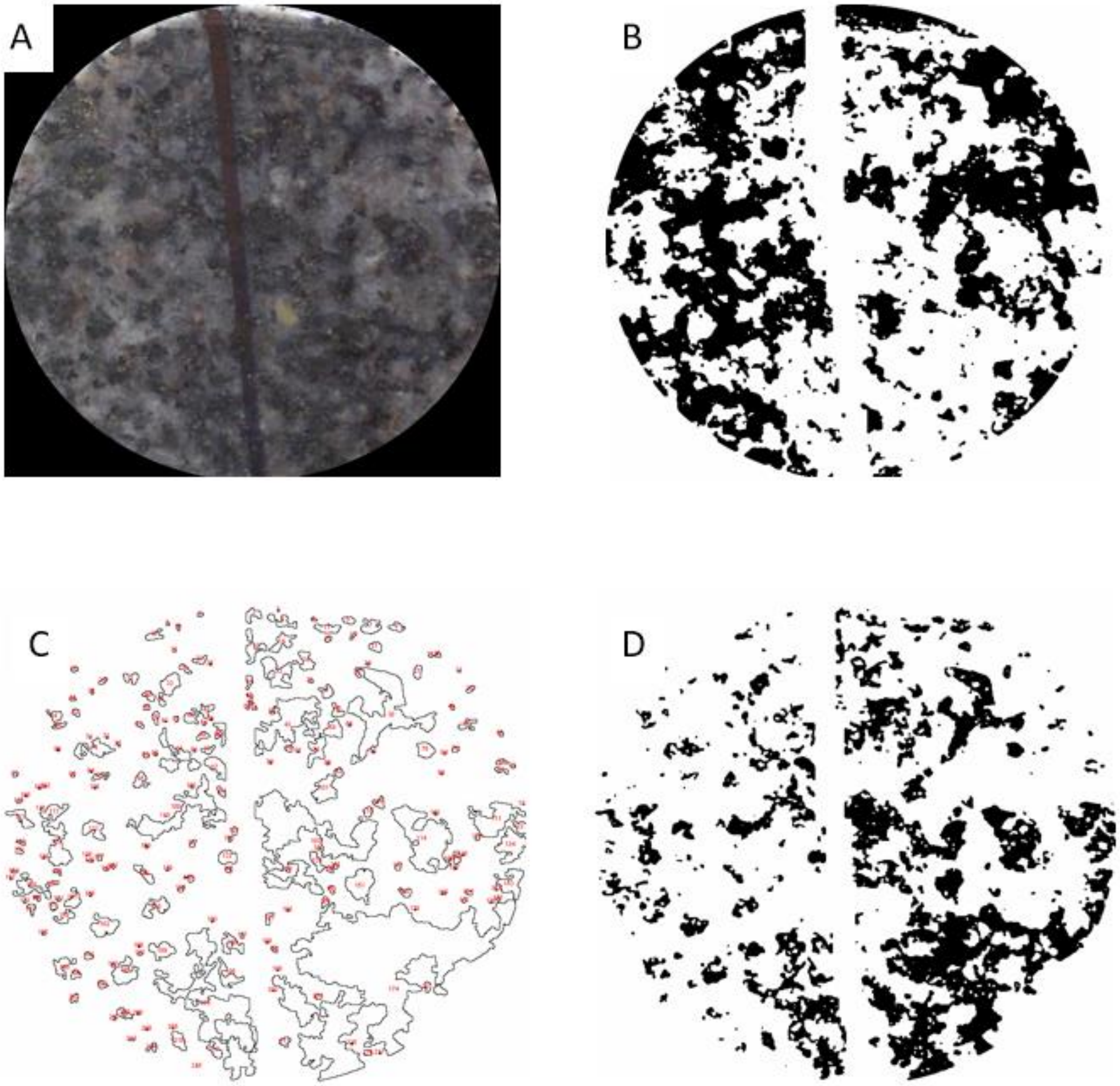

Figure A - 1: Avro Granite – KLX04A-110-4 (Jacobsson, 2004)

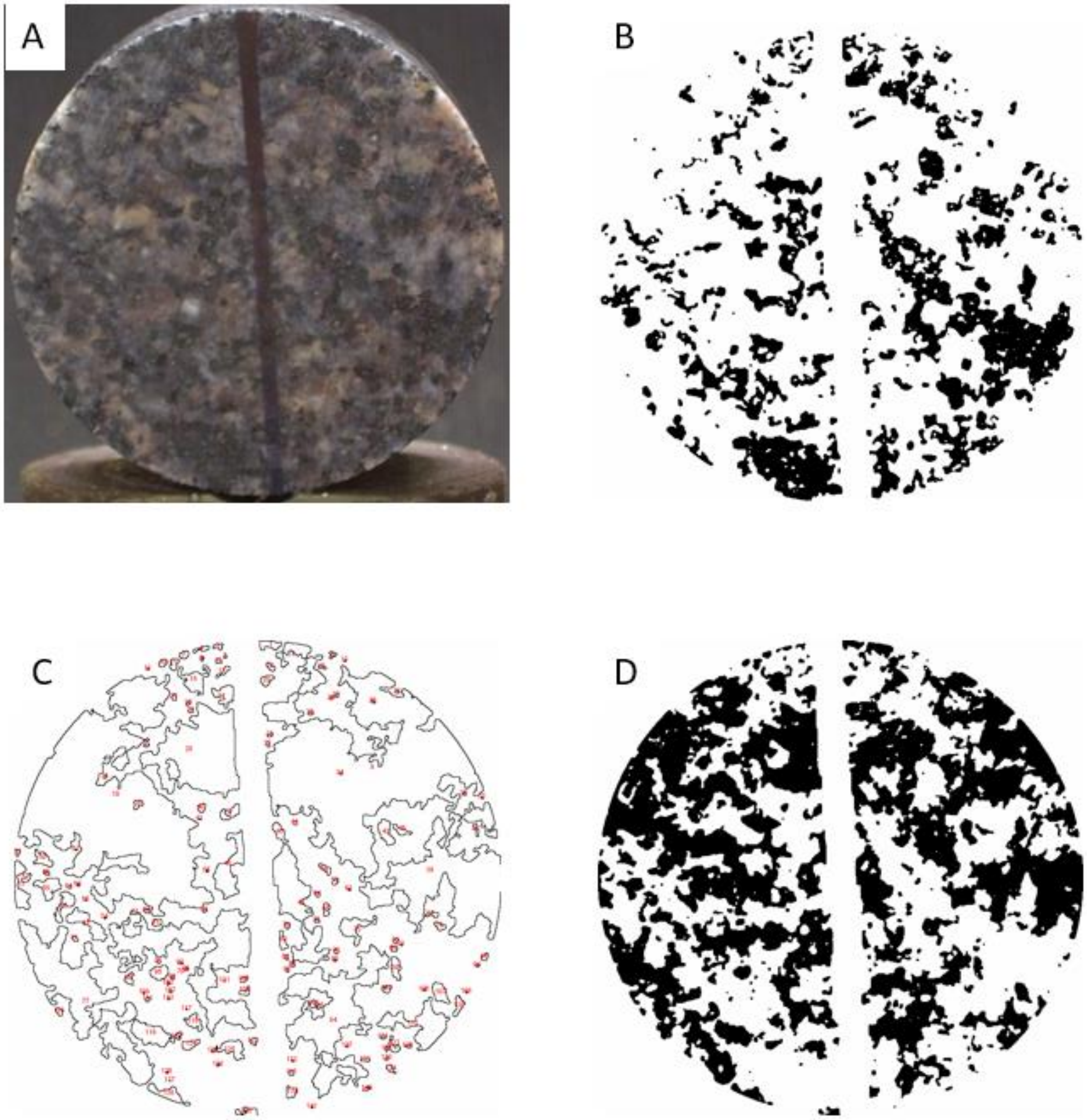

Figure A - 2: Avro Granite – KLX04A-110-13 (Jacobsson, 2004)

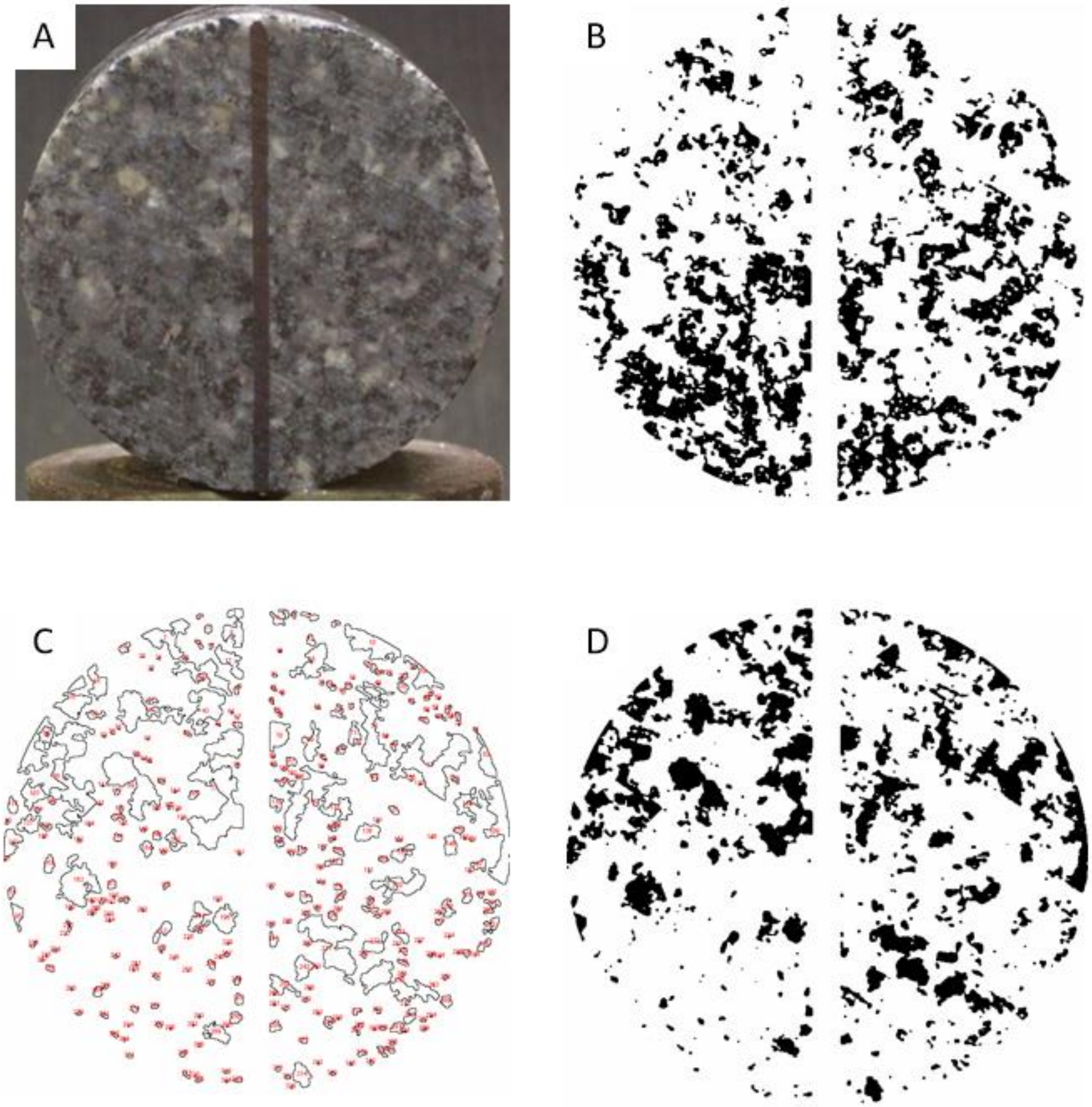

Figure A - 3: Avro Granite – KLX04A-110-18 (Jacobsson, 2004)

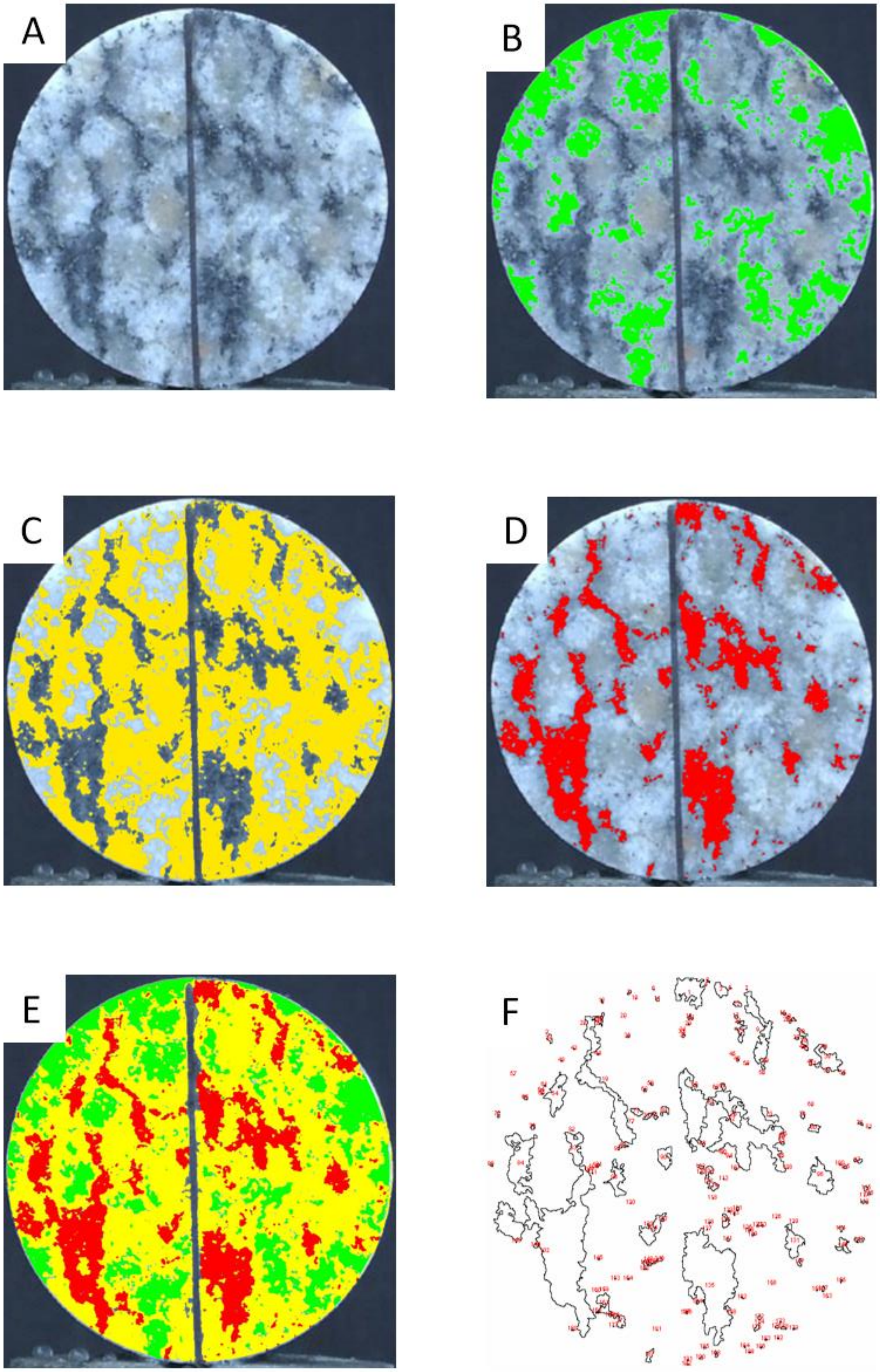

Figure A - 4: Medium grained granite – KFM05A-110-14 (Jacobsson, 2005)

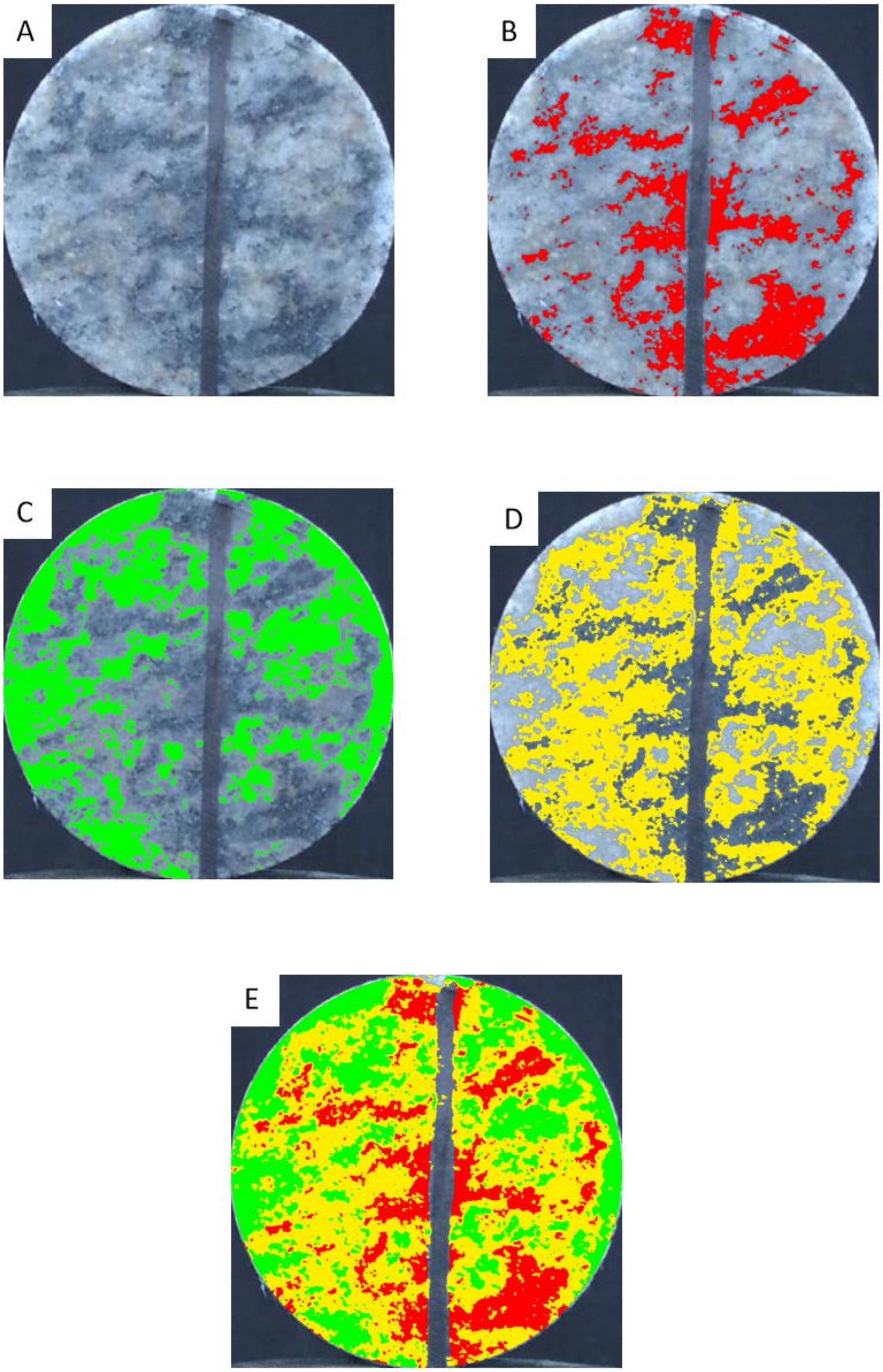

Figure A - 5: Medium grained granite – KFM05A-110-1 (Jacobsson, 2005)

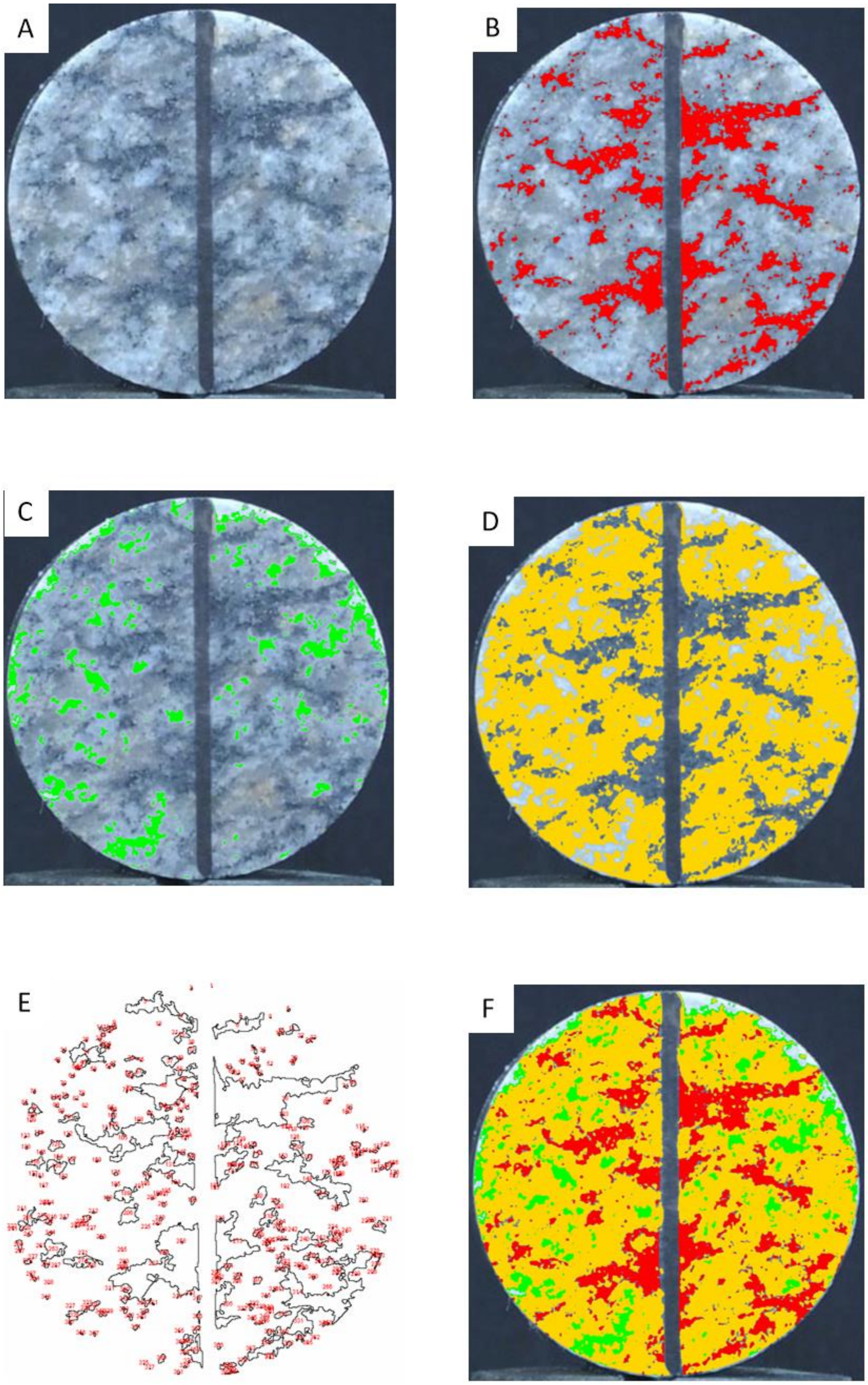

Figure A - 6: Medium grained granite – KFM05A-110-3 (Jacobsson, 2005)

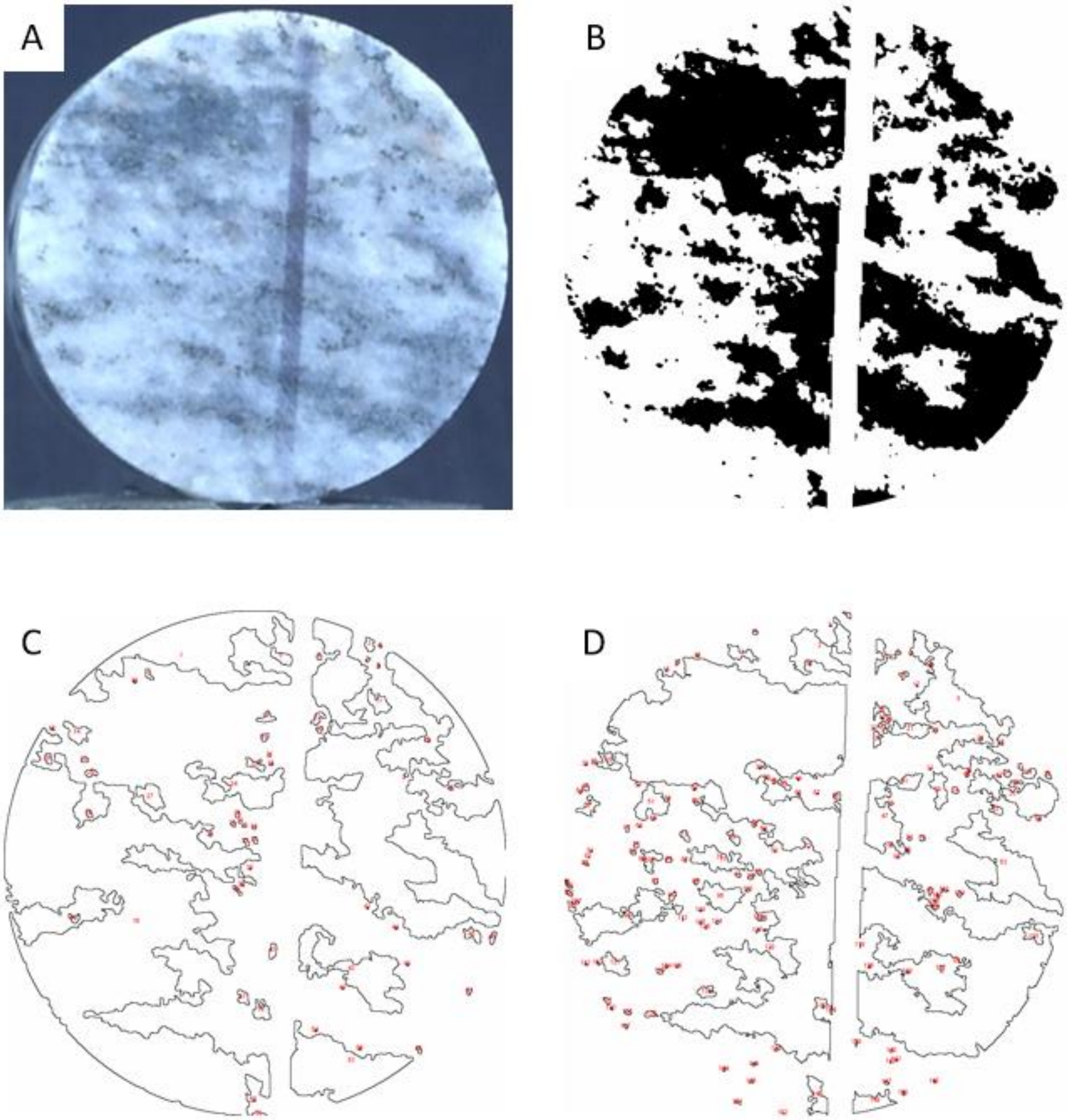

Figure A - 7: Granite-Granodiorite – KFM3A-110-26 (Jacobsson, 2004)

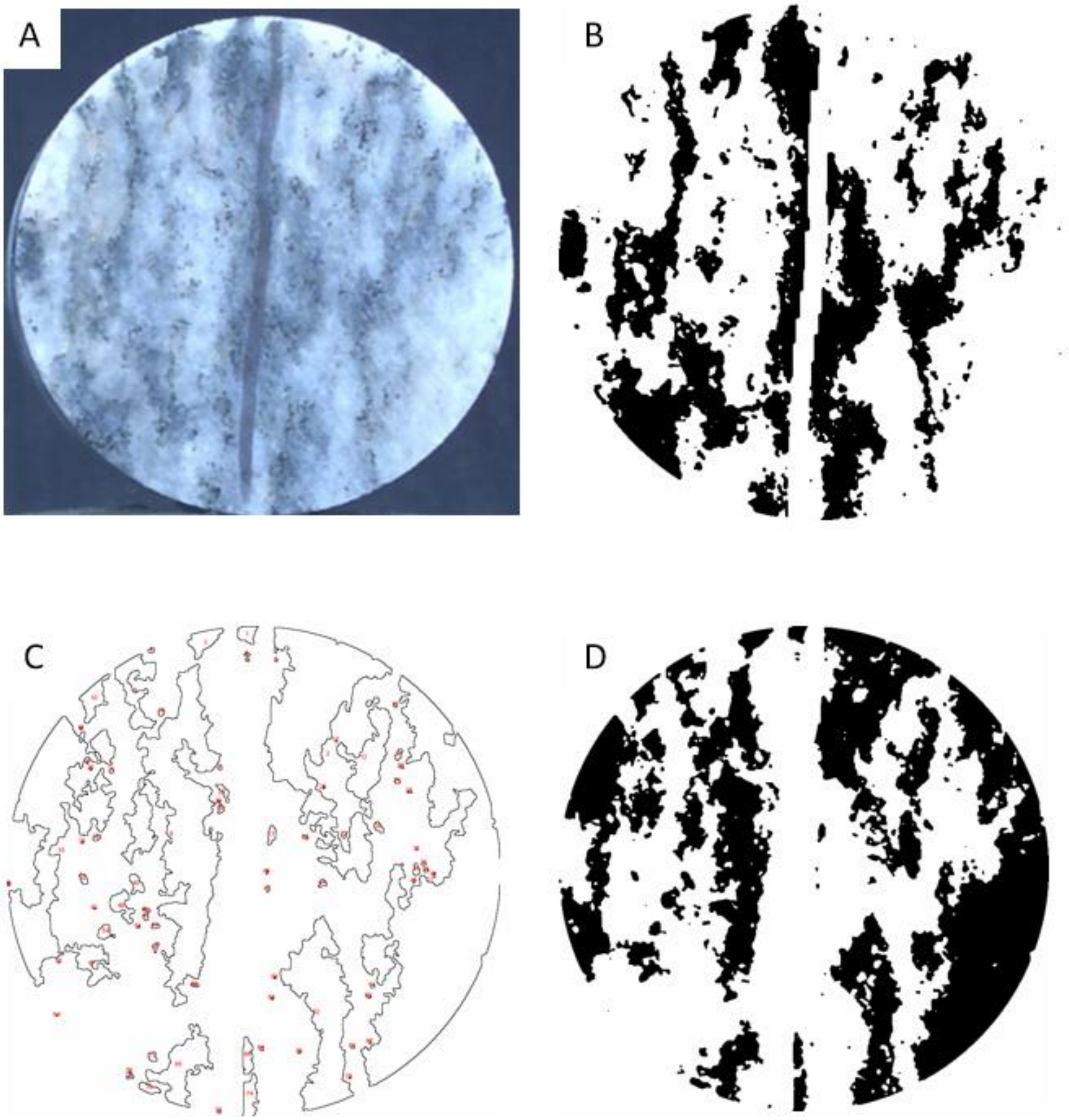

Figure A - 8: Granite-Granodiorite – KFM3A-110-33 (Jacobsson, 2004)

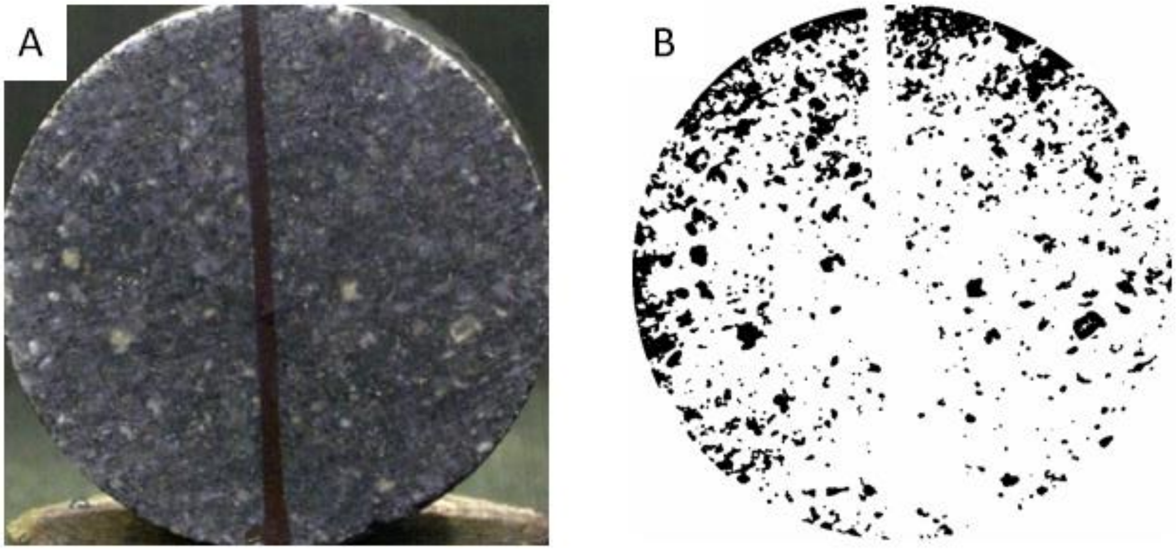

Figure A - 9: Granodiorite-Tonalite – KFM3A-110-14 (Jacobsson, 2004)

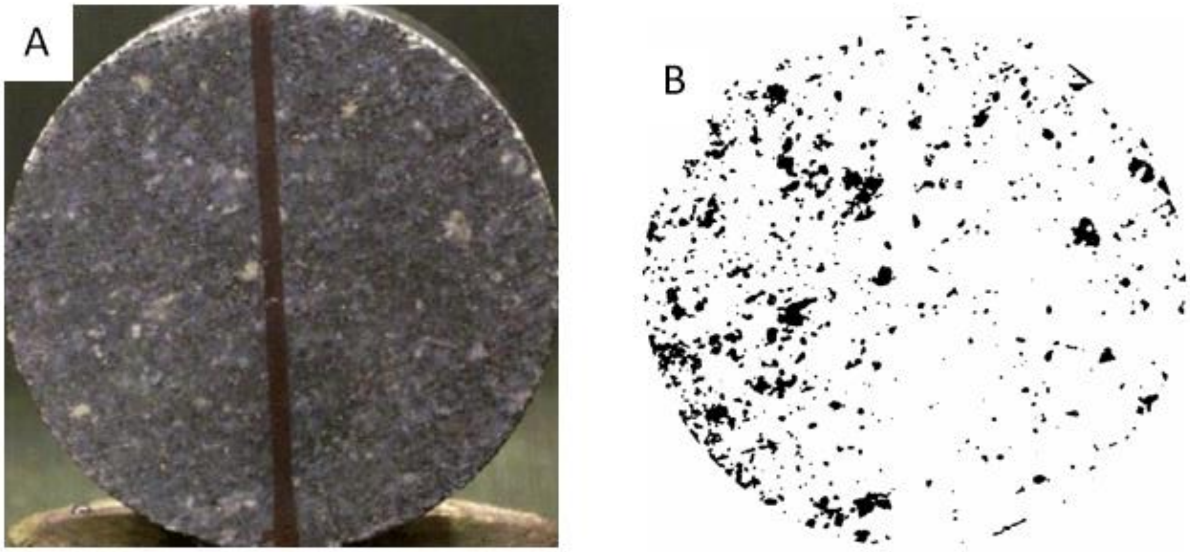

Figure A - 10: Granodiorite-Tonalite – KFM3A-110-16 (Jacobsson, 2004)

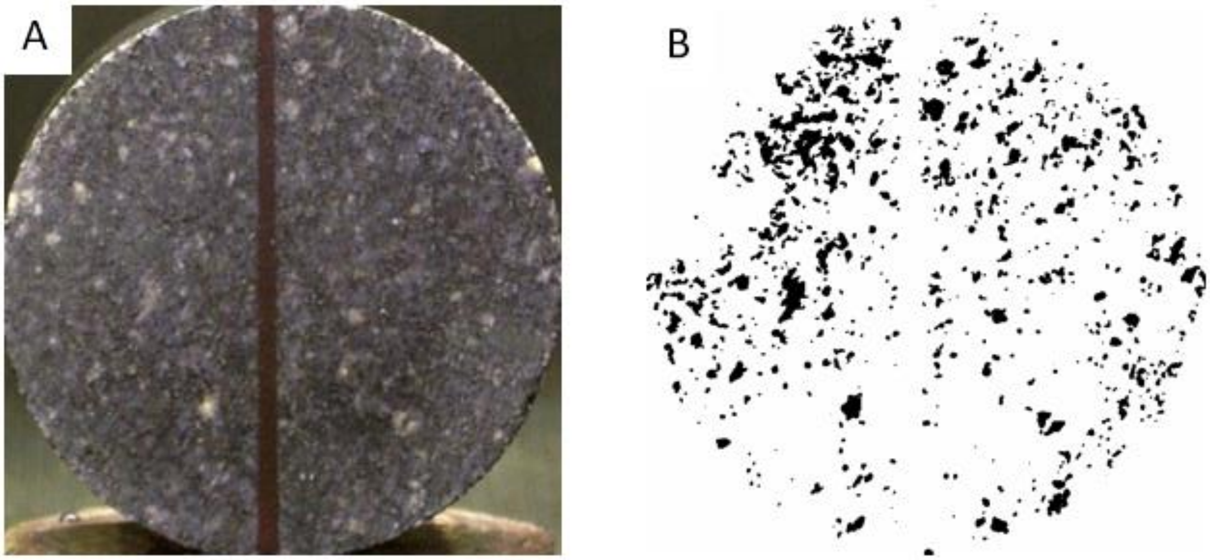

Figure A - 11: Granodiorite-Tonalite – KFM3A-110-20 (Jacobsson, 2004)

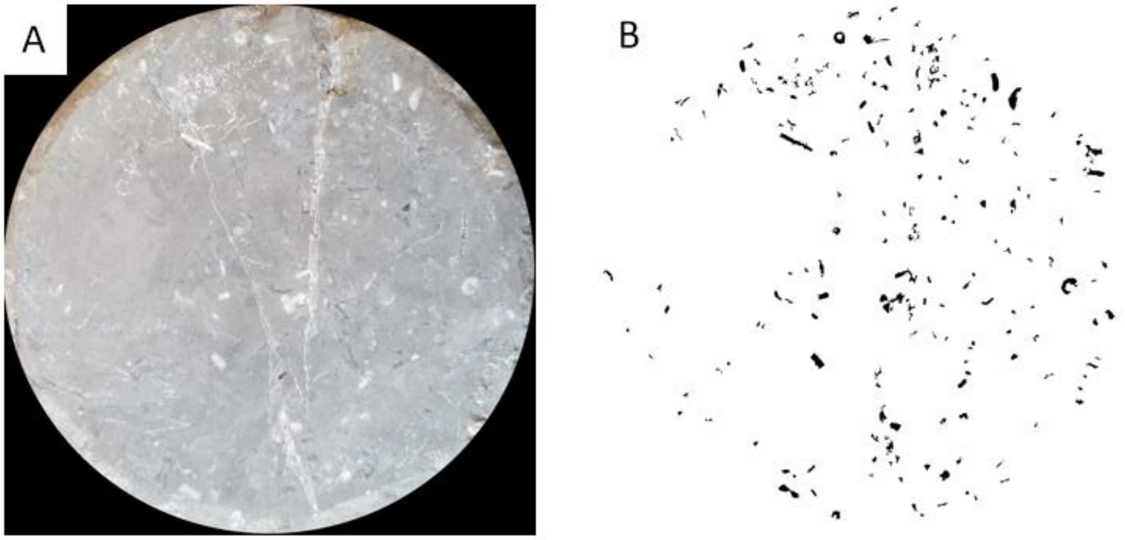

Figure B13: Cobourg Limestone – Sample 34

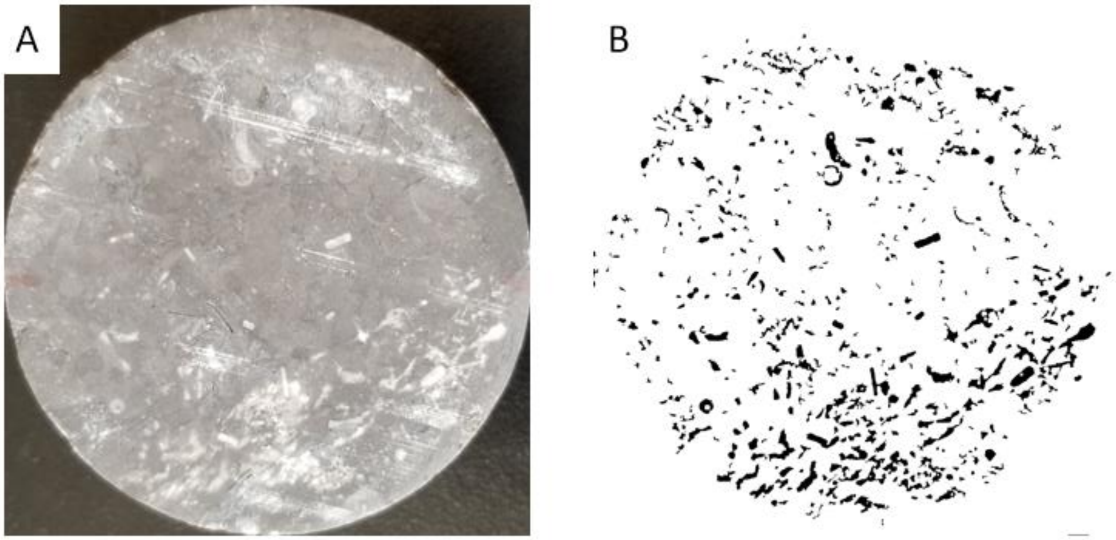

Figure A - 12: Cobourg Limestone – Sample 21a

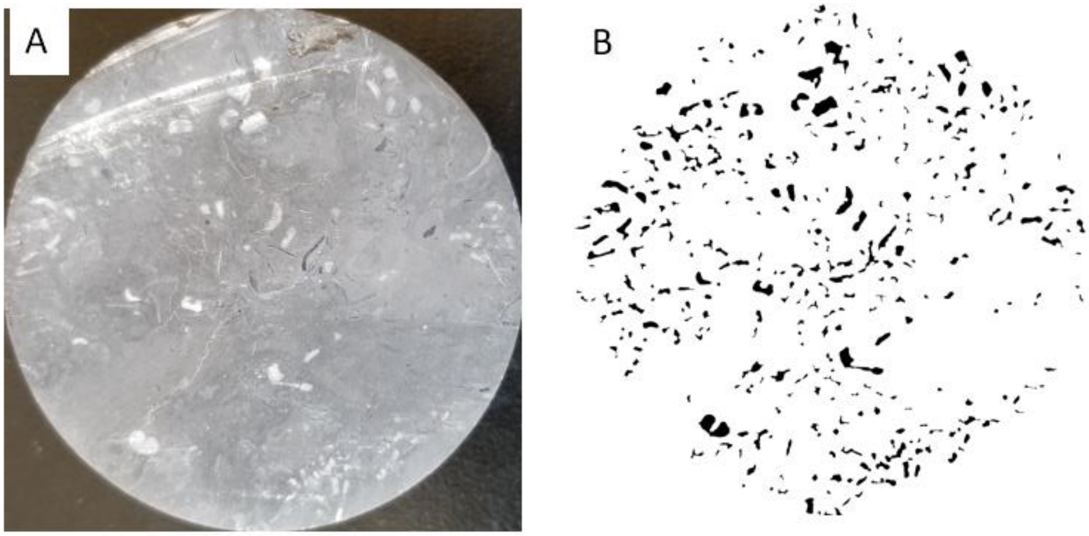

Figure A - 13: Cobourg Limestone – Sample 22d

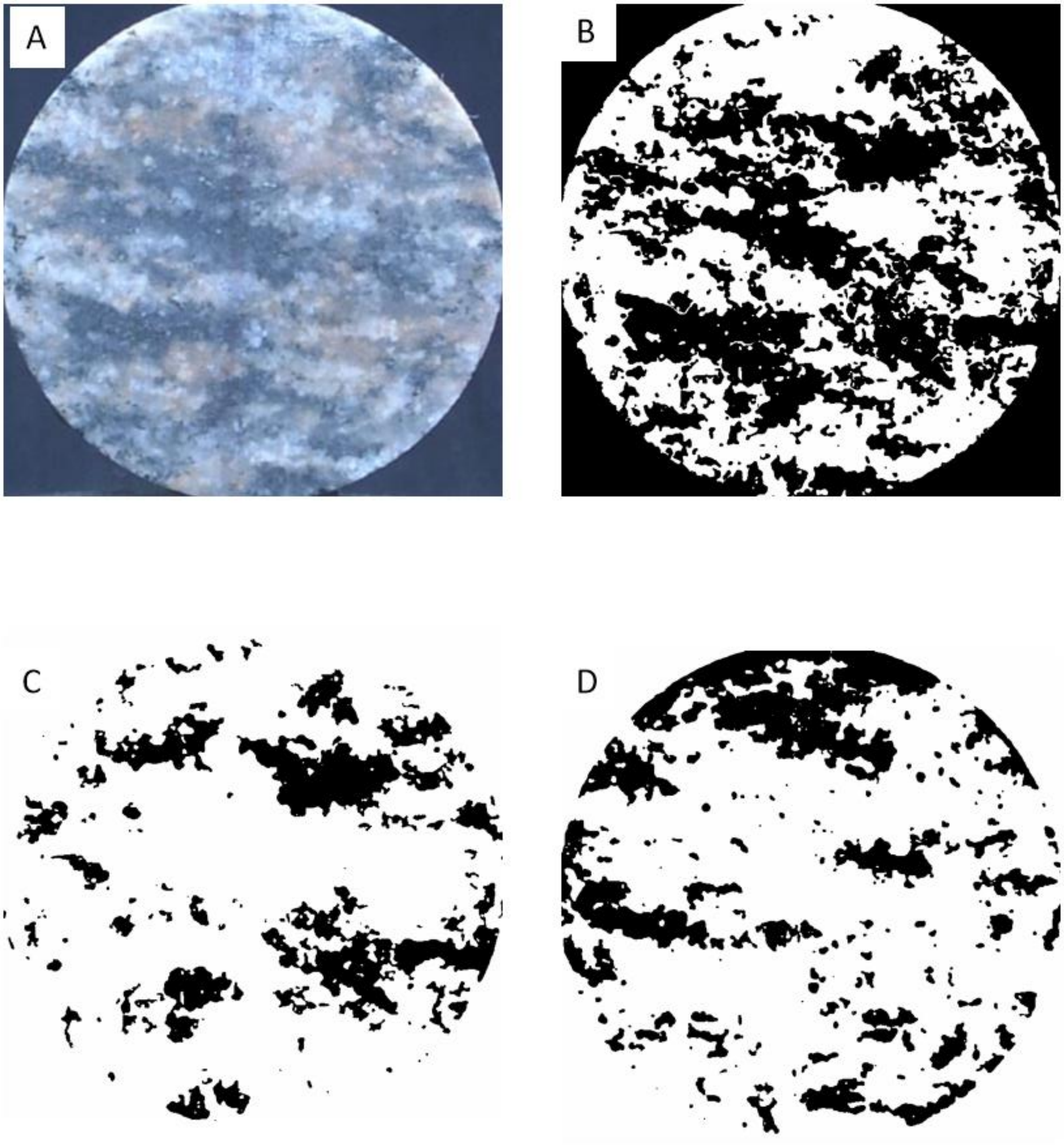

Figure A - 14: Pegmatite – KFM06A-110-2 (Jacobsson, 2005)

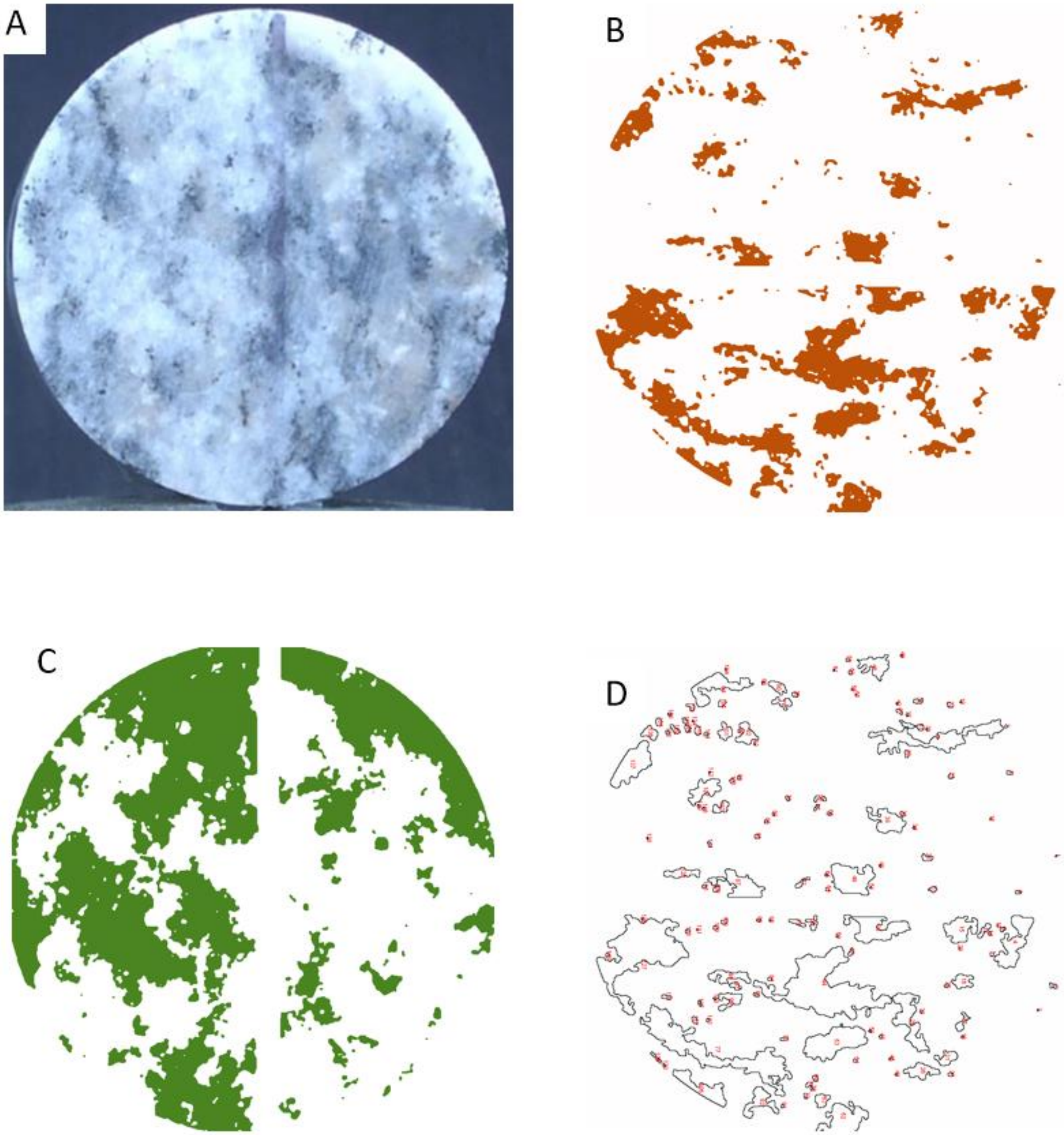

Figure A - 15: Pegmatite – KFM06A-110-3 (Jacobsson, 2005)

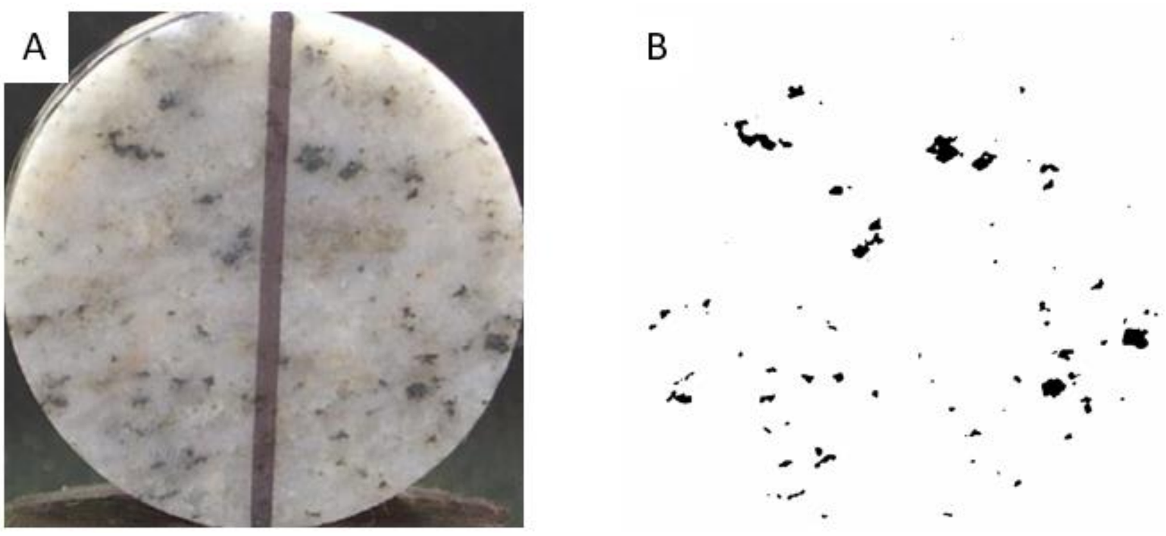

Figure A - 16:Albitic Granite - KFM08D-110-3

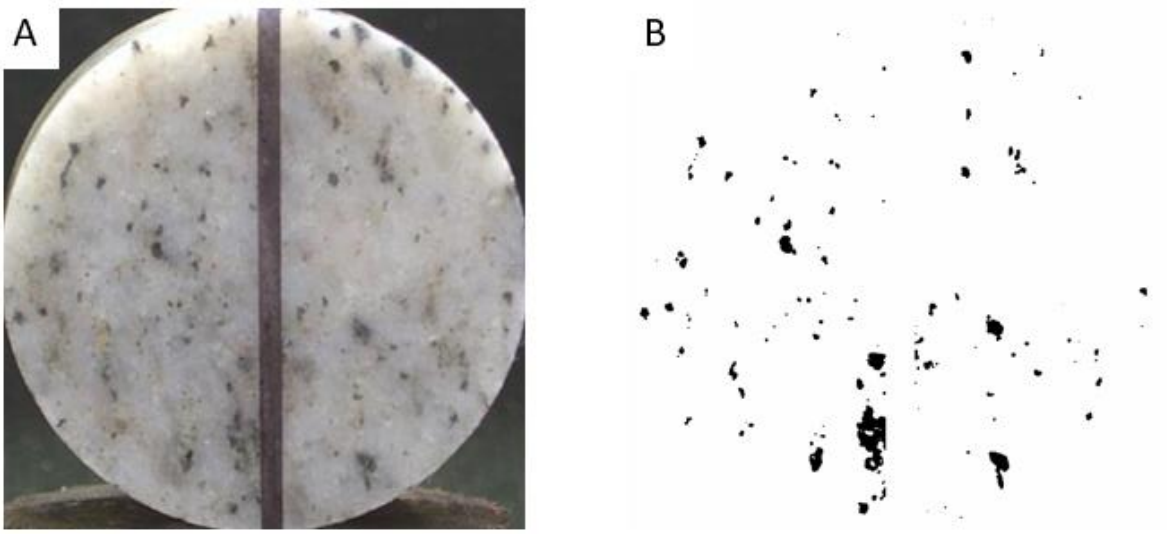

Figure A - 17: Albitic Granite - KFM08D-110-4

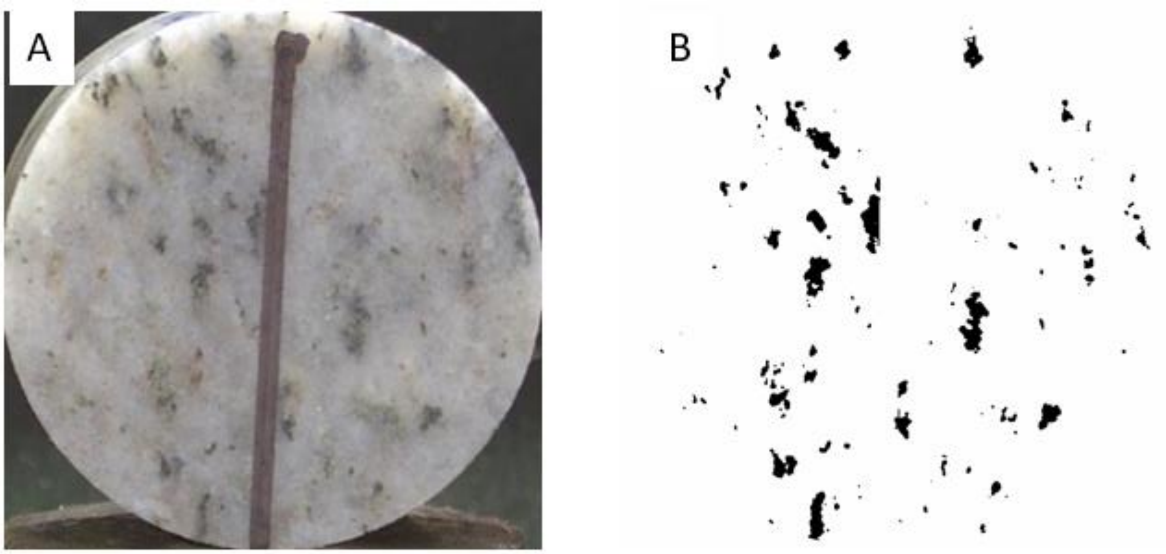

Figure A - 18: Albitic Granite- KFM08D-110-6

Appendix B: Point Cloud Cross Sections from Lidar scans for damage extent determination.

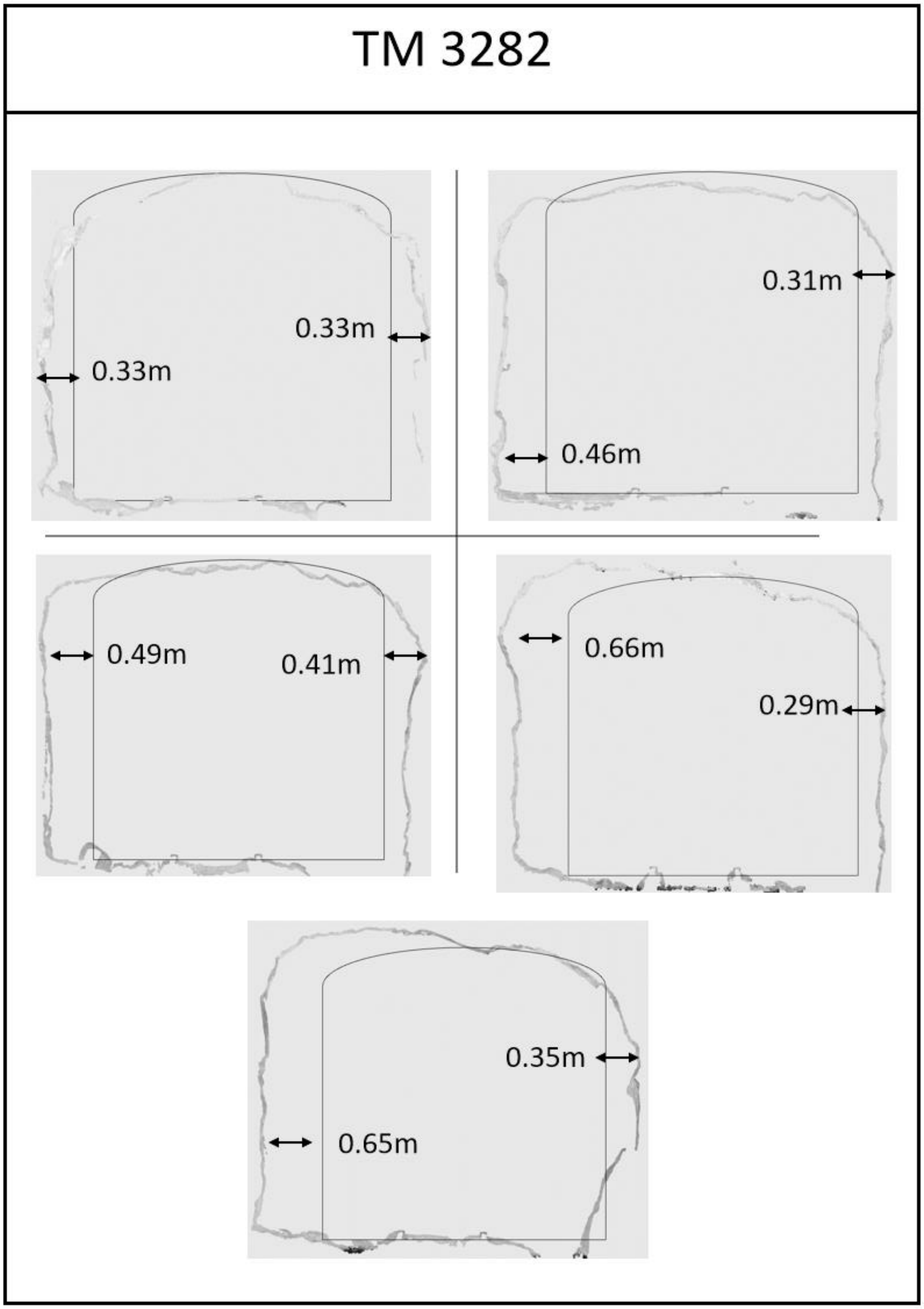

Figure B - 1: TM 3282

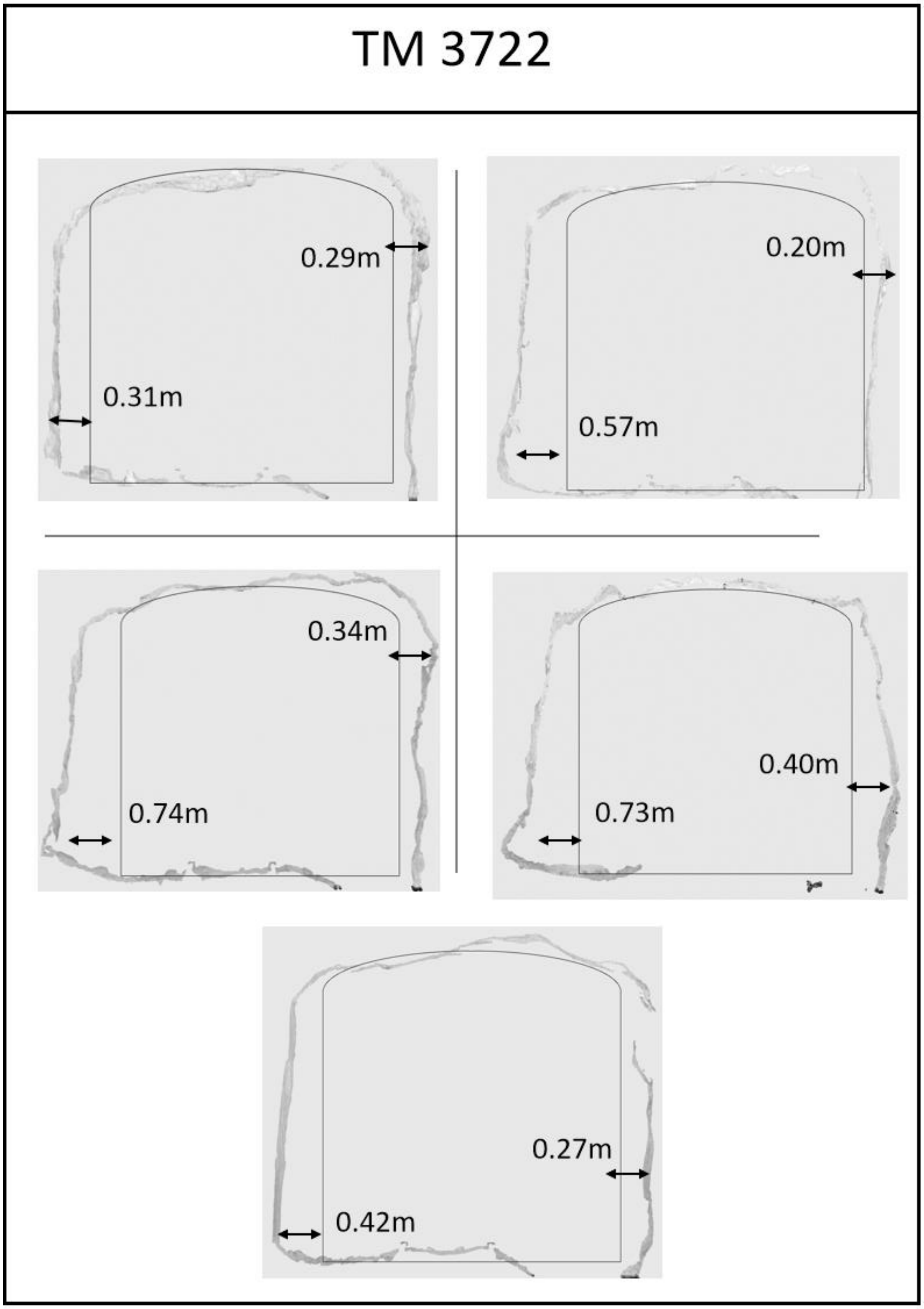

Figure B - 2: TM 3722

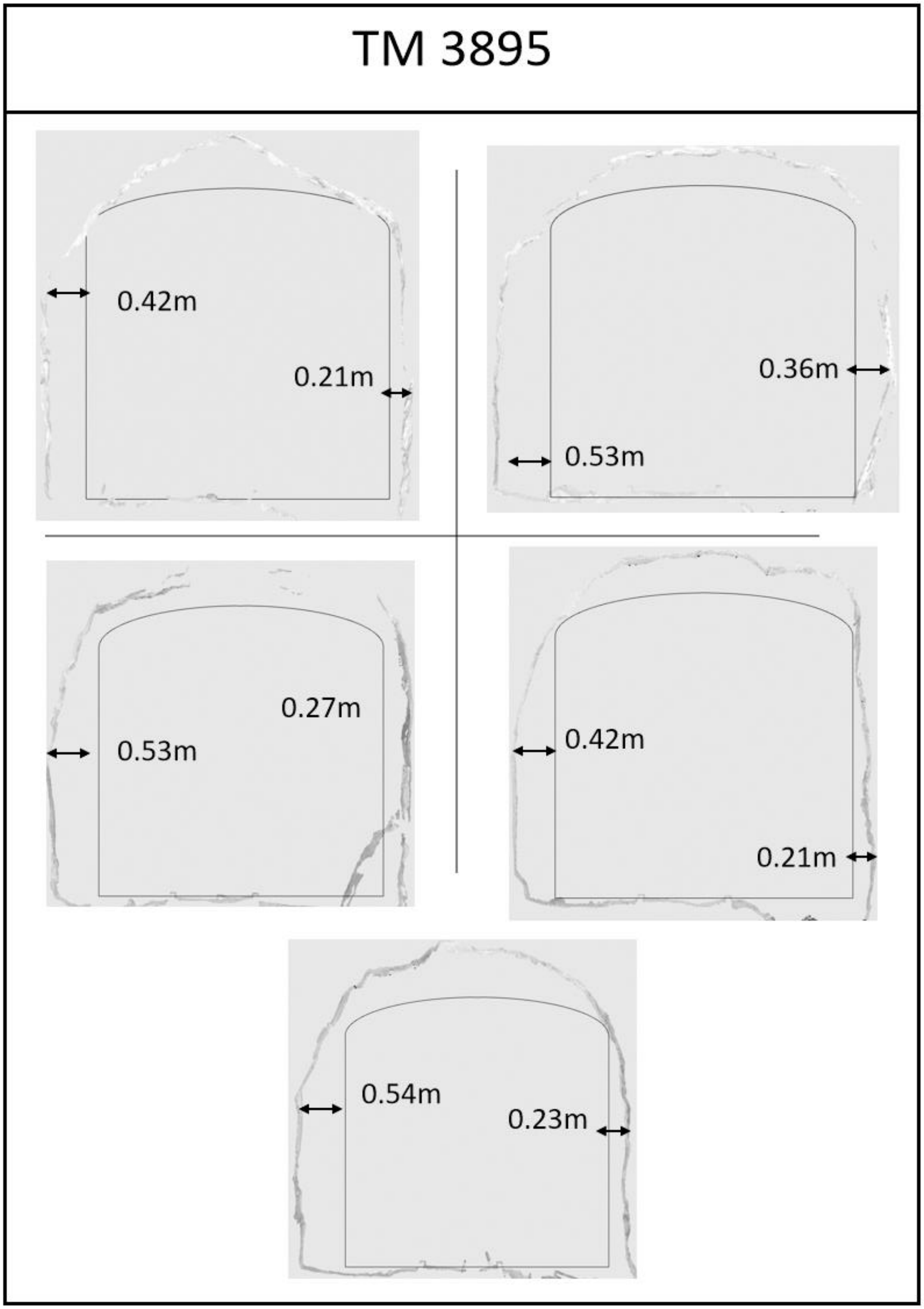

Figure B - 3: TM 3895

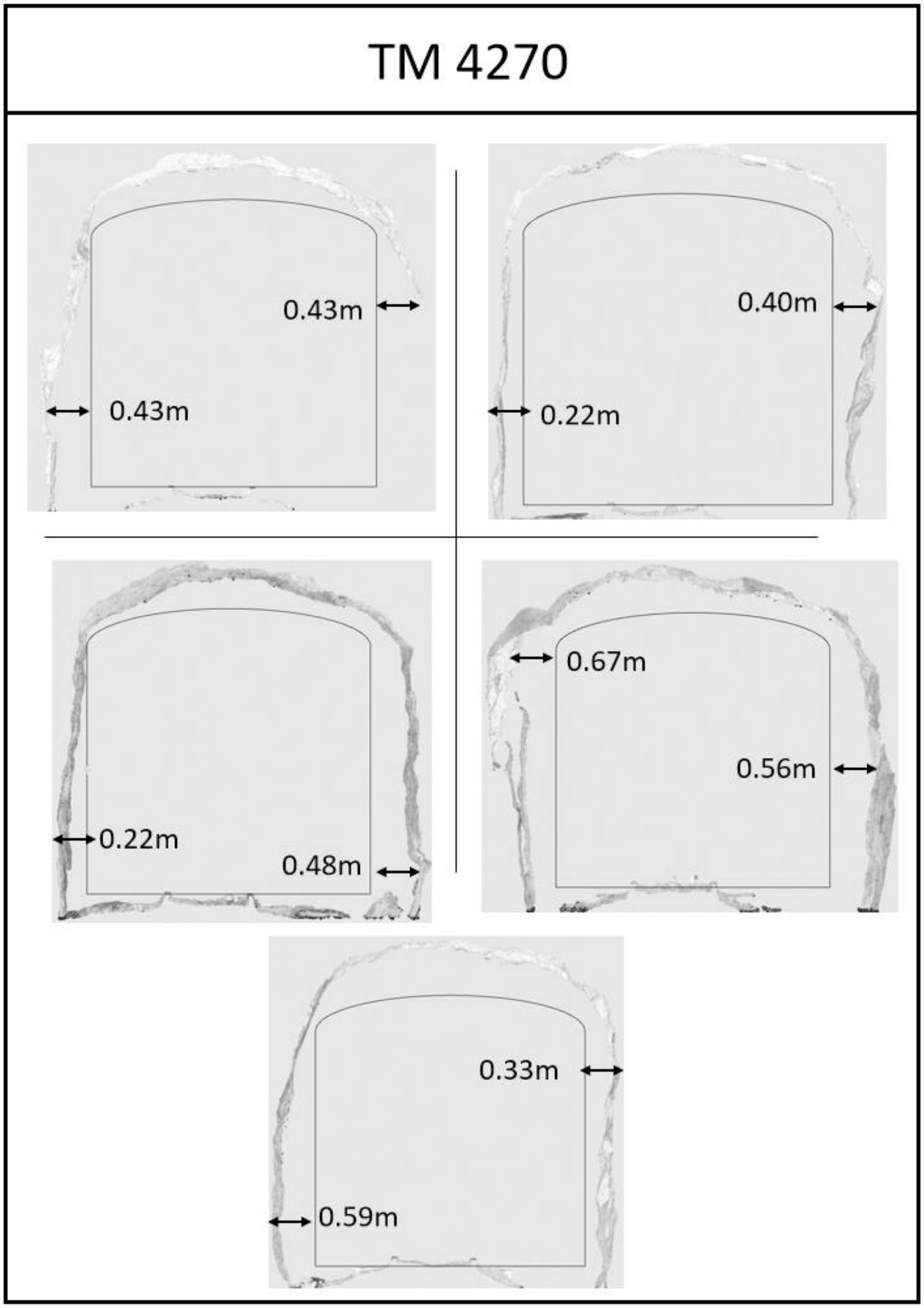

Figure B - 4: TM 4270

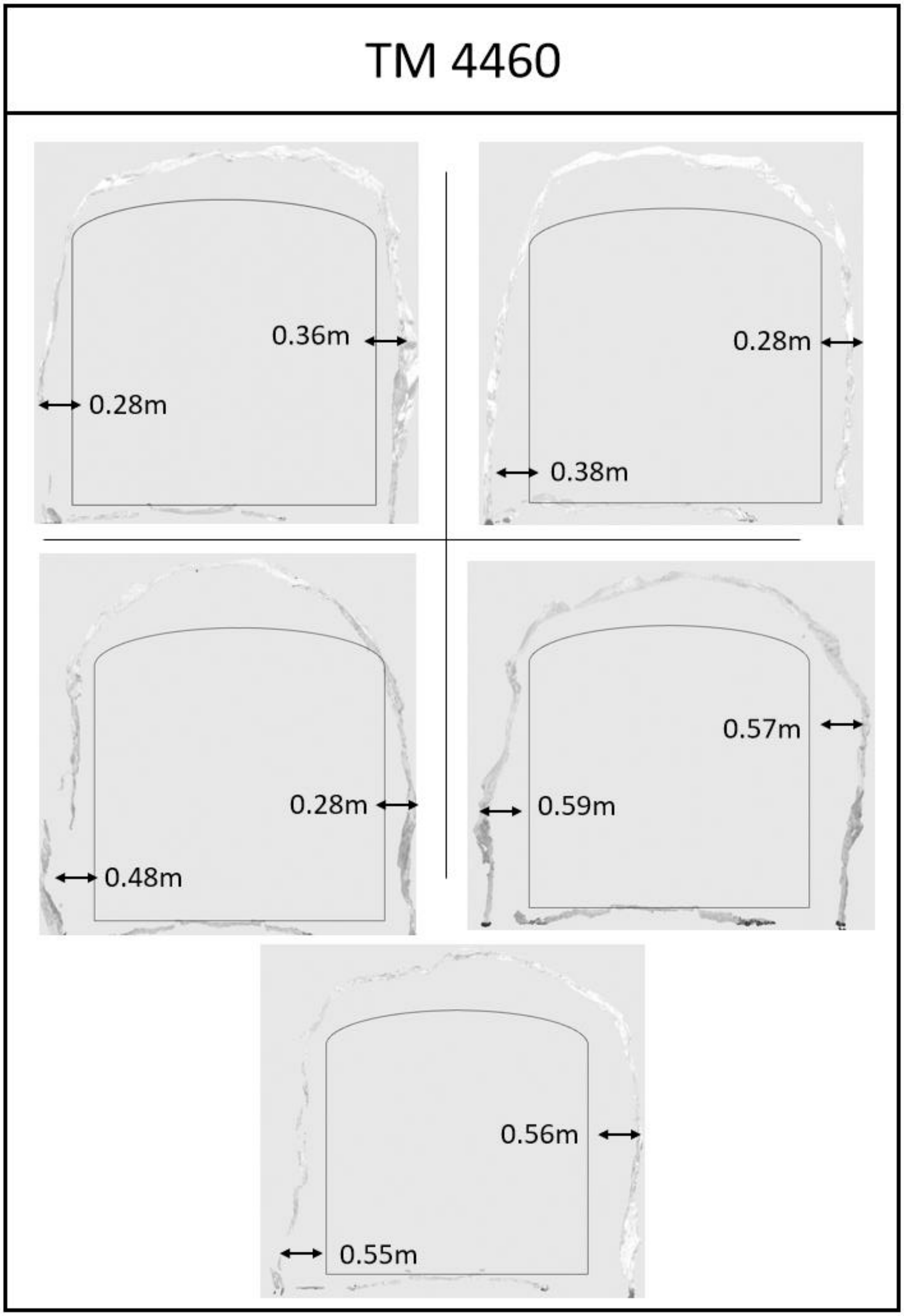

Figure B - 5: TM 4460

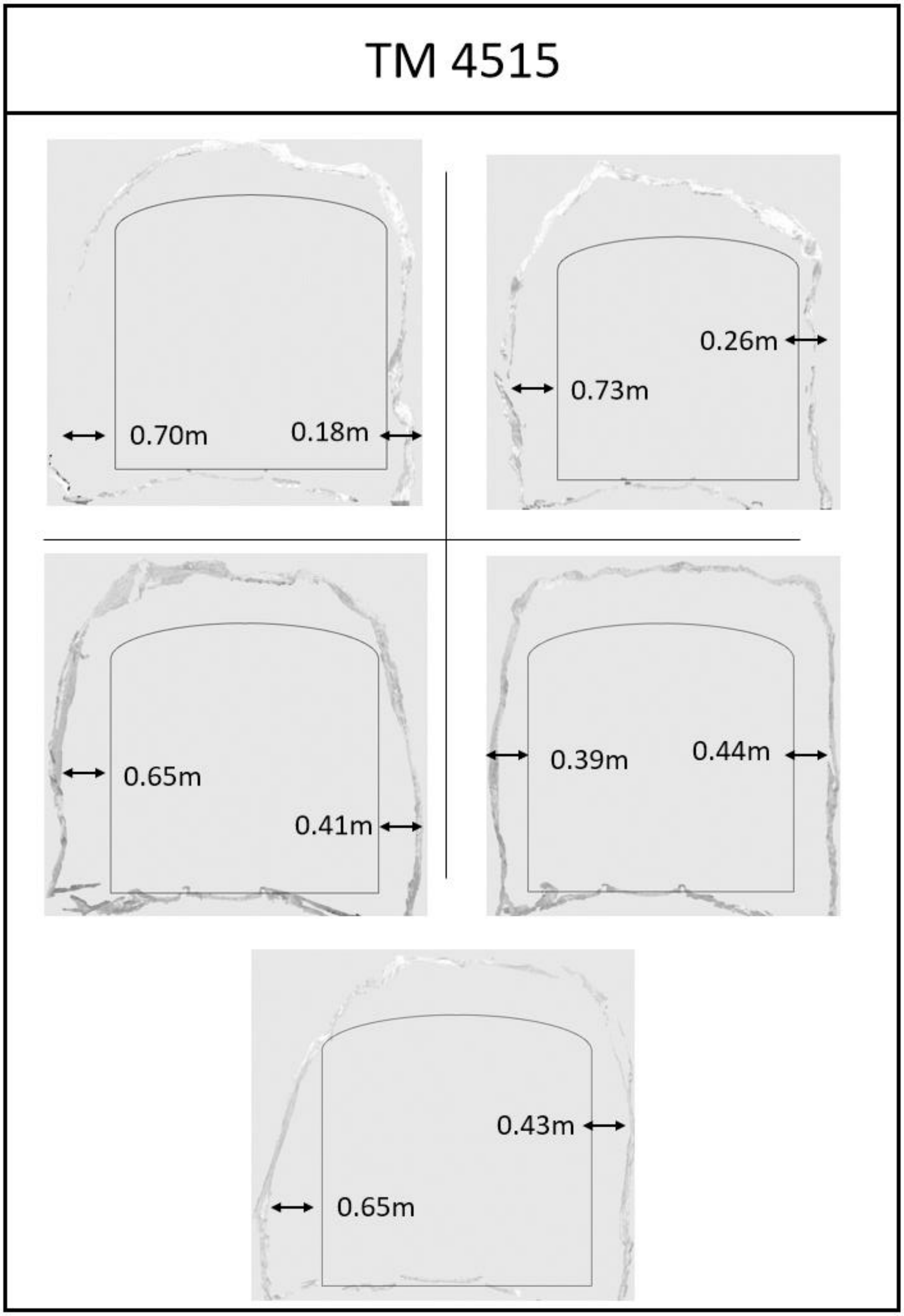

Figure B - 6: TM 4515

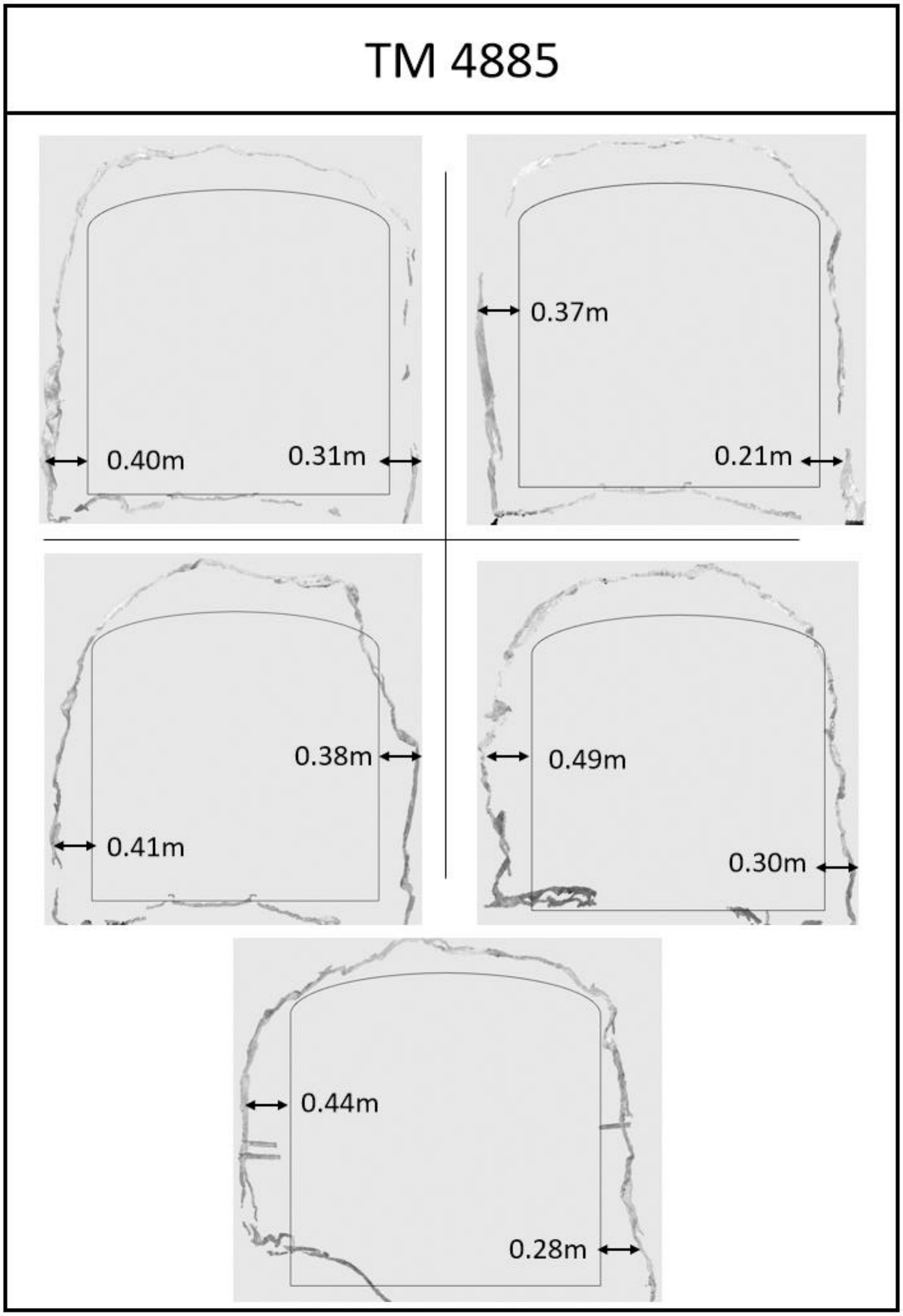

Figure B - 7: TM 4885

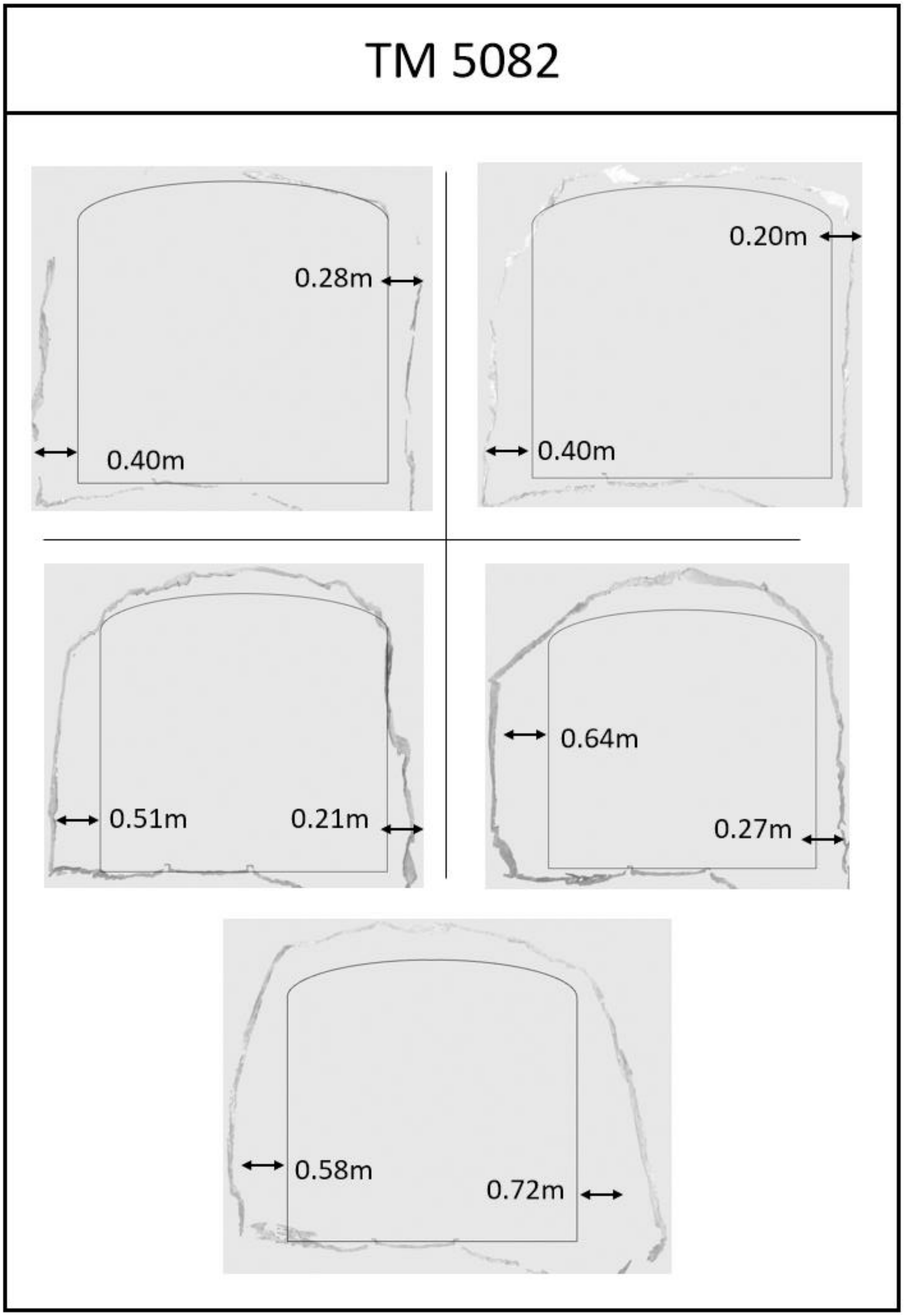

Figure B - 8: TM 5082

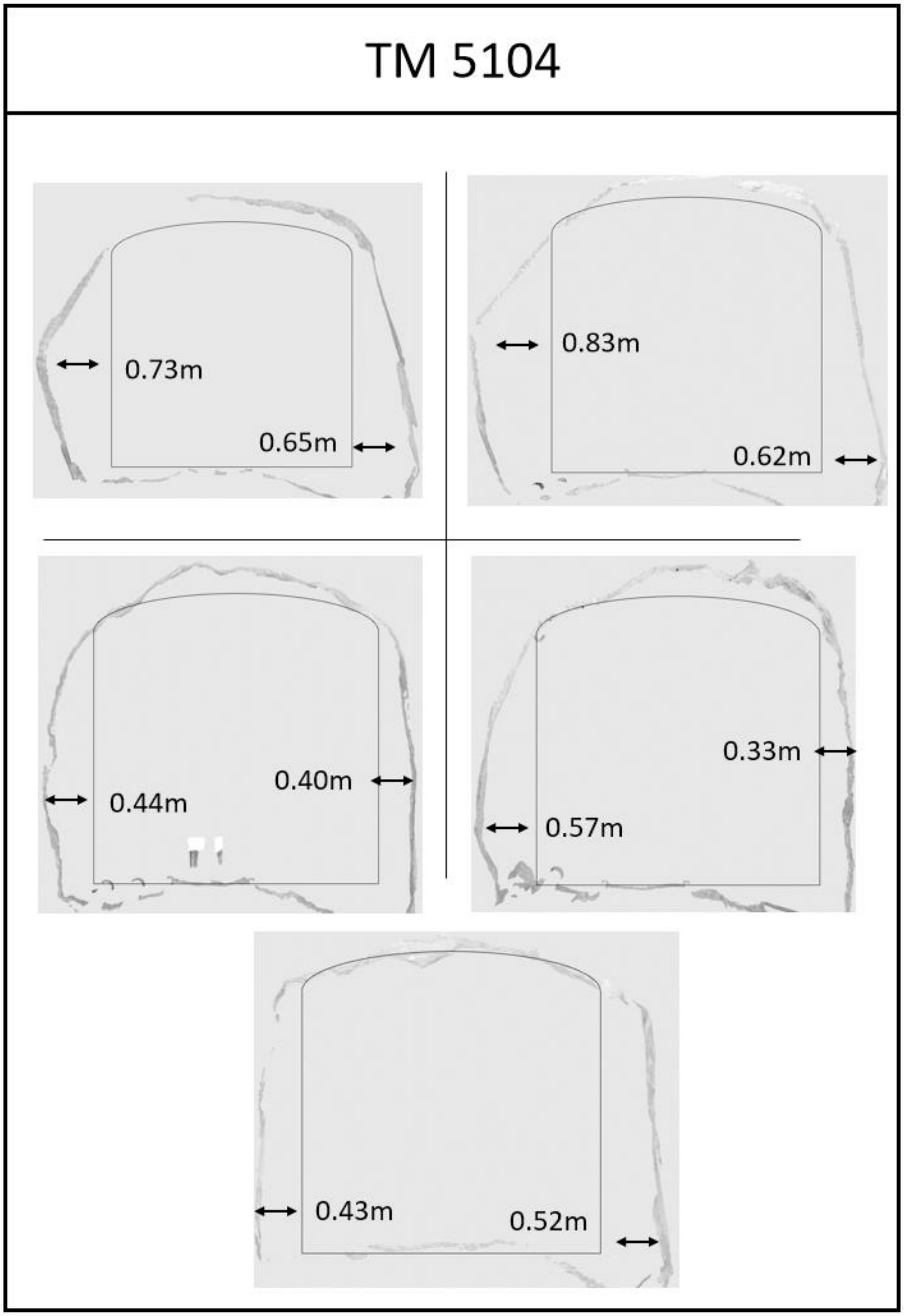

Figure B - 9: TM 5104

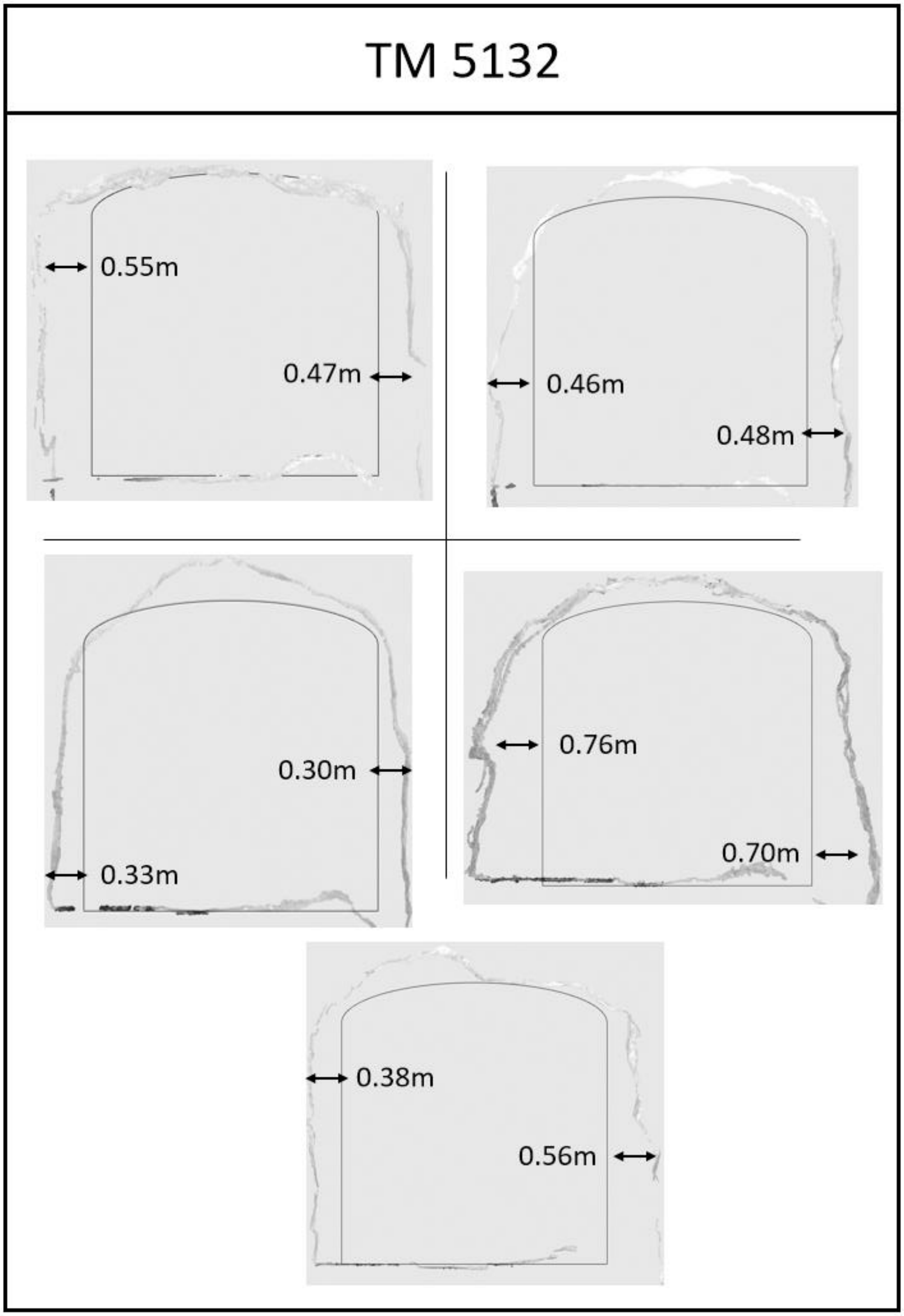

Figure B - 10: TM 5132